Nanoscale nonlinear optics using silica nanowires

A thesis presented

by

Geoffry T. Svacha

to

The Department of Physics

in partial fulfillment of the requirements

for the degree of

Doctor of Philosophy

in the subject of

Physics

Harvard University

Cambridge, Massachusetts

June 2008

Nanoscale nonlinear optics using silica nanowires

Eric Mazur Geoffry T. Svacha

Abstract

We have fabricated silica fibers with diameters less than one micrometer and molecularly smooth side walls. We modeled the waveguide properties and demonstrated low-loss light propagation over tens of millimeters, sufficient for microphotonic device applications. We manipulated silica nanowires into geometries to demonstrate waveguiding around tight bends as small as 5 micrometers, evanescent coupling, and wavelength filtering as a ring resonator. The linear waveguiding properties produced by the large index contrast between silica and air yield a tight confinement of the mode, which, when combined with the high electric field intensity in an ultrashort laser pulse, can produce significant nonlinear effects over lengths of about one millimeter. We studied nonlinear optical properties by observing the spectral broadening as a probe for the diameter-dependent nonlinearity of the silica nanowire. Our measurements confirmed the dependence of the generated spectra on the theoretically calculated effective nonlinearity and diameter-dependent dispersion. Our results reveal a diameter range for silica nanowires with an enhanced nonlinearity which may be employed in nonlinear devices. We fabricate a nonlinear Sagnac interferometer using silica nanowires for optical switching and discuss possibilities for optical logic. Our results confirm light-by-light modulation, with pulse energies less than a couple of nJ. Combining top-down and bottom-up fabrication techniques, we use tapered silica fibers to couple light directly into the waveguiding modes of ZnO nanowires. We experimentally confirm simulations for the coupling efficiencies and propagation of higher order modes. We also excite ZnO nanowires with ultrashort laser pulses and compare the spectrum transmitted along the nanowire waveguide with the spectrum at the excitation spot. Our results show

a shifting of the band edge that indicates a local heating of the nanowire by a few hundred degrees, which is confirmed by finite-element simulation. Finally, we discuss the outlook for nanoscale nonlinear optical devices.

Table of Contents

List of Figures

List of Tables

Acknowledgements

"Scientists are a friendly, atheistic, hard-working, beer-drinking lot whose minds are preoccupied with sex, chess and baseball when they are not preoccupied with science."

Yann Martel - *Life of Pi*

The camaraderie and bonding in our research group is like none other. I definitely owe a lot to this extended family especially Eric Mazur, for making it possible for such a great group of awesome, talented people to come together from around the world. I never imagined someone in his position could be so open and democratic about decision making. I have also learned a lot from him about how to take science and tell a story, be concise, and emphasize the big picture. Only through Eric making the group dynamic a top priority could we trust ourselves enough to tear each other apart and build each other back up again better.

Thanks to Kevin, Chris, Jason, and Diebold for reading through the thesis and providing feedback. Over the years, I'm happy to have met and spent time with Limin, Jon, Jim, Mike, Alex, Maria, Rafa and Simone, Iva, Vijay, Cleber, Tommaso, Brian and Ruby, Lauren and Jason, Prakriti, Sam, Mark and Jess, Eric, Tobias, Tina, Masa, Jessica, Albert, Daniel, Kasey, Rishi, Anja, Doug, Kevin, Chris, Jason, Virginia, and the other Mazur group alums I've been fortunate enough to meet. I especially remember pulling nanowires, listening to Fabolous and Jay-Z with "the high school student" who was more like a brother;

the best nut-themed social event ever, planned by Brian; cabbing it to IHOP at 3 o'clock in the a.m.; Watkins, who found, and is still finding, job postings for me; learning kendo from Masa with a yard stick; restraining myself from saying something embarrassing at Tina's wedding; returning skis with Jason, Mark, and Eric; staying at the casino in St. Ignace; losing to a Tuft's group at frisbee; destroying an MIT group at soccer; sneaking into chemistry bashes; frequenting the Queen's Head.

I want to thank Winkler for the moral support during the writing: there's nothing quite like 2a.m. coffee breaks... and "Every Other Week" rocks. Tina, I'm glad I dragged you into the internship at the Museum and the Exploratorium. Diebold, who defines the attitude "go big or go home," has definitely added flavor an otherwise mostly married lab. I've learned from him that since we only live one life, why not live it more like an episode of Entourage. If Albert is like my younger brother, then Rafa is definitely my older brother. E aí, mermão, beleza? Rafa, I can't thank you enough for all your help and guidance in the lab, showing us around Brazil teaching us to be Cariocas and meeting your family.

Kathryn Hollar helped push me to get involved in informal science education, and introduced me to Tim Miller from the Museum of Science. I want to thank Tom Hayes for his guidance in teaching the labs. My Korean instructor Kim Jung Hee was my surrogate mom for my first few years here and has an amazing teaching philosophy. I also owe many thanks to Virginia for looking out for me and everyone else in the lab.

My housemates and international traveling companions, Jon, David, Martin, Maciej and our English counterparts Helen, Conall, and Kate: I hope we can continue trekking across the globe together. Living in the dorms and offices would not have been the same without Christine, Mason, Katie, Hummon, Mosca, Laura, Dilini, Lydia, Andy, and the rest. The only way I made it to grad school is because of the Michigan SPS people, especially Ryan, Soo, Megan, Jim, and Lab Partner.

The Harvard Taekwondo club has been another awesome family to be a part of. I kept the little sanity I started grad school with by joining a club where people kick each other as a hobby, in the head much of the time, go figure. The club has changed a lot since I started, I'm happy to have met some of the old guard like Chris, Will, Jeanie, and Nadine, as well as the not-so-old guard Bui, Tina, Cha, Patrick, Calvin, Alice, Carl, Chunder, Luke, Jen, Diana, Bo, Ian, Samantha, Schwabish, Danny, and the downright young Dan, Nancy, Khoa, Victor, Christian, Julie, Richard, Dennis, TruckMin, and Hargate. One of the only constants in HTKD is Edwin Yoo, who really pulled me into the club and makes everyone feel welcome. For a club based on fighting, it is amazing just how much love there is. Sabrina, thank you!

Carbon, the JD, and Chase, enough said.

Finding these amazing extended families is only possible because of the incredible support from my family at home, my brothers, my mom, who remembered that my post-exam celebration was an ice cream shake, and my dad, who made me push for more than good enough. No matter where I'm at in my life, or how complicated it seems, they have always found a way to say the simplest thing and speak straight to the heart, or as Bean would say:

"Remember, the enemy's gate is down."

Orson Scott Card - *Ender's Game*

Geoffry T. Svacha
Cambridge, Massachusetts
June, 2008

Acknowledgements of Financial Support

This thesis is based on work supported by the National Science Foundation under contract ECS-0601520 and the Center for Nanoscale Science at Harvard University.

Citations to Published Work

Parts of this dissertation cover research reported in the following articles:

[1] T. Voss, G. T. Svacha, E. Mazur, and C. Ronning, "Influence of local heating by nonlinear pulsed laser excitation on the transmission characteristics of a ZnO nanowire waveguide," *submitted to Nano Letters*.

[2] T. Voss, G. T. Svacha, E. Mazur, S. Muller, C. Ronning, D. Konjhodzic, and F. Marlow, "High-order waveguide modes in ZnO nanowires," *Nano Letters*, vol. 7, pp. 3675–3680, Dec 2007.

[3] R. R. Gattass, G. T. Svacha, L. Tong, and E. Mazur, "Supercontinuum generation in sub-wavelength diameter silica fibers," *Optics Express*, vol. 14, pp. 9408–9414, Oct 2006.

[4] L. M. Tong, J. Y. Lou, Z. Z. Ye, G. T. Svacha, and E. Mazur, "Self-modulated taper drawing of silica nanowires," *Nanotechnology*, vol. 16, pp. 1445–1448, Sep 2005.

To Grandpa Bob and Grandpa Joe

Notice that the stiffest tree is most easily cracked,

while the bamboo or willow survives by bending with the wind.

Bruce Lee

Chapter 1

Introduction

1.1 Motivation

Gazing out across the Charles River toward the belfry of the Old North Church, a group of Paul Revere's associates stationed in Charlestown were looking for a flash of light that signified the American Revolution had begun. The signal, a simple one, was a lantern in a window, which encoded a very important piece of information. A single lantern indicated that the British military forces would be arriving "by land" while two lanterns meant they would come "by sea." On the evening of April 18th, 1775, after hours of staring at a slim black spire set against the night sky, two faint flickering lights were seen in the steeple, and Paul Revere began his historic ride through Lexington and Concord to alert the militia that the British forces were coming by boat into Cambridge [1].

The story of Paul Revere's ride symbolizes the importance of optical communication in our society. For thousands of years before Paul Revere, humans used fires, smoke signals, and flags to encode and transmit all types of military, cultural, and other information across long distances. Now, it is difficult to imagine a piece of information that takes longer than a few seconds to find using the connected optical network that makes up the

internet.

In 1880, Alexander Graham Bell invented a device called the photophone that was actually quite similar to lantern signals used by American revolutionaries a century earlier. The photophone consisted of a flexible mirror that reflected sunlight towards a receiver. The receiver consisted of a piece of selenium, whose electric resistance varies according to the degree of illumination [2]. As someone speaks into the transmitting device, sound vibrations are transformed into vibrations in light by the flexible mirror, which then creates a current in the receiver circuit resulting in an audible signal from a telephone disk. Bell also carried out the experiment using an electric light source, successfully transmitting over 86 yards.

Despite Bell's ingenuity, the photophone, while demonstrating an amazing engineering feat, was ultimately flawed due to the reliance on, and exposure to, environmental factors. Even with that limitation, the fundamental idea behind Bell's photophone has a few similar ideas in common with modern day communications systems. The major difference is the containment of the light signals in a "wire" that transports them to and from the receiver. Contemporaries of Bell were already observing and studying a phenomenon that would make a wire for light possible.

Almost 40 years prior the demonstration of the photophone, Daniel Colladon performed an experiment that confined light in water flowing from hole in a bucket. He observed [3]:

> I managed to illuminate the interior of a stream in a dark space. I have discovered that this strange arrangement offers in results one of the most beautiful, and most curious experiments that one can perform in a course on Optics.

John Tyndall later independently repeated this experiment, demonstrating the guiding of light by total internal reflection [4].

While Colladon, Tyndall, and others studied interesting experimental optical phenomena, James Clerk Maxwell described the theoretical mechanism for the propagation

of light, as well as how light interacts with materials [5]. To understand how light can be 'trapped' inside a stream of water, and ultimately how glass optical fibers can transmit data across a thousand kilometers, we will examine the interaction between light and matter. We can summarize the interaction by describing the induced polarization to the incident electric field. The constitutive relation

$$\mathbf{P} = \epsilon_0 \chi^{(1)} \cdot \mathbf{E}, \tag{1.1}$$

where $\epsilon_0 = 8.853 \times 10^{-12}$ A·s/V·m is the vacuum permeability, and material response is given by the first order susceptibility tensor $\chi^{(1)}$. Equation (1.1) describes the linear polarization response of a material to an applied electric field. While the linear response is certainly not the only contribution to the polarization, as we will describe below, many optical phenomena we observe in our daily lives can be explained with the simple relationship in Eq. (1.1).

Maxwell's equations yield a wave equation describing the propagation of light

$$\nabla^2 \mathbf{E} - \frac{1}{c^2} \frac{\partial^2 \mathbf{E}}{\partial t^2} = \mu_0 \frac{\partial^2 \mathbf{P}}{\partial t^2}. \tag{1.2}$$

where c is the vacuum speed of light and μ_0 is the vacuum permeability. Using the relation $\mu_0 \epsilon_0 = 1/c^2$, and substituting the induced polarization from Eq. (1.1) into Eq. (1.2), if we assume an instantaneous material response we obtain

$$\nabla^2 \mathbf{E} - \frac{(1 + \chi^{(1)})}{c^2} \frac{\partial^2 \mathbf{E}}{\partial t^2} = 0, \tag{1.3}$$

which resembles the propagation in free space, but with a wave velocity $v = c/\sqrt{1 + \chi^{(1)}}$. We define the index of refraction $n \equiv \sqrt{1 + \chi^{(1)}}$, which relates the speed of light in a vacuum to the speed of light in a material.

The index of refraction is a useful parameter when examining how light behaves

at an interface between two materials. Light propagating through material A with index n_A, when reaching an interface with material B with an index $n_B > n_A$ will propagate with a slower wave velocity through material B. When light approaches the interface at an angle different from normal incidence, then the leading edge of the wavefront reaches the interface first and slows down. The trailing edge of the wavefront propagates further in material A, traveling a farther distance than the leading edge, before it reaches the interface. The difference in wave velocity in the two materials results in the wavefront changing its angle, effectively causing light to 'bend' at the interface. For the case of $n_B > n_A$, the light bends toward the normal vector, while for $n_B < n_A$ light bends away from the normal, with the degree of bending determined by the contrast of the index of refraction. By solving geometrically for the change of the wavefront, we obtain Snell's Law

$$n_A \sin(\theta_A) = n_B \sin(\theta_B) \tag{1.4}$$

where θ_A and θ_B represent the angle of incidence and the angle of refraction, respectively. This quantitative description of light passing through an interface gives a surprising result for the case of $n_B < n_A$, specifically, a range of angles for θ_A where $\sin(\theta_B) > 1$. We define the critical angle $\theta_c \equiv \sin^{-1}(n_B/n_A)$, such that for $\theta_A > \theta_c$, there is no solution for θ_B. For the case when no angle is allowed for the light to enter material B, the light reflects from the interface and remains in material A. This phenomenon is called *total internal reflection*, and it is exactly what Colladon and Tyndall observed when they trapped light in a stream of water.

Light confined to a wire can be used to transmit binary information, but the practical application of total internal reflection for data transmission requires a reliable material and fabrication process. Scientists at Corning first demonstrated a low loss optical fiber made from fused silica in 1972 [6]. The optical fiber consists of a core region 3 μm

in diameter of fused silica doped with titanium oxide, and a cladding region about 100 μm in diameter of pure fused silica. The doping creates a difference of 0.008 in the index of refraction between the core and cladding, which provides total internal reflection for light approaching the interface at an angle greater than 84° from the normal (or equivalently, less than 6° from the plane of the surface). The purity of the material and uniformity of the fabrication process helped achieve losses of about 10 dB/km, enabling long distance optical communication with glass fibers.

In 1977, Bell Labs installed the first commercial fiber optic lightwave system in Chicago [7]. Light, transmitted along an optical fiber, works well as a signal from one end to the other, but in order to have a network that connects many distinct sites, the signals need to be routed through a series of nodes. At each node, the address for a particular piece of information, which is contained within the signal itself through a prearranged protocol, determines the destination. The process at the nodes takes place in electrical interconnects that detect the light signal, transform it to an electric signal, process that electric signal to get the address, and create a new optical signal which is then sent along the proper route.

Almost twenty years prior to the installation in Chicago, scientists at Bell labs and elsewhere [8, 9] were studying a process to create light which later became the optical signals in future communications systems, and also fundamentally changed our ability to study nature with optics. The development of the "laser" brought about unprecedented intensities of light at the same frequency, polarization, and phase, or, in a quantum mechanical description: a large number of photons in the same state. Lasers have since enabled new methods for imaging, more precise ways to keep time, the creation of new states of matter, and many other applications.

The invention of the laser also allows us to break the assumption we made in Eq. (1.1), because the large number of photons in the same state can simultaneously interact

with the matter, thereby contributing to the material response and allowing nonlinear phenomena. We can begin to describe this response as

$$\mathbf{P} = \epsilon_0 \chi^{(1)} \cdot \mathbf{E} + \mathbf{P}_{NL}, \tag{1.5}$$

By assuming that the nonlinear polarization $\mathbf{P}_{NL}$ can be treated as a perturbation, we can expand in powers of the electric field as

$$\mathbf{P} = \epsilon_0 (\chi^{(1)} \cdot \mathbf{E} + \chi^{(2)} \cdot \mathbf{EE} + \chi^{(3)} \cdot \mathbf{EEE} + ...) \tag{1.6}$$

with $\chi^{(k)}[(m/V)^{k-1}]$ being the kth-order susceptibility tensor [10]. The additional terms, with higher powers of electric field, result in the mixing of waves which allows for the generation of sum and difference frequencies, as well as higher harmonics, of the incident field. When a laser pulse interacts with a material where the nonlinear contribution to the polarization is non-neglible, and the dispersive properties of the material are considered, the evolution of the pulse can become quite complex both spectrally and temporally [11]. This complexity has created tremendous growth of the field of nonlinear optics over the past 40 years, and allowed for mathematical analogies to be drawn to fields as distant as black hole event horizon dynamics [12].

For the long distance signal-carrying optical fibers, effects due to nonlinearity degrade the signal integrity. The study of nonlinear optics describes pulse propagation in various dispersion and nonlinear regimes, and presents opportunities to minimize signal degradation. The careful balance of waveguide nonlinearity, anomalous dispersion, and pulse power can yield a solitary wave, or "soliton", that propagates without distortion and which can be used to transmit information along optical fibers [11].

While the understanding of nonlinear optics helps to avoid unwanted signal distortion in an optical communications transmission line, nonlinear systems can have many other

applications. Many useful components in electrical systems, such as diodes and transistors, rely upon nonlinear operation. In fact, the electrical interconnects that do the routing and signal processing at the nodes of an optical network contain hundreds to thousands of these electrical components. The capacity of optical networks used to transmit information in metro and long haul networks has followed a doubling trend analogous to Moore's law, coined Butter's Law of Phontonics, that states the capacity doubles every nine months. That rate is twice the rate of doubling for many performance parameters of the computer industry. The quicker growth rate for photonics implies that the electrical interconnects that perform the switching and routing will become the limiting feature of the network. One promising solution for overcoming this bottleneck is the replacement of the electrical interconnect with an all-optical circuit.

Optical fibers rapidly replaced copper wires as the preferred transmission lines due to their large bandwidth and low power consumption. Using standard optical fibers in order to perform the operations required at the network nodes, such as splitting signal channels (demultiplexing), processing, and recombining signals (multiplexing), is impractical due to the physical size of the constituent components. This limitation is analogous to what the electronics industry faced when increasing the processing power of a computer: increase the size of the computer, or decrease the size of the components. The photonics industry needs to address the same concerns: as the number of information channels on an optical fiber increases from hundreds to thousands, an optical circuit capable of handling that demand will need to have miniaturized individual components.

The economic push for increased information capacity leads to smaller optical waveguides and devices that can be incorporated into optical circuits. As we shrink the components, in particular as the feature size approaches the wavelength of light and below – we need a fundamental understanding of the interaction of light and matter at the nanoscale.

For example, unlike electrons flowing in a conducting wire, photons traveling in a nanoscale waveguide have a substantial evanescent field that is susceptible to surface roughness which results in scattering. On the other hand, studying light at the nanoscale may provide opportunities to take advantage of physical phenomena that are not manifested on a larger scale. For example, metallic and dielectric nanoparticles can exhibit "capacitor-like" and "inductor-like" responses to an incident optical field; the particles can be arranged to create an optical circuit whose behavior is analogous to traditional electronic circuits [13].

Many different materials and technologies have been used to make small waveguides, including plasmonic waveguides [14, 15], semiconductor nanowires [16, 17, 18, 19, 20], and lithographically-defined nanowires [21, 22, 23, 24]. Each fabrication technique brings its own advantages and limitations, which are frequently linked to the specific material system. A few of the concerns when fabricating nanoscale waveguides are the surface roughness, material absorption, large-scale patterning, geometry restrictions, and susceptibility to the environment.

In this dissertation, we will be studying the optical properties of silica nanowires fabricated by a taper-drawing method [25], and ZnO nanowires chemically grown with a vapor-liquid-solid technique [26]. We explore the possibility of building nanoscale optical devices that rely on nonlinearity to achieve their function. We demonstrate the power-dependent transmission of one such device, and discuss how it can integrated for optical switching and logic into an all-optical circuit.

1.2 Organization of the dissertation

Overall, this dissertation is separated in two parts. The first part of the thesis will be concerned with using the linear and nonlinear optical properties of silica nanowires for

assembling microphotonic devices, and the second part of the thesis will cover the potential use of ZnO nanowires.

Chapter 2 introduces sub-micrometer silica optical fibers and their properties. We review the fabrication technique, physical properties, device manufacture and their applications. We focus on the linear optical properties such as the large evanescent field and the diameter-controlled dispersion.

Chapter 3 discusses nonlinear effects inside nanowires. The relevant parameters for wave propagation inside a fiber are reviewed and discussed in light of small diameter fibers. We utilize supercontinuum spectrum broadening as a measure of the nonlinearity of the fiber. We demonstrate that nonlinearity and dispersion play crucial roles in determining the wavelength broadening of the supercontinuum.

Chapter 4 presents a silica nanowire Sagnac interferometer. We use the nonlinear phase accumulated in a loop assembled from a silica nanowire to induce a power-dependent transmission that may be used for optical switching. We discuss the potential implementation of the nonlinear Sagnac interferometer as NAND optical logic gate.

Chapter 5 examines the waveguiding properties of ZnO nanowires. The top-down taper-drawn silica nanowires are used to directly inject light into the waveguiding modes of the bottom-up chemically grown ZnO nanowires. We experimentally demonstrate coupling and broadband waveguiding and use simulations to show the role of higher-order modes in the transmission behavior of ZnO nanowires.

Chapter 6 discusses the transmission characteristics of ZnO nanowires being excited by a femtosecond-pulsed laser. The transmission spectrum at the output is compared with excitation spot to reveal a shift in the band edge due to heating of the ZnO nanowire. Finite-element simulations give a temperature distribution along the wire consistent with the experimentally band shifting.

Chapter 7 summarizes the work contained within the dissertation and discusses the potential for employing nonlinear effects at the nanoscale to create novel photonic devices.

Chapter 2

Silica nanowires

In this chapter, we introduce nanoscale waveguides fabricated from silica optical fibers, with a focus on their linear optical properties. We model the waveguides as cylindrical dielectric rods with a high refractive index contrast between silica and air. Calculations reveal interesting waveguide properties including tight confinement of the mode, a large evanescent field, and a strongly diameter-dependent dispersion. We discuss the fabrication techniques for making sub-micrometer diameter silica fibers, examine their physical properties, and demonstrate the coupling of light from macroscopic light sources into the silica nanowires via tapered fiber. Their optical properties, including the transmission and bending loss, were measured experimentally. We also explore possible applications for these silica fibers in more complex microphotonic devices. These devices will be discussed in later chapters, along with nonlinear wave propagation, to offer a potential platform for miniaturized optical switching and logic.

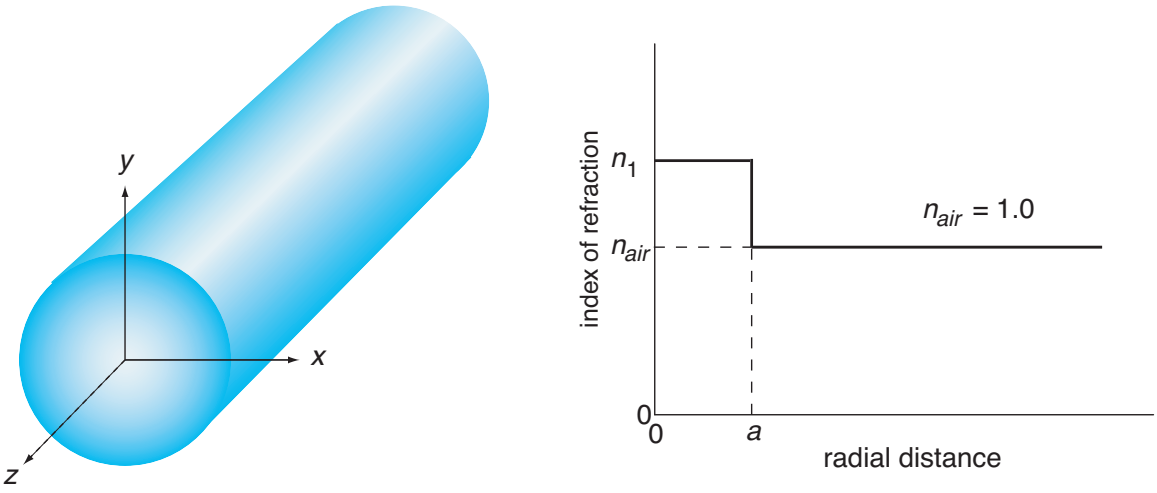

Figure 2.1: The geometry and index of refraction profile for an air-clad silica nanowire. The value of n_g is the index of the cladding of the standard optical fiber preform.

2.1 Linear wave propagation in silica nanowires

In this section, we examine the linear waveguiding properties of nanoscale step-index cylindrical dielectrics. In particular, we want to understand the propagation of light in sub-micrometer diameter silica fibers, also referred to as silica nanowires. The waveguiding modes of cylindrical dielectrics have been heavily studied over the past 50 years [27], thus we will focus our attention on the propagating modes when the dimensions enter the nanoscale. The fabrication of silica nanowires from standard optical fibers will be discussed in Section 2.2 and the experimental characterization of their linear optical properties in Section 2.4. The treatment of waveguiding in ZnO nanowires in Chapter 5 shares much in common with the analysis presented in this section.

Figure 2.1 describes the geometry of a step-index cylindrical dielectric waveguide. Even though the index profile appears qualitatively similar to standard step-index optical fibers, an important difference between standard fibers and silica nanowires is the index contrast. The difference between germanium-doped silica and fused silica yields a contrast

of about 10^{-3} for standard fibers, while the index contrast between fused silica and air is about 0.5. The large increase in index contrast for silica nanowires leads to tight mode confinement which is essential for the experiments described in Chapters 3 and 4.

To understand the propagation of light in a dielectric material with a refractive index profile like that shown in Figure 2.1, we rewrite the wave equation for the electric field from Eq. (1.2), with the polarization, $\mathbf{P}$, from Eq. (1.6) separated into its linear, $\mathbf{P}_L$, and nonlinear parts, $\mathbf{P}_{NL}$

$$\nabla^2\mathbf{E} - \frac{1}{c^2}\frac{\partial^2\mathbf{E}}{\partial t^2} = \mu_0\frac{\partial^2\mathbf{P}_L}{\partial t^2} + \mu_0\frac{\partial^2\mathbf{P}_{NL}}{\partial t^2}. \tag{2.1}$$

We will focus here on the linear optical waveguiding and ignore the nonlinear contribution to the polarization $\mathbf{P}_{NL}$ in this chapter. The linear contribution to the polarization is $\mathbf{P}_L = \epsilon_0\chi^{(1)}\mathbf{E}$, where ϵ_0 is the vacuum permittivity. With that substitution, we can solve Eq. (2.1) using separation of variables [11](where the direction of propagation is along the z axis) assuming a solution of the form

$$E(r,t) = F(x,y)A(z,t)e^{-i\beta(\omega)z}, \tag{2.2}$$

where $F(x,y)$ gives the shape of the transverse modes, $A(z,t)$ describes the slowly varying change in the direction of propagation (also referred to as the "pulse envelope"), and the factor $e^{-i\beta(\omega)z}$ describes the fast oscillations, if we define the propagation constant $\beta(\omega) \equiv n(\omega)\omega/c$, where c is the speed of light in vacuum. Note that the index of refraction $n(\omega) = 1 + \frac{1}{2}\mathrm{Re}[\chi^{(1)}(\omega)]$ appears in the phase of the fast oscillation term, which will be important when we consider an intensity-dependent index of refraction in the next chapter.

If we consider a quasi-monochromatic source, the spectrum of the electric field is centered around a frequency ω_0 (also referred to as the "carrier frequency"), and $\beta(\omega)$ can be expanded in a Taylor series

$$\beta(\omega) = n(\omega)\frac{\omega}{c} = \beta_0 + \beta_1(\omega - \omega_0) + \frac{1}{2}\beta_2(\omega - \omega_0)^2 + \dots \tag{2.3}$$

where β_m represents the mth derivative of the propagation constant with respect to ω

$$\beta_m = \left(\frac{d^m\beta}{d\omega^m}\right). \tag{2.4}$$

We can gain physical insight into the wave propagation by examining the terms of this expansion. The first order term, β_1, describes the motion of the pulse envelope, and is related to the group velocity by $\beta_1 = v_g^{-1}$. The higher order terms describe the dispersion of the medium, which are important for pulse propagation even when we ignore nonlinear effects. The dominant contribution comes from the second order term β_2, also called group velocity dispersion (GVD) [28], which is commonly written as the waveguide dispersion parameter

$$D_W = -\frac{2\pi c}{\lambda^2}\beta_2 \tag{2.5}$$

which can be expressed for experimental purposes in the convenient units of ps/km·nm. For completeness, we define the material dispersion [28]

$$D_M = -\frac{\lambda}{c}\frac{d^2n}{d\lambda^2}. \tag{2.6}$$

For a pulse propagating along a waveguide in the fundamental mode, the dispersion is the sum of the material and waveguide dispersions. We will examine the dependence of the dispersion on nanowire diameter below.

Keeping the third order term β_3, simply called third order dispersion, we neglect higher order terms and write the expansion for $\beta(\omega)$, from Equation (2.3) as

$$\beta(\omega) = n(\omega)\frac{\omega}{c} = \beta_0 + \beta_1(\omega - \omega_0) + \frac{1}{2}\beta_2(\omega - \omega_0)^2 + \frac{1}{6}\beta_3(\omega - \omega_0)^3. \tag{2.7}$$

The term β_3 is very small and usually neglected as well, but when operating near the zero GVD wavelength, or for broadband pulse propagation in fibers, β_3 can have a strong contribution.

When solving for the propagation constant β in standard optical fibers, the weakly guiding approximation, $n_{core} \approx n_{cladding}$, is often used to simplify the solutions resulting in degenerate modes within a narrow range for β: $kn_{cladding} < \beta \leq kn_{core}$ [29]. Due to their small diameter and high index contrast, light propagation in nanowires cannot be solved approximately. Solving Maxwell's equations for the nanowire geometry with no approximation yields modes that have all six nonzero electric and magnetic field components [30, 31].

Figure 2.2 shows numerical results for the propagation of the fundamental mode in a nanoscale cylindrical dielectric waveguide. Figure 2.2a and b show that as the diameter decreases beyond the wavelength of light, an increasing amount of the Poynting vector is found outside of the waveguide as evanescent wave. Figure 2.2c plots the percentage of the electro-magnetic field power propagating inside the core as a function of the nanowire diameter for three wavelengths of light. Using Figure 2.2d, which plots the critical diameter for single mode operation, we can make the general statement when less than ∼80% of the power is guided in the core, the nanowire is single mode. Another restatement: when the nanowire diameter is smaller than λ/n, the nanowire is single mode.

The large evanescent field observed in Figure 2.2 affects many of the optical properties of the nanowire, including the dispersion from Eq. (2.5). Figure 2.3a plots the calculated dispersion for a laser pulse with 800-nm center wavelength as a function of the

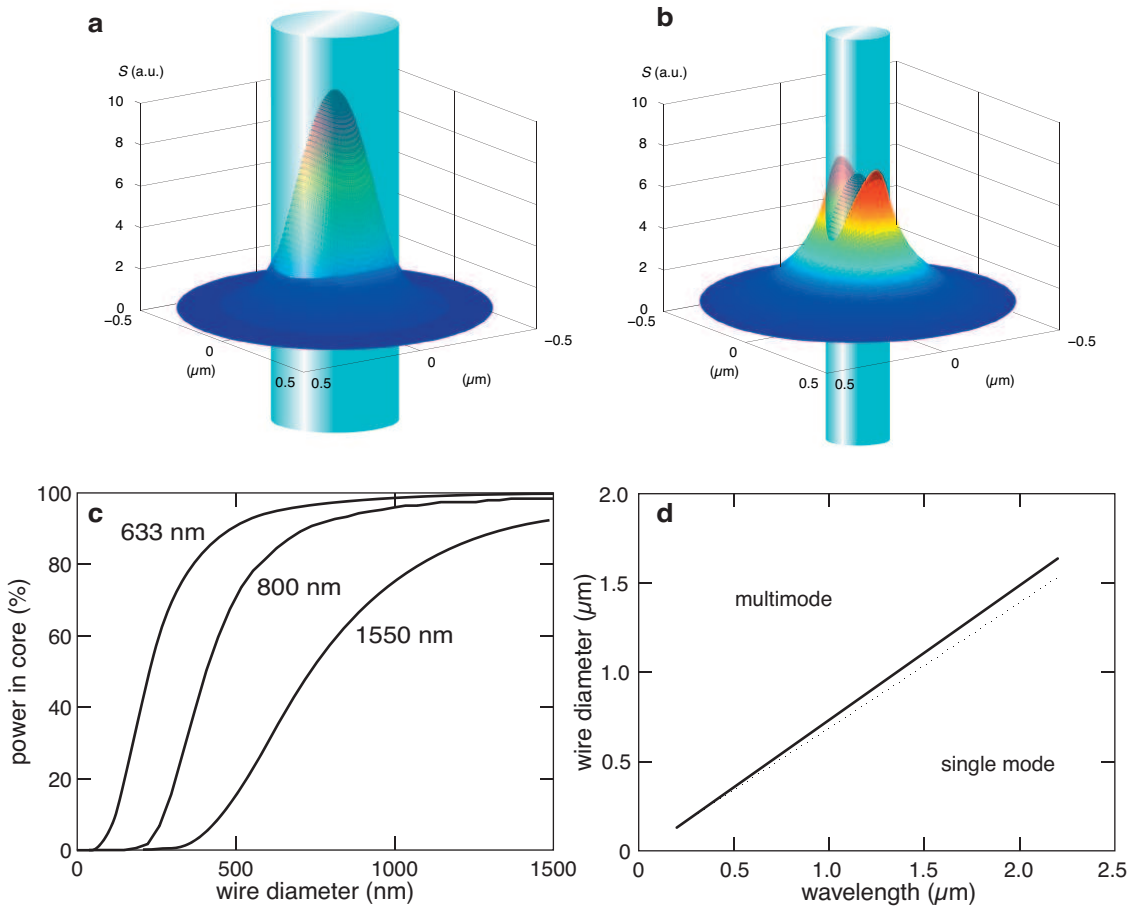

Figure 2.2: (a) The calculated Poynting vector for the fundamental mode of 633-nm wavelength light in a silica nanowire with diameter 400 nm and (b) 200 nm. (c) The integrated power in the core as a function of nanowire diameter for 633-nm, 800-nm, and 1550-nm wavelength light. (d) The calculated critical diameter for single mode operation as a function of the wavelength of light. After Refs. [30, 31].

nanowire diameter. For diameters greater than 700 nm, the dispersion is anomalous (shaded area). In this region, shorter wavelengths travel faster than longer wavelengths and pulse compression can occur. In the normal dispersion regime (diameters less than 700 nm), there exists a large fluctuation in the values for total dispersion, reaching a minimum value of -4.1 ns nm^{-1} km^{-1} for 350-nm diameter. The total dispersion value at this minimum is about 50 times larger than the bulk material value at the same wavelength, showing

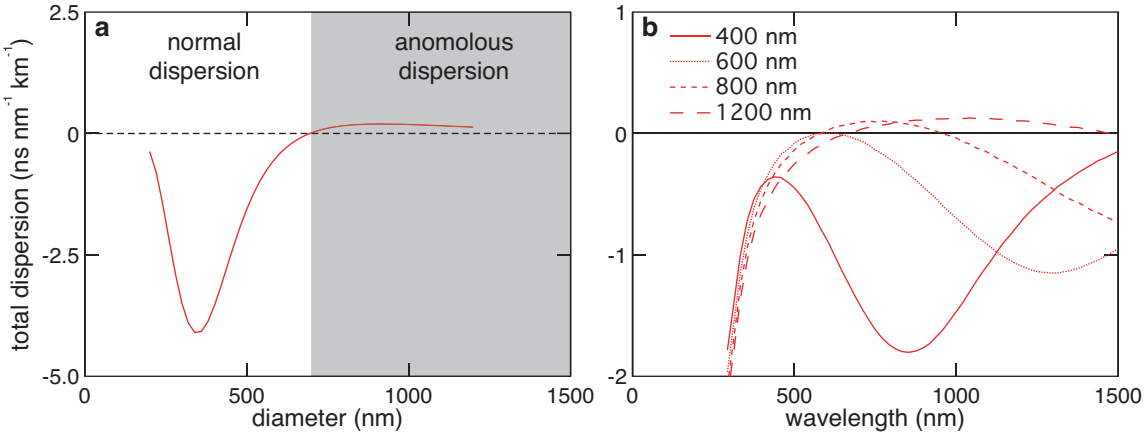

Figure 2.3: (a) Total dispersion (waveguide plus material) for a laser pulse with wavelength centered around 800 nm. The shaded area indicates the region of anomalous dispersion. (b) Total dispersion as a function of wavelength for different fiber diameters.

that the waveguide dispersion term completely dominates the behavior of light in nanoscale waveguides.

Another important optical property is the wavelength where the dispersion crosses zero. Figure 2.3b plots the dispersion as a function of wavelength for different nanowire diameters. The nanowire diameter dependence is strong enough to shift the zero dispersion crossing by several hundred nanometers (to around 600-nm wavelength for a 600-nm diameter fiber) from the bulk material zero crossing around 1.3 μm. This implies that a specific nanowire diameter can be chosen to propagate a pulse with center wavelength from 600-1500 nm with zero dispersion.

2.2 Fabrication of silica nanowires

In the previous section, we discussed the waveguiding of visible light in silica fibers. The waveguide modes in a cylindrical dielectric material have been well-studied over the past 50 years [27]. Even though the critical diameter for single mode operation, which scales

with λ/n, using visible light was known for many years, it remained a technical challenge to produce silica optical fibers with sub-micrometer diameters that were smooth, uniform, and strong. Reports on silica fibers with tiny dimension date back to 19th century [32, 33], but limited knowledge of waveguide theory and the lack of experimental tools, in particular the scanning electron microscope (SEM), for characterizing the size and roughness restricted the investigations to mechanical studies of these fibers. Within the past five years, though, we have seen dramatic developments in the fabrication of nanoscale optical fibers and in the application of these nanoscale fibers in novel photonic devices.

There are currently various techniques for achieving nanometer scale silica fibers with smooth surfaces [25, 34, 35, 36, 37, 38, 39]. We initially demonstrated fabrication through a two-step pulling process assisted by a sapphire tip [25]. Since the first demonstration, sub-micrometer diameter silica wires have been fabricated through flame-brush tapering [34, 40, 41], CO_2 heated oven [42], and directly from a piece of bulk glass, from both active [39] and passive [37, 39] materials.

Figure 2.4 describes the fiber pulling technique used to obtain all the fibers described in this chapter. First, an optical fiber is heated under a flame and drawn to the point of breakage at roughly 2-5 micrometers in diameter. The tapered micrometer-diameter silica fibers float around with the surrounding air currents and have a large Van der Waals attraction to any surface they touch. In the second step, shown in Figure 2.4a, a sapphire taper of about 100 μm diameter [43] is used to mechanically stabilize the fiber near the flame. The micrometer-diameter fiber obtained in the first step is wrapped around the sapphire tip as shown in Fig. 2.4b. The sapphire is placed partially in the flame, absorbing the flame's heat. As heat diffuses along the sapphire taper, the tip's temperature stabilizes, minimizing fluctuations from the flame. The temperature of the tip is reduced to slightly below the melting point of silica ($\sim 2000^{\circ}$C) but still above the softening point (1600°C) [44].

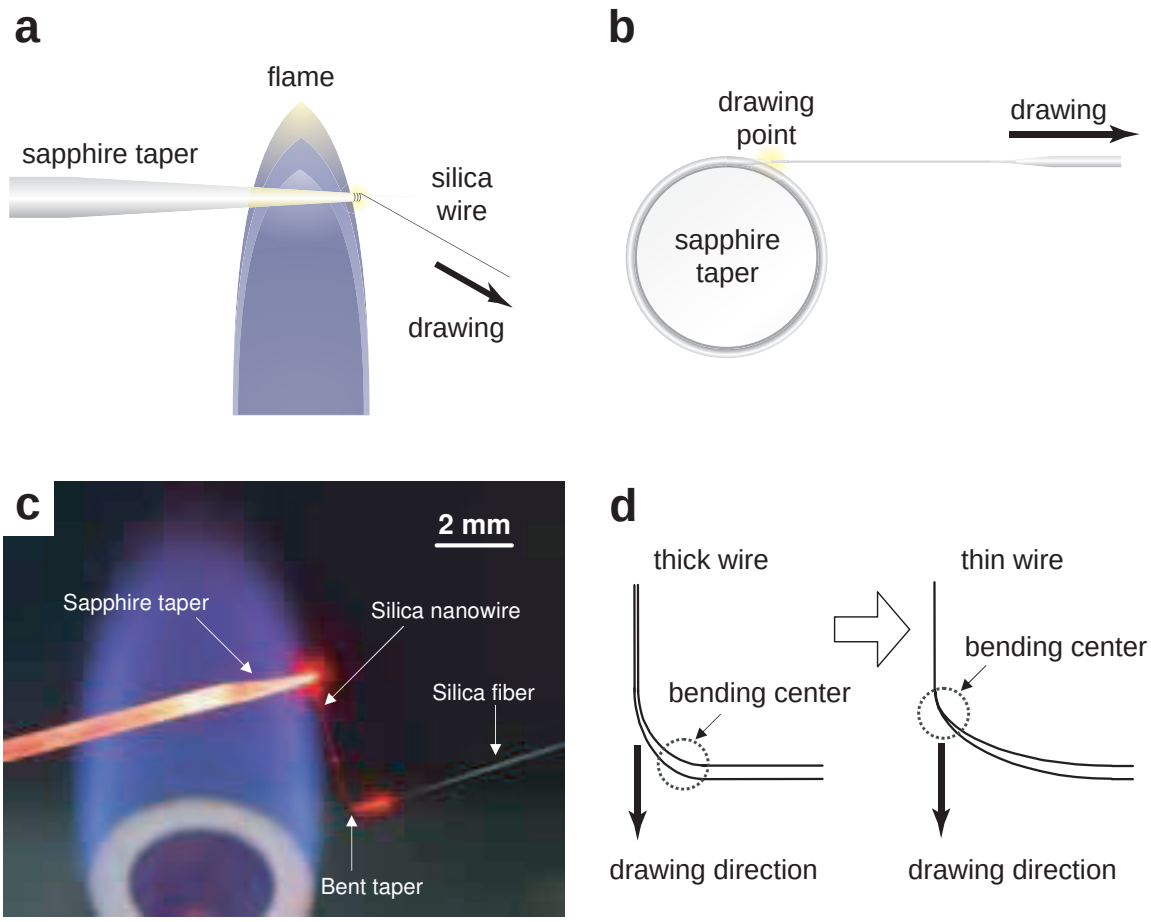

Figure 2.4: The second step in the fabrication process of silica submicrometer- and nanometers fibers. (a) Schematic diagram of the drawing of the fiber from a coil of a micrometer-diameter silica fiber wound around the tip of a sapphire taper. The taper is heated with a CH_3OH torch with a nozzle diameter of about 6 mm. The wire is drawn in a direction perpendicular to the sapphire taper. (b) Magnified view of the drawing process. The sapphire taper ensures that the temperature distribution in the drawing region remains steady. (c) Photograph of the self-modulating taper drawing procedure. The silica nanowire is illuminated by scattering helium-neon laser light. (d) Diagram showing the self-modulation technique using the the bent taper region to produce silica nanowires as small as 20 nm in diameter.

The stability of the heat source is crucial for pulling sub-micrometer diameter fibers with a smooth surface [45].

Figure 2.4c is a photograph of the second step in the pulling procedure [38]. The

silica nanowire is illuminated by scattered helium-neon laser light coupled into the standard optical fiber. We hold the standard fiber at a right angle to the drawing direction to create a bend in the tapered region that "self-modulates" the tension applied to the nanowire according to its thickness, as described in Figure 2.4d. The variable tension is more forgiving of small temperature fluctuations. The standard fiber is pulled away from the wrapped fiber until breaking, yielding a nanowire. Using this technique we can fabricate silica wires with diameters as small as 20 nm with lengths up to several tens of millimeters [38].

With this two-step technique, the resulting nanowire is still attached to the micrometer fiber, which is attached via taper to the original standard fiber. Depending on the application, the nanometer side can be cleaved as shown in Figure 2.10, but for most applications, in particular optical measurements that require coupling to macroscopic sources and detectors as described in Fig. 2.11, the nanowire connected to the standard optical fiber is convenient.

The experiments described in Chapters 3 and 4 demand both input and output coupling of light to the silica nanowires. We fabricated the nanowires for those experiments with a conventional fiber tapering setup shown in Figure 2.5. The preform optical fiber is held by fiber mounts on computer-controlled stages. A hydrogen torch heats the fiber while the stages pull apart at speeds ranging 0.1-1 mm/s. The resulting connected nanowires have sub-micrometer dimensions up to a couple of centimeters in length and minimum diameters as small as 90 nm.

Regardless of the choice of method selected to manufacture a sub-micrometer fiber, the choice of a heat source is of crucial importance. We use a CH_3OH fueled flame for our two-step method and a hydrogen based flame for our conventional tapering rig. Both flames have very low carbon content which helps avoid contamination of the fiber surface with soot or other incompletely burnt particles. Stability of the flame under external perturbations

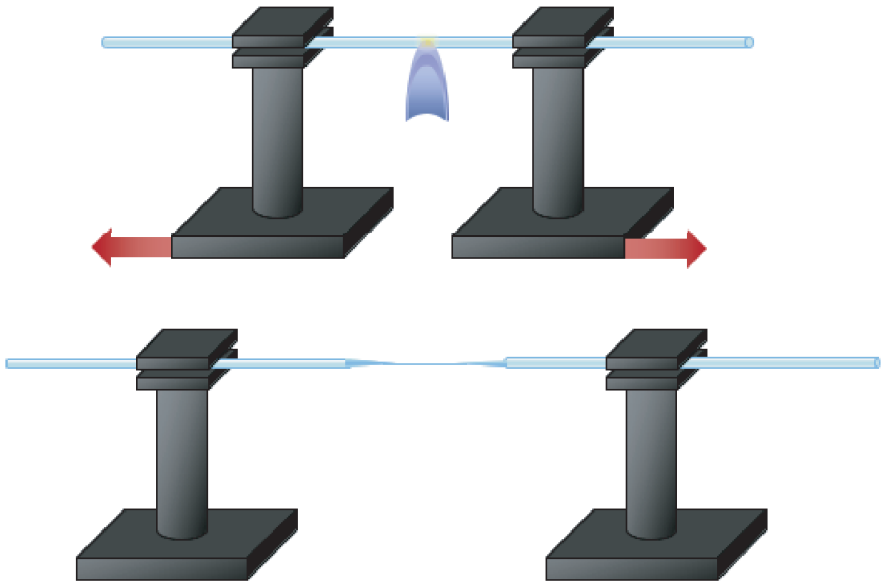

Figure 2.5: Schematic diagram showing the computer-controlled fiber drawing process. A standard optical fiber is placed in two fiber mounts attached to computer-controlled stages that pull at a chosen velocity for a specified distance. The optical fiber is heated with a hydrogen torch using a mass-flow controller to meter out reproducible gas flow.

such as air currents and fuel flow is critical for any pulling system to yield consistent results.

2.3 Characterization of silica nanowires

In this section, we examine the nanoscale silica wire fabricated using the process described in the previous section. We characterize the nanoscale size, uniformity, and roughness of the silica nanowires using an electron microscope. We also take advantage of the mechanical properties of the nanowires to manipulate and arrange them into specific geometries. These techniques are crucial for the linear and nonlinear photonic devices we will study in the upcoming sections and chapters.

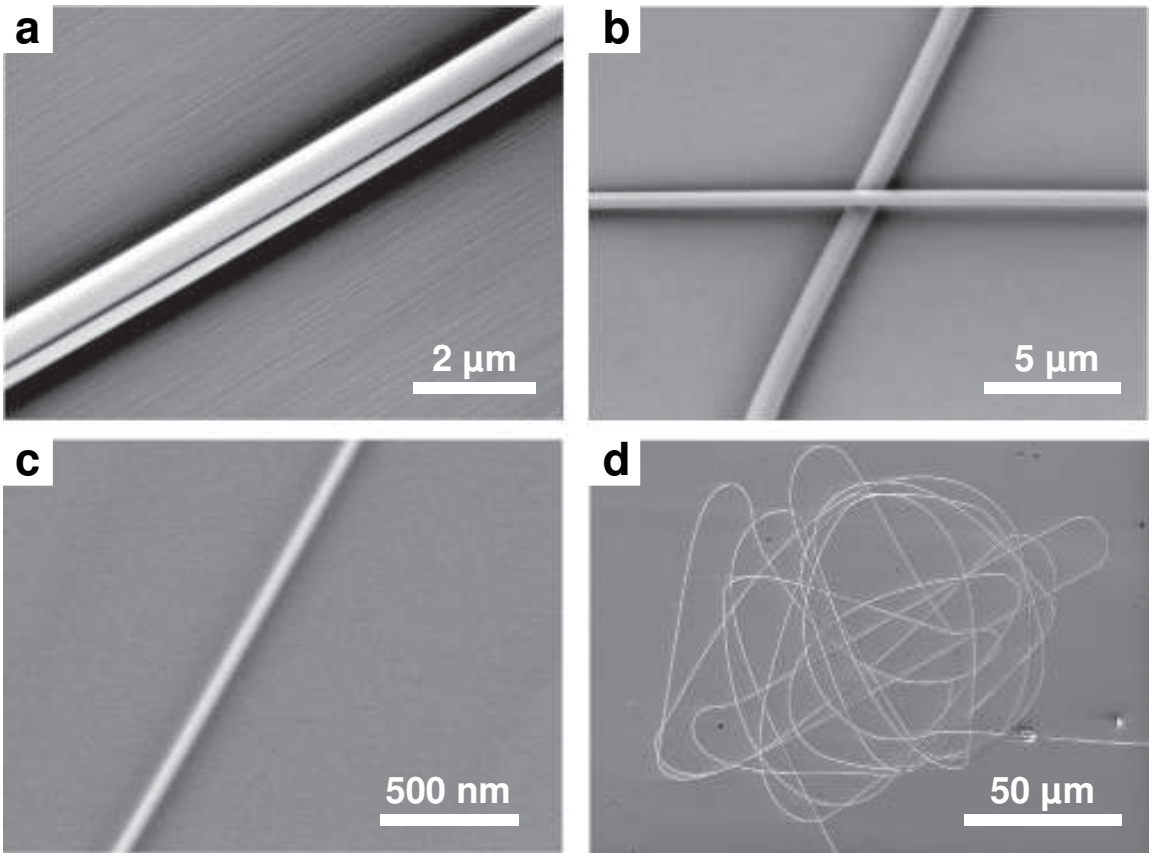

Figure 2.6: Scanning electron micrographs of silica nanowires. (a) Two parallel 170-nm and 400-nm fibers. (b) Two crossed fibers with 570-nm and 1,100 nm diameters. (c) A silica nanowire with a diameter of about 50 nm. (d) A coiled 260-nm diameter fiber with a total length of about 4 mm.

Figure 2.6 shows a collage of scanning electron microscope images of nanowires with various diameters [25]. Figure 2.6a and b shows various sizes of nanowires assembled in different geometries with a fiber of about 50 nm diameter shown in Figure 2.6c. Although only a small section of fiber is shown in Figure 2.6a-c, the overall length of the fiber exceeds millimeters with incredible uniformity. Figure 2.6d displays a single nanowire manually coiled and attached via Van der Waals attraction to a silicon substrate in order to show the large aspect ratio between length and diameter. The maximum diameter change over the more than 4 mm of 260-nm fiber is 8 nm, demonstrating a uniformity of 10^{-6}.

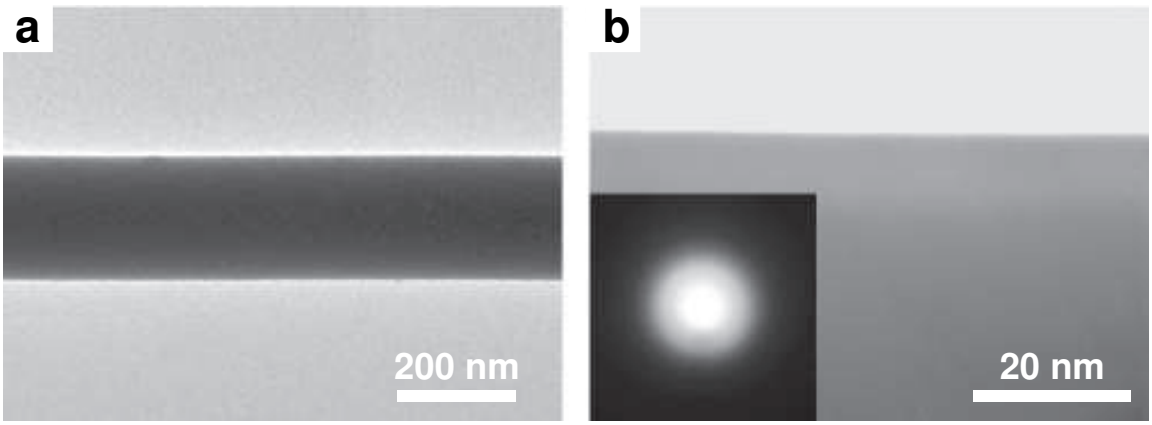

Figure 2.7: Electron images of silica nanowires. (a) TEM image of a 240-nm fiber. (b) TEM image of the surface of a 330-nm silica fiber; Inset: Electron diffraction pattern demonstrating the fiber is amorphous.

Figure 2.7a and b are higher magnification images using a transmission electron microscope (TEM) of the nanowire surface to examine the smoothness [25]. From Fig. 2.7b, we observe that the fiber's surface roughness is less then 0.5 nm with the upper bound is set by the resolution of the TEM used to obtain image. This roughness is comparable to the 0.16 nm bond distance between Si and O in the SiO_2 molecule [44]. We confirm that the molecular structure of the fiber remains amorphous by using electron diffraction shown in the inset of Fig. 2.7b.

The large aspect ratio between the diameter and the length of silica nanowires result in a large flexibility. Figure 2.8 shows how nanowires can be bent, tied, and twisted without breaking. In Figure 2.8a a 520-nm diameter wire is tied into a knot with a 15 μm diameter. Silica nanowires can be bent to even smaller radii of curvature, which gives estimated tensile strength is on the order of 5GPa. [25]

The nanowire bends shown in Fig. 2.8 are elastic in nature, which means the nanowire remains under tension in order to maintain its shape. When the tension is released, the nanowire straightens out. As mentioned above, the dimensions of these silica nanowires

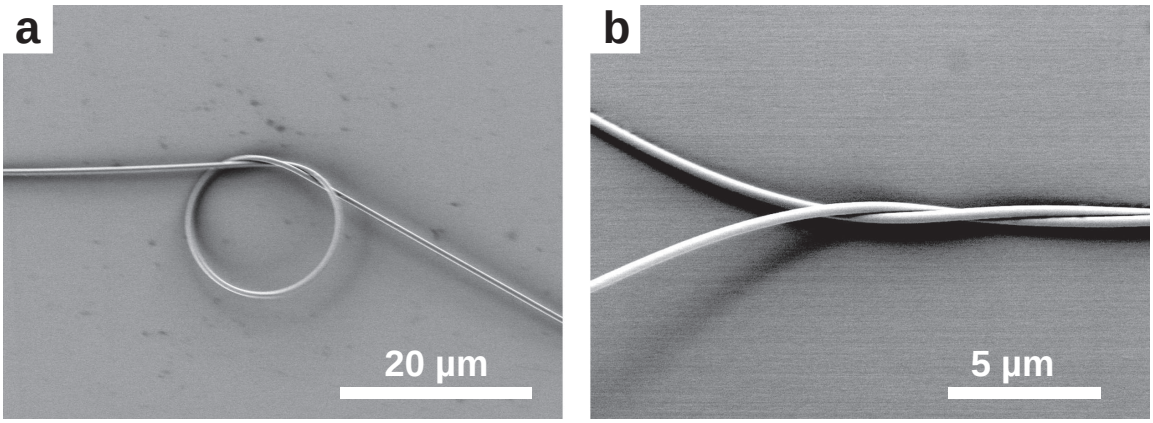

Figure 2.8: SEM images of the flexibility and strength of silica nanowires. (a) A 15 μm diameter ring made with a 520-nm diameter silica wire. (b) A pair of twisted 330-nm diameter wires.

are small enough that the Van der Waals attraction provides a strong contact force to other surfaces. We use this force not only to immobilize the nanowires on a substrate, but also to bond one nanowire to another.

Figure 2.9 shows plastically bend silica nanowires [46]. We create these geometries by elastically bending the nanowires on a sapphire disk, then thermally annealing for about two hours at 1400 K. The elastic bends become permanent during the annealing, which provides a technique for avoiding long term fatigue due to bending stress [47, 48].

The tight bends in Figure 2.9b and d are particularly useful for small scale photonic devices. These figures show that both smooth and sharp bends with radii of curvature smaller than 5 μm are possible. Unlike planar photonic structures where multiple layers are involved, the dimensions of a bend are dictated only by the fiber size. In addition, contrary to other technologies including photonic crystals and semiconductor nanowires, the bent silica fiber guides light in broadrange of wavelengths, from at least 325 to 1550 nm [46]. As a reference, the bending radius in optical fibers is on the order of centimeters [49], in SOI integrated devices 10 μm and in photonic crystals about 1 μm [50].

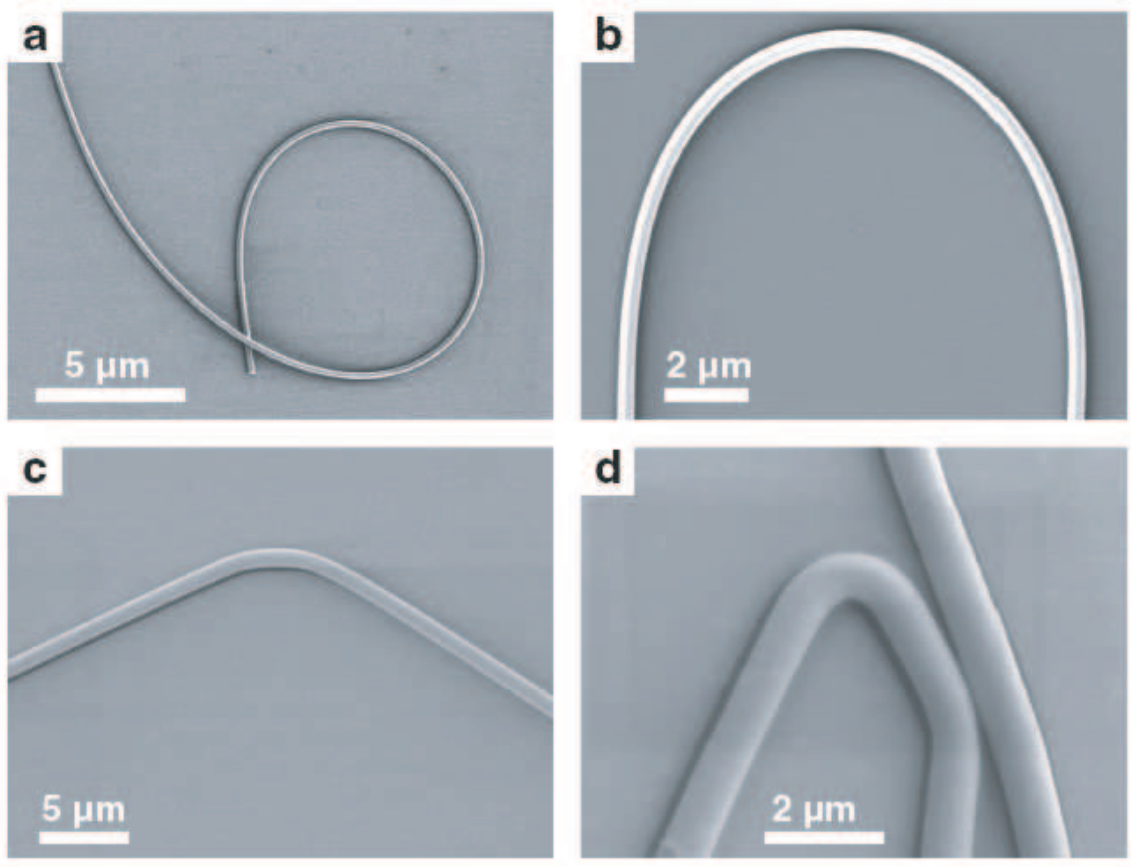

Figure 2.9: SEM images of silica nanowires with plastic bends. (a) A 9-μm diameter loop on a sapphire substrate formed by elastic bending of a 200-nm diameter fiber. (b) A plastic bend in an annealed 410-nm diameter wire on a sapphire substrate. (c) Double plastic bends in a 940-nm diameter fiber. (d) Double bend in a 800-nm diameter wire. The sharp bend has a radius of less than 1 μm.

The silica nanowires are flexible because of their high aspect ratio, but they can also be cut to specific lengths as shown in Figure 2.10 [46]. Using a pair of sharp metallic tips to hold the nanowire along one edge, a third tip can be positioned to apply pressure to the point of breaking the nanowire. Figure 2.10a shows the cleaved end of three different sizes of nanowires. By repeating this procedure we obtain isolated silica nanowires of a desired length, as shown in Fig. 2.10b. Silica nanowires can be cut in this fashion and combined with semiconducting or metallic nanowires into heterostructures.

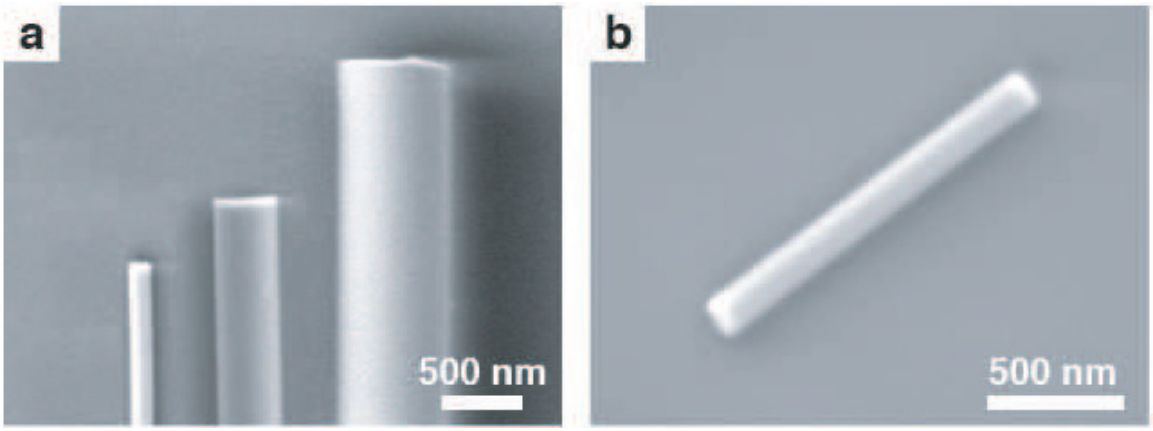

Figure 2.10: SEM images of cleaved silica nanowires. (a) 140-,420- and 680-nm diameter fibers. (b) A 1.5 μm long segment cut from a 160-nm diameter fiber.

2.4 Optical properties of silica nanowires

In the previous section, we examined the physical characteristics of silica nanowires. We measured the nanowire surface smoothness down to the molecular level, and observed extremely high uniformity over long lengths. These two features are important in order for the nanowires to act as the dielectric waveguides we studied in Section 2.1. In this section we show that the silica nanowires we fabricate conduct light similar to standard optical fibers, but with some important distinctions.

Coupling light into a sub-micrometer diameter silica fiber, or any other nanostructure, is not a trivial task because the feature size is often smaller than the diffraction-limited focal spot for visible light. Typical coupling of light into optical fibers requires a microscope objective whose numerical aperture matches that of the optical fiber, which is mounted on a three-dimensional stage (or six-dimensional stage, for higher efficiency) to optimize the throughput. The dimensions of the nanowires make this direct focusing method extremely inefficient. As mentioned in Section 2.2, our fabrication techniques create silica nanowires that are still attached on one or both ends to standard optical fiber by a tapered region.

We can therefore couple into the standard optical fiber by the usual method, and light can propagate along the tapered region into the nanowire. The efficiency of the tapered region depends on how adiabatic the shape of the taper is [29], which is determined by the fiber pulling parameters. Frequently, the specific application determines whether we fabricate a long, gradual tapered region with high efficiency or an abrupt sharp tapered region with low efficiency. In either case, some fraction of the power is coupled via taper to the waveguiding modes (often only the fundamental mode) of the silica nanowires.

Figure 2.11a describes how we couple from one nanowire to another. Light is coupled into a fiber taper and the large evanescent field shown in Figure 2.2 allows for touching nanowires to couple. Figure 2.11b experimentally demonstrates evanescent coupling to a nanowire with 633-nm light. The coupled light propagates along the fiber and can be observed from the scattering along its length from contamination on the surface by dust. The large amount of scattering seen in Figure 2.11b amounts to only a small fraction of the amount of the power being transmitted. Fig. 2.11c confirms light is guided mostly along the fiber by purposely intercepting a fiber to induce the scattering of guided light.

Using the coupling scheme described in Figure 2.12a, we can measure the propagation losses of different size fibers. By changing the input coupling location along the suspended wire, we measure the amount of signal lost for different lengths and determine the transmission loss directly. Figure 2.12b shows the loss values for 633 nm and 1550 nm [25]. Propagation losses can be reduced substantially by limiting surface contamination from the environment [46] and by measuring loss directly while pulling the nanowires [51, 34].

The wavelength dependence of the losses can be understood from the theoretical calculations modeling light propagation in nanowires in Section 2.1. From Figure 2.2c, we see that for a given wavelength, the power in the core decreases with decreasing nanowire diameter. We can also understand the source for higher transmission losses at longer wave-

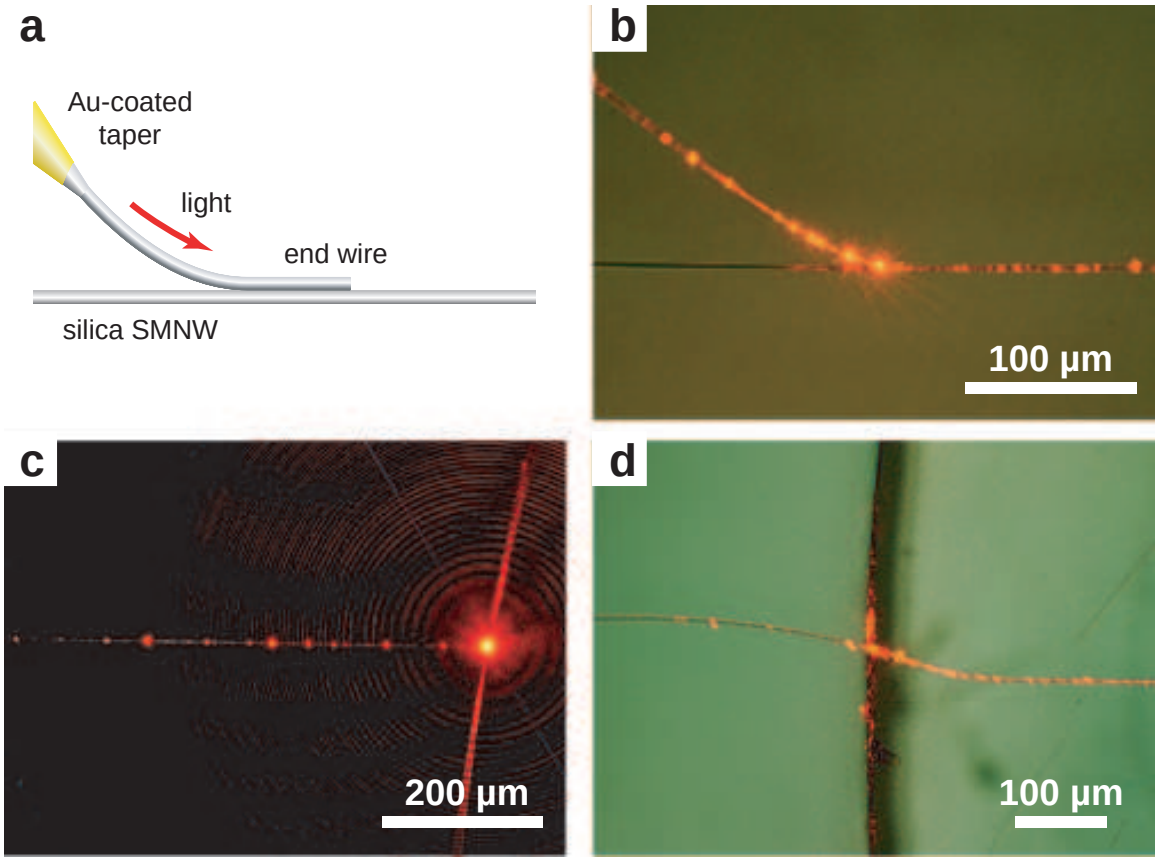

Figure 2.11: Light coupling into silica nanowires. (a) Schematic diagram for launching light into a silica fiber using evanescent coupling. (b) Optical microscope image of a 390-nm diameter taper coupling into a 450-nm diameter silica fiber. (c) Long time exposure image of a 633-nm wavelength light guided by a 360-nm diameter fiber in air and intercepted by a 3-μm fiber on the right. (d) Optical microscope image of 633-nm wavelength light guided in a 550-nm diameter fiber. The left half of the fiber is suspended in air, while the right side is supported by a MgF_2 crystal ($n = 1.37$).

lengths. For a given nanowire diameter, the longer wavelengths have less power in the core, thus larger evanescent waves than shorter wavelengths. The light that is the outside the core will interact with any environmental perturbations at or near the surface, including particles of dust or microbends. Thus the greater the evanescent field the higher the transmission losses.

As shown in Section 2.1, silica nanowires are able guide light with tight confinement

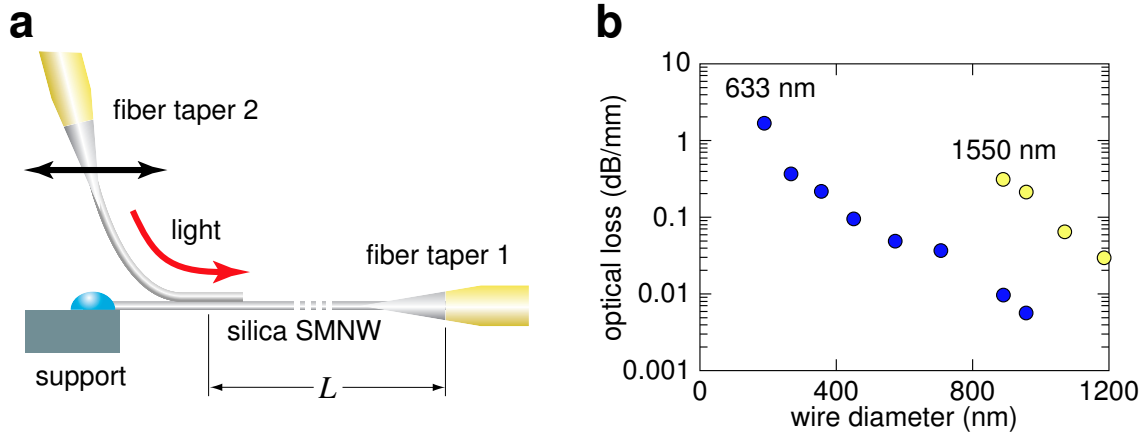

Figure 2.12: Optical loss measurement of silica nanowires. (a) Optical loss measurement scheme. Fiber taper 2 is attached at different points along silica nanowire thereby changing the length of propagation. (b) Measured optical loss of silica fibers at 633-nm (filled circles) and 1550-nm (hollow) wavelengths.

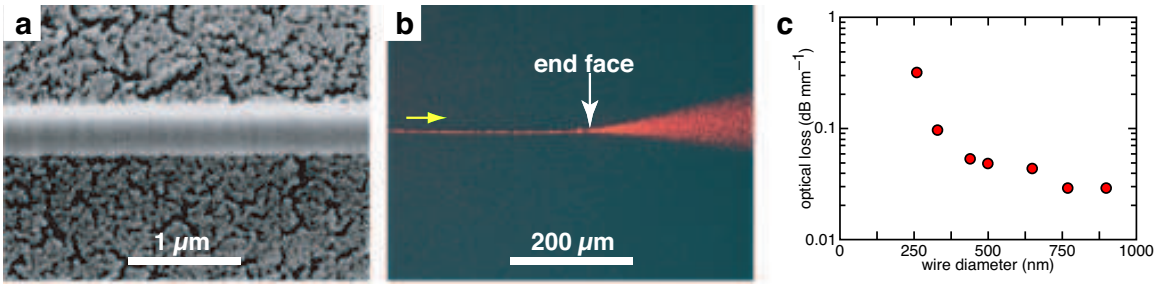

Figure 2.13: Guiding of light by straight and curved silica nanowires mounted on a silica aerogel. (a) SEM image of a 450-nm fiber supported on a aerogel. (b) Optical microscopy image of a 380-nm diameter fiber guiding 633-nm wavelength light on the surface of an aerogel. The left arrow (yellow) indicates the direction of light propagation; at the right end of the wire, the light spreads out and scatters on the aerogel surface. (c) Measured optical loss of straight aerogel supported fibers for 633-nm wavelength.

due to the large index contrast. When using freestanding silica nanowires we maintain the large contrast due to the surrounding air, but when we place the nanowires on a substrate the index contrast decreases, in some cases completely. The large index contrast requirement limits the uses of the nanowires because they cannot be supported on most substrates. There are some low index materials, such as MgF_2 crystal, which has an index $n = 1.37$,

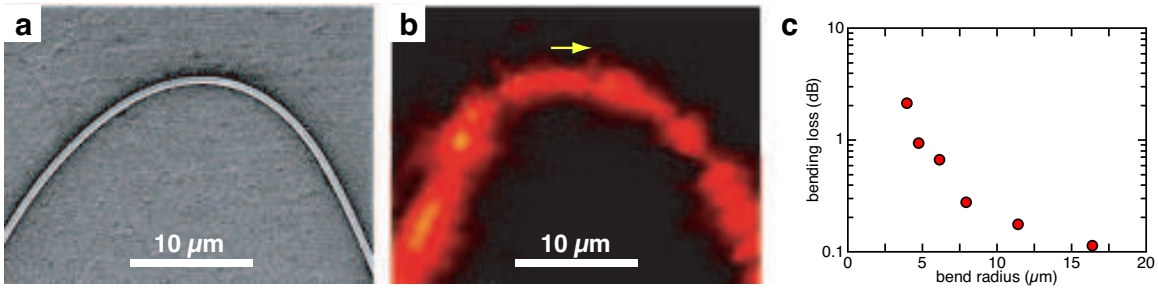

Figure 2.14: Guiding of light by and bending losses of curved silica nanowires supported on a silica aerogel. (a) SEM of a 530-nm fiber supported on an aerogel with 8 μm radius of curvature bend. (b) Optical microscopy of the 530-nm aerogel-supported fiber guiding 633-nm wavelength light across the bend. (c) Measured bending loss in a 90° bend in aerogel-supported 530-nm wide wires at a wavelength of 633 nm.

that can be used for supporting silica nanowires, but, as shown in Figure 2.11d, the decrease in contrast causes an increase in scattering.

To tackle this problem we began using mesoporous materials, such as silica aerogel, as substrates for silica nanowires. The silica aerogel is a tenuous network of pores, on the order of tens of nanometers [52, 53], and is ultimately composed of more than 90% of air. This trapping of air makes silica aerogel an excellent thermal insulator, and it also reduces the refractive index to as small as 1.05. Recently, we also began using glass substrates coated with a mesoporous silica layer of about 800 nm in thickness [54, 55]. The mesoporous silica layer has an index of refraction of about 1.18 or less.

We can compare the optical properties of silica nanowires supported by aerogels to freestanding wires. Figure 2.13a shows a nanowire on top of an aerogel surface under SEM. Figure 2.13b shows light propagating along a nanowire then diverging from the end facet. The measured losses in nanowires supported with aerogels are in fact lower than the first reported losses for free standing wires in Figure 2.12. These results imply that we can use aerogel substrates with minimal perturbation to the waveguiding properties of the silica nanowires.

The bending loss for nanowires supported on aerogel substrates is measured in Figure 2.14a-c and shows that the minimum bending radius is on the order of 5 μm. The bending loss presented in Figure 2.13c was measured for a 530-nm diameter wire supported on an aerogel substrate [46]. The bending loss is calculated by slowly increasing the radius of curvature of the bend while maintaining the input and output coupling fixed. The loss due to tight bending ultimately sets a limit for the density of integration for devices assembled from silica nanowires.

2.5 Applications

There are a variety of interesting applications for nanoscale optical waveguides including near-field imaging, biological and chemical sensing, laser-induced breakdown spectroscopy, atom cooling and trapping, nano-lasing, and optical computing. In this section, we will focus on a couple of applications that play a role in the experiments in Chapter 4. Specifically, we will look at 2×2 coupler using a pair of touching silica nanowires, and a micro-ring resonator assembled from a silica nanowire loop.

We create a 2×2 linear coupler by putting two nanowires wires in contact. The evanescent field of one nanowire overlaps with the other, creating coupled modes which cause the power distribution to oscillate from one nanowire over a characteristic length. If the region where the nanowires touch can be tuned across the characteristic length, the transmission can vary from a 100:0 coupler to a 50:50 coupler. Simulations for silica nanowires calculate that this change can occur over a region as small as 5 μm [46]. This is 20 times smaller than the usual 100 μm overlap region in integrated devices [56].

Figure 2.15a shows the experimental demonstration of a coupler that confirms the dimensions from the simulation. Light is input at the left side into the bottom nanowire

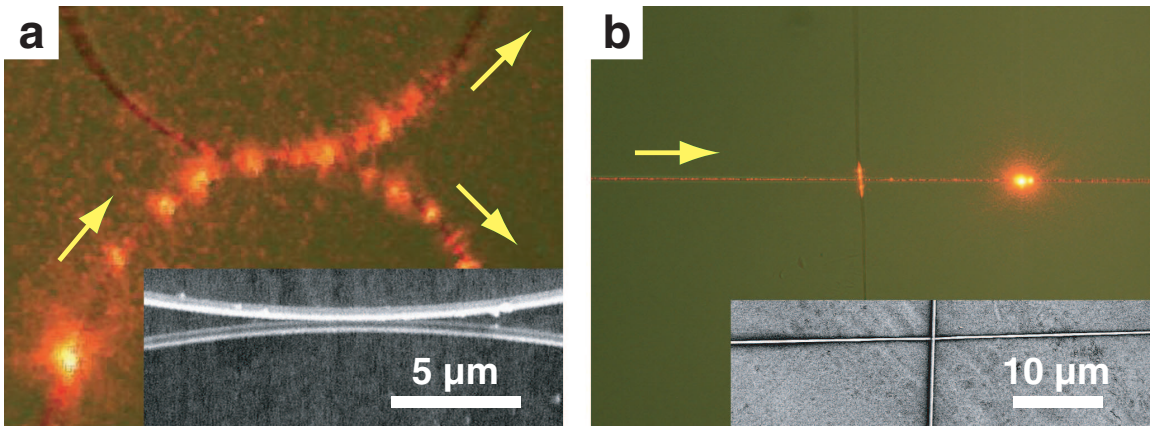

Figure 2.15: Optical coupling between aerogel-supported silica wires. The arrows indicate the direction of light propagation. (a) Optical microscope image of a micrometer-scale 2×2 coupler assembled from two 420-nm wide silica fibers. The two fibers overlap less than 5 μm at the center. Inset: SEM image of the overlap region. (b) Two 390-nm silica fibers intersecting perpendicularly on an aerogel surface. The bright spot on the right is intentional scattering to show the power carried inside the fiber. Inset: SEM close-up of the intersection.

branch and the signal is split into both top and bottom branches in the right side. The coupler acts as a 3-dB splitter with an insertion loss of 0.5 dB [46]. The inset shows an SEM microscopy image of the device with no light inputted, demonstrating the dimensions of the overlap region.

We can understand the 2×2 linear coupler by examining the coupled mode equations [28]

$$\frac{\partial A_1}{\partial z} + \frac{i\beta_2}{2}\frac{\partial^2 A_1}{\partial T^2} = i\kappa A_2 \tag{2.8}$$

$$\frac{\partial A_2}{\partial z} + \frac{i\beta_2}{2}\frac{\partial^2 A_2}{\partial T^2} = i\kappa A_1 \tag{2.9}$$

where A_1 and A_2 are the slowly varying functions describing the electric fields in the nanowires coming into the coupler, and $T = t - z/v_g$ is the relative time. The coupling coefficient, κ, is the result of the overlap of the modes in the two nanowires, primarily due

to the substantial evanescent field. Neglecting dispersion over the length of the coupler, which is reasonable in our case for coupling lengths of about 5 μm, we can solve Eqs. 2.8 and 2.9 assuming only one input along the first nanowire

$$A_1(z,T) = A_0\cos(\kappa z) \tag{2.10}$$

$$A_2(z,T) = A_0\sin(\kappa z) \tag{2.11}$$

where $A_0(T)$ is the shape of the pulse at $z = 0$. The results from Eqs. 2.10 and 2.11 are analogous to coupled finite quantum wells, which exhibit the same sinusoidal oscillations.

Figure 2.15b shows another interesting optical property of coupling in silica nanowires. Unlike electrons flowing in a conducting wire, the efficiency of coupling between two nanowires is angle dependent [57, 58]. For wires crossing at 90° angles, momentum conservation prohibits light from coupling from one wire to another. This implies no crosstalk between crossed wires, which was confirmed experimentally with extinction ratios of 35 dB [46]. The inset in Figure 2.15b shows an SEM image of a supported wire on top of another. The design of integrated photonic devices can take advantage of the lack of crosstalk between perpendicular nanowires to create stacked components in layers, where the angle of crossing determines whether components will interact.

The other application we want to examine that will help us understand our interferometer in Chapter 4 is the micro-ring resonator, which has been experimentally demonstrated [42, 59]. The micro-resonator is composed of two crossing fiber in a geometry similar to Fig. 2.8a. The largest observed quality factors (Q) for these structures are on the order of 10^5 [59]. However, given the low optical losses associated with nanowires, quality factors in excess of 10^{10} are expected to be possible [59].

Figure 2.16 shows a micro-ring resonator we assembled with a silica nanowire. The

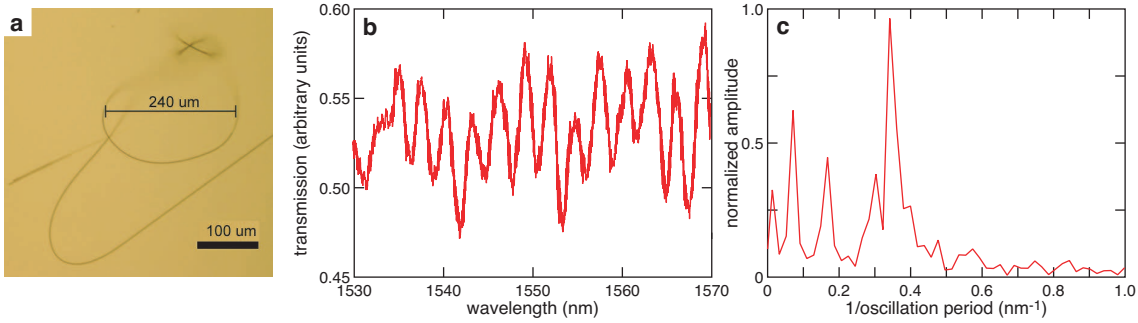

Figure 2.16: A micro-ring resonator assembled from a looped silica nanowire. (a) Optical microscope image the silica nanowire loop after transferring to a glass substrate. (b) The transmission through the micro-ring resonator as a function of input wavelength of light. (c) The power spectrum of the micro-ring resonator obtained by Fast-Fourier Transform of (b) showing a strong resonance 0.36 nm^{-1}.

optical microscope image in Figure 2.16a provides an estimate for the loop size of 240 μm in diameter. The oscillations in Figure 2.16b, and the power spectrum in Figure 2.16c, reveal the resonant behavior of the silica nanowire loop. The strongest peak at 0.36 nm^{-1} gives a periodicity of 2.8 nm, which for $\lambda = 1524$ nm, corresponds to a loop with a diameter of about 260 μm, which agrees well with our estimate from the microscope image. The application of the micro-ring resonator illustrates how we can take advantage of the low loss of the silica nanowires to create a miniaturized device whose operation is based on the specific geometric details of the device.

2.6 Outlook

One of the largest challenges we face when using silica nanowires to study nanoscale optical properties is the assembly into more complex devices. We demonstrated a few of these assemblies, including a coupler and micro-ring resonator, but the manipulation is currently a manual, serial process. Silica nanowires can be shaped into useful geometries to prototype a variety of devices, but the repeatability of a specific structure is still quite

difficult. Another challenge that might help solve the repeatability issue is the ability to fabricate large quantities of nanowires. We have explored other techniques for fabricating nanoscale waveguides including lithography and replication molding, but thus far, the taper-drawn silica fibers, with their low loss, long length, strength and uniformity, have proven to be a reliable tool for studying nanoscale photonics. We can also use silica nanowires in combination with nanostructures created by other means. In particular, in Chapter 5 we use these top-down fabricated silica wires to couple light directly into the waveguide modes of bottom-up grown ZnO nanowires to study their optical properties.

Chapter 3

Nonlinear optical properties of silica nanowires

In the previous chapter, we characterized the physical and linear optical properties of taper-drawn silica nanowires. The large index contrast is responsible for the tight field confinements and strong diameter-dependence of the dispersion. These properties can drastically influence the behavior of a pulse propagating along the nanowire. Over the next few chapters, we explore the potential for using nanoscale optical waveguides to create nonlinear microphotonic devices. In this chapter, we begin by studying the nonlinear optical properties of silica nanowires.

We continue the theoretical treatment of waves propagating in step-index fibers by including the nonlinear polarization that we neglected in Section 2.1. We examine the role of the third-order susceptibility for a nanoscale waveguide with a large evanescent field by calculating a nonlinear parameter that accounts for the size of the mode. We experimentally characterize the silica nanowire nonlinearity as a function of nanowire diameter by observing the spectral broadening (also referred to as supercontinuum generation because

of the continuous spectrum created across hundreds of nanometers) of a femtosecond laser pulse propagating through nanowires [60]. We conceptually discuss the spectral broadening in terms of the diameter-dependent dispersion and nonlinearity, which ultimately provides a range of nanowire diameters that can be used for optimal enhancement of the effective nonlinearity.

3.1 Nonlinear wave propagation in fibers

In this section, we continue the treatment of electro-magnetic wave propagation in a step-index cylindrical dielectric. Recall the wave equation including the response due to the induced material polarization, Eq. (2.1). In Section 2.1, we neglected the contribution from the nonlinear polarization $\mathbf{P}_{NL}$, which typically only changes the refractive index by $< 10^{-6}$ [11]. This small value implies that we can include the nonlinear polarization as a perturbation to the total polarization in Eq. (2.1).

Eq. (1.6) gives the expansion of the polarization in terms of powers of the electric field and the kth-order susceptibility tensor $\chi^{(k)}$. For an arbitrary material, calculating the contribution due to the nonlinear polarization may require many orders of the susceptibility tensor, each of which may have an arbitrary time dependence. We will simplify this complexity by considering an isotropic material whose nonlinear response is instantaneous and maintains the same polarization. These assumptions are appropriate for pulses propagating in silica with pulse durations $> 1ps$. For shorter pulses durations, the temporal vibrational response, or Raman response, of the material can be included as a parameter, T_R, the Raman gain slope, into Eq. (2.1).

By symmetry considerations for an isotropic material such as amorphous silica, the even orders of the susceptibility tensor $\chi^{(k)}$ must vanish. We will focus on the first

nonzero term in $\mathbf{P}_{NL}$, which is the third-order susceptibility $\chi^{(3)}$. The nonlinear polarization becomes

$$\mathbf{P}_{NL} = \epsilon_0 \chi^{(3)} \cdot \mathbf{E} \cdot \mathbf{E} \cdot \mathbf{E}. \tag{3.1}$$

Recalling from Section 2.1, we separate the electric field into a fast oscillation term, a transverse component, which gives the mode profile, and a slowly-varying longitudinal component, which describes the envelope of a pulse, as in Eq. (2.2). We use a Taylor series expansion of the propagation constant β given in Eq. (2.7) to provide useful values such as the group velocity and group-velocity dispersion. Accounting for the simplifications described above, and substituting the electric field and propagation constant into Eq. (2.1), we obtain an equation for the pulse envelope $A(z,t)$ [28]

$$\frac{\partial A}{\partial z} + \frac{\alpha}{2}A + \frac{i}{2}\beta_2\frac{\partial^2 A}{\partial T^2} - \frac{1}{6}\beta_3\frac{\partial^3 A}{\partial T^3} = i\gamma\Big[|A|^2 A + \frac{i}{\omega_0}\frac{\partial}{\partial T}(|A|^2 A) - T_R A\frac{\partial |A|^2}{\partial T}\Big] \tag{3.2}$$

where γ is the nonlinear coefficient, α the absorption coefficient, and T_R the Raman gain slope time. The co-moving coordinate, $T = t - \beta_1 z$, is used to shift to the reference frame of the pulse. The terms on the right hand side of the equation are due to the contribution of the third-order susceptibility to the nonlinear polarization. We define the nonlinear coefficient γ, which absorbs the material and mode information that contributes to the nonlinear wave propagation

$$\gamma \equiv n_2\frac{\omega_0}{cA_{eff}} \equiv \frac{3}{8n}\mathrm{Re}(\chi^{(3)}_{xxxx})\frac{\omega_0}{cA_{eff}} \tag{3.3}$$

where A_{eff} is the effective area of the mode and n_2 is the intensity dependent refractive index coefficient that relates to $\chi^{(3)}$.

The first term on the right hand side of Eq. (3.2) is often referred to as the self-phase modulation (SPM) term, which leads to spectral broadening. The last two terms in

the right hand side of the nonlinear wave equation Eq. (3.2) represent self-steeping and the Raman gain due to the non-instantaneous response, respectively.

Numerical simulations have been used to study pulse propagation under specific conditions [61, 28], but Eq. (3.2) does not have an analytic solution. Since we are examining pulses propagating along a waveguide, one useful way to discuss the various mechanisms in Eq. (3.2) is in terms of the length scale required for a particular mechanism to become significant. If we normalize our variables for the time and the field amplitude to our experimental parameters [28]

$$\tau = \frac{T}{T_0}, \tag{3.4}$$

$$A(z,\tau) = \sqrt{P_0} e^{-\alpha z/2} U(z,\tau), \tag{3.5}$$

where T_0 represents the initial pulse width and P_0 represents the peak power of the incident pulse. The parameters for dispersion and nonlinearity can be represented by particular length scales which we can compare with the nanowire interaction length, L. We define the following characteristic lengths

$$L_D = \frac{T_0^2}{|\beta_2|} \tag{3.6}$$

$$L'_D = \frac{T_0^3}{|\beta_3|} \tag{3.7}$$

$$L_{NL} = \frac{1}{\gamma P_0} \tag{3.8}$$

$$L_s = \frac{1}{\omega_0 T_0 P_0 \gamma} \tag{3.9}$$

$$L'_W = \frac{T_R}{T_0 P_0 \gamma} \tag{3.10}$$

as the dispersion length L_D, the third-order dispersion length L'_D, the nonlinear length L_{NL}, the nonlinear length associated with self-steepening L_s and the Raman length L'_W. These

length scales relate experimental quantities, such as the input pulse power P_0, the initial pulse width T_0, the nonlinear parameter γ and the dispersion of fiber, to the interaction length required to influence pulse propagation. By comparing characteristic lengths to each other, we can determine if one effect will be dominant over the others. We substitute the normalized parameters from Eqs. (3.4,3.5) and characteristic lengths into the Eq. (3.2) yielding

$$\begin{aligned}&\frac{\partial U}{\partial z} + \frac{i}{2}\frac{\mathrm{sgn}(\beta_2)}{L_D}\frac{\partial^2 U}{\partial \tau^2} - \frac{1}{6}\frac{\mathrm{sgn}(\beta_3)}{L'_D}\frac{\partial^3 U}{\partial \tau^3} \\ &\qquad = ie^{-\alpha z}\Big[\frac{1}{L_{NL}}|U|^2 U + \frac{i}{L_s}\frac{\partial}{\partial \tau}(|U|^2 U) - \frac{1}{L'_W}U\frac{\partial |U|^2}{\partial \tau}\Big]\end{aligned} \tag{3.11}$$

which describes nonlinear pulse propagation along a waveguide. Eq. (3.11) shows, when different mechanisms have similar length scales the resulting behavior of the pulse propagation can become rather complex.

3.2 Silica nanowire nonlinearity

In Section 2.1, we calculated the Poynting vector profile and the fraction of the propagating power in the core in Figure 2.2. To understand the nonlinear coefficient γ from Eq. (3.3), we need to use information about the mode profile in order to figure out how the light interacts with the nonlinear material, in our case, the silica. We define a parameter called the mode field diameter (MFD) as the cross-sectional diameter that contains the same fraction of power that a corresponding Gaussian-shaped profile contains within the Gaussian width, w. An equivalent definition for the mode field diameter is $2w$ defined by the effective area $A_{eff} = \pi w^2$ [11].

Figure 3.1 plots the mode field diameter at 800 nm wavelength for nanowires of different diameters. The mode field diameter decreases almost linearly with decreasing core

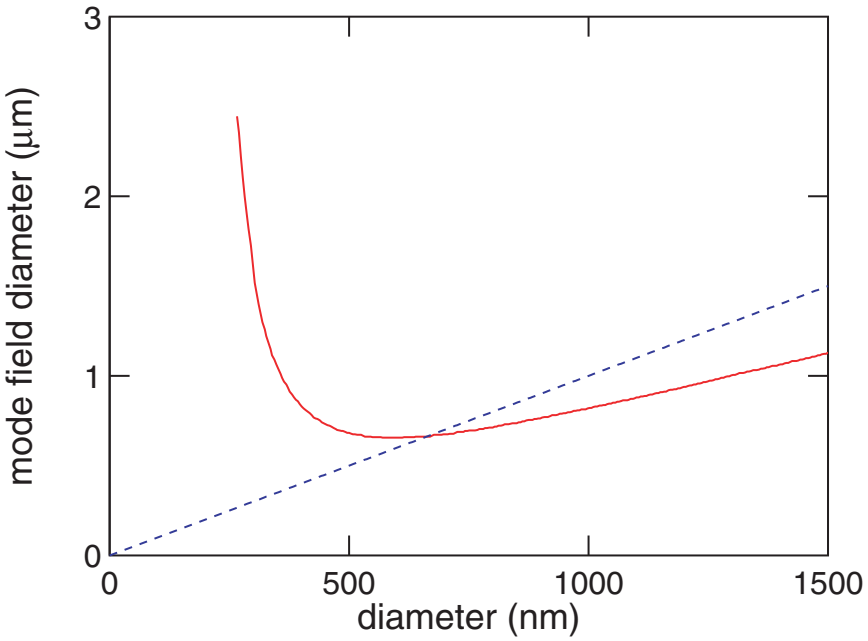

Figure 3.1: Mode field diameter for 800 nm as a function of the nanowire diameter. Dashed line indicates a 1:1 ratio.

size until the core is about the size of the wavelength. The mode field diameter reaches a minimum around when the nanowire is around the size of the wavelength, increasing drastically as the core decreases. The growth of the mode size is observed in Figure 2.2a and b as the larger evanescent field decays exponentially with increasing distance from the core. The dashed line indicates where the nanowire diameter equals the MFD.

We can use the mode field area obtained from Figure 3.1 to determine the diameter region where the mode is the most tightly confined. The nonlinear parameter γ cannot be calculated from the simplified Eq. 3.3 for a silica nanowire because we can see in Figure 3.1 that the mode can spread out beyond the nanowire, therefore the nonlinearity for silica does not completely describe the nonlinearity of the nanowire waveguide. The effective nonlinearity for a waveguide is calculated using the Poynting vector S_z [62].

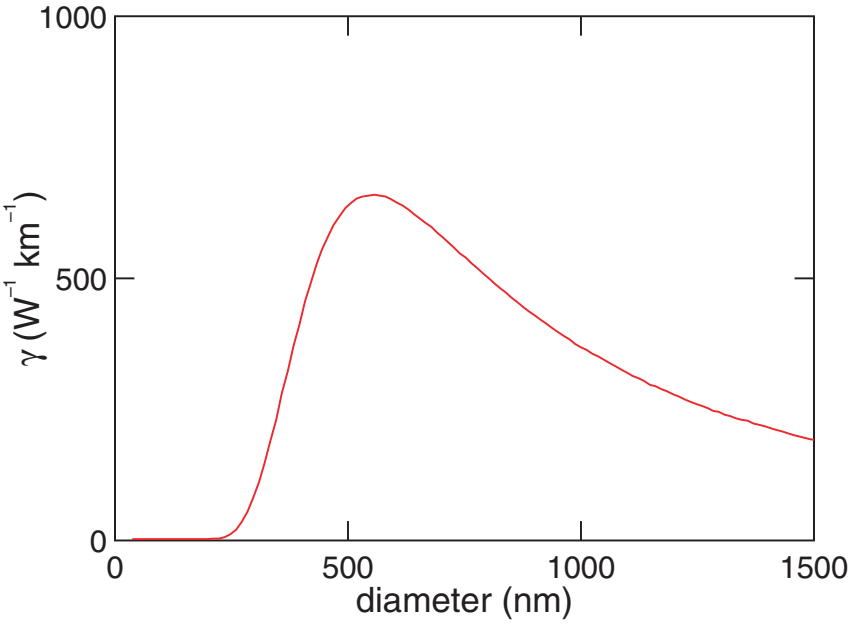

Figure 3.2: Effective nonlinearity (γ) for a 800-nm center wavelength pulse as a function of nanowire diameter. After Ref. [62].

$$\gamma = \frac{2\pi}{\lambda} \frac{\int n_2(\mathbf{r}) S_z^2 d^2\mathbf{r}}{(\int S_z d^2\mathbf{r})^2} \tag{3.12}$$

remembering that the Poyting vector $S_z = (\mathbf{E} \times \mathbf{H}^*)_z$. Eq. 3.12 takes into account the possibility for inhomogeous nonlinear refractive index with n_2 in Eq. 3.12 being spatially dependent. For silica nanowires, the nonlinear index of the air cladding is three orders of magnitude smaller than the that of the silica core, so the integral in the numerator for the effective nonlinearity is restricted to the core.

Figure 3.2 plots the effective nonlinearity γ as a function of the nanowire diameter for a 800-nm center wavelength pulse. As expected from Eq. 3.12, γ resembles the inverse of the mode field diameter shown in Fig. 3.1. For large diameters, the nonlinearity approaches that of bulk silica. At the diameter where the mode field is the smallest (about 550 nm), the nonlinearity peaks at 660 $\mathrm{W^{-1}km^{-1}}$. The peak value for the nonlinearity inside a nanowire

is much larger than those for a standard single mode fiber. The nonlinearity for a 10 μm^2 mode area fiber is 22 times smaller at 30 $W^{-1}km^{-1}$ [11]. For small diameters, as expected from the mode field diameter calculations, the nonlinearity decreases approaching zero for diameters below 300 nm. The vanishingly small nonlinearity is a result of large evanescent field that experiences mostly the nonlinearity of the surrounding air.

3.3 Experimental setup

The behavior of γ calculated in Figure 3.2 shows a strong diameter dependence. In this section, we describe the setup used to experimentally probe the nanowire nonlinearity as a function of diameter by propagating a femtosecond pulse along a silica nanowire.

To fabricate silica nanowires in order to study the nonlinear optical properties of nanoscale waveguides, we used the conventional fiber tapering technique with computer-controlled stages described in Section 2.2. The parameters for the fiber pulling system, including speed, acceleration, tension and position of flame, were optimized to yield relatively large (tens of mm) lengths of nearly constant diameter fiber. We tested both single and multimode fibers, and observed that the final diameter of the tapered fibers were equivalent independent of the initial fiber size (with different fiber pulling parameters). We chose a commercial 50 μm core/125 μm cladding multimode fibers as "preform" for drawing in order to minimize nonlinear effects that might occur in either the standard optical fiber or the tapered region of the fiber. The diameter profile for each pulled fiber was measured using a scanning electron microscope.

The laser pulses for the experiments described below are generated by a 250-kHz femtosecond laser system with 800-nm central wavelength, 90-fs minimum pulse duration and 4-μJ maximum pulse energy. Because the fibers are tapered, the laser pulse propagates

through some length of untapered fiber at the input and output side. Hence, we need to control the dispersion of the input pulse so that a short pulse is delivered at the nanowire part of the fiber. By tuning a grating compressor the pulse's dispersion can be changed, pre-compensating for the input fiber dispersion, and shifting the position of the shortest pulse inside the fiber. For example, we confirmed the delivery of pulses as short as 200 fs at the output of a 25-cm long standard fiber using a commercial autocorrelator.

The output signal from each fiber is directed to a calibrated fiber-based spectrometer and time-averaged for at least 1 μs. The spectral range for all spectra shown is dictated by the calibration light source of the spectrometer, being restricted to the range 380–1050 nm. We measure the overall transmission at 800-nm wavelength light at low intensities for each fiber. We then increase the input laser pulse energy in steps up to the damage threshold of the fiber's front face ($\leq$ 360 nJ) while recording the spectrum.

3.4 Results

Figure 3.3 shows the diameter profiles of six representative nanowires as measured by a scanning electron microscope. The average diameter of the nanowire for the region less than 1-μm of the tapered fibers is shown at the top right of every profile. Although the six fibers shown have different interaction lengths and minimum diameters, we refer to each fiber by its average diameter.

We observe from Figure 3.3 that the tapers on either side are sharp and not necessarily symmetric. As in previously reported experiments [63], significant transmission losses occur at the taper region ($\sim$ 70%). We can fabricate longer tapered regions to reduce the loss in that region, but we want to minimize the interaction length the tapered region which may contribute to the output spectrum, therefore we make a sharp taper. Using this

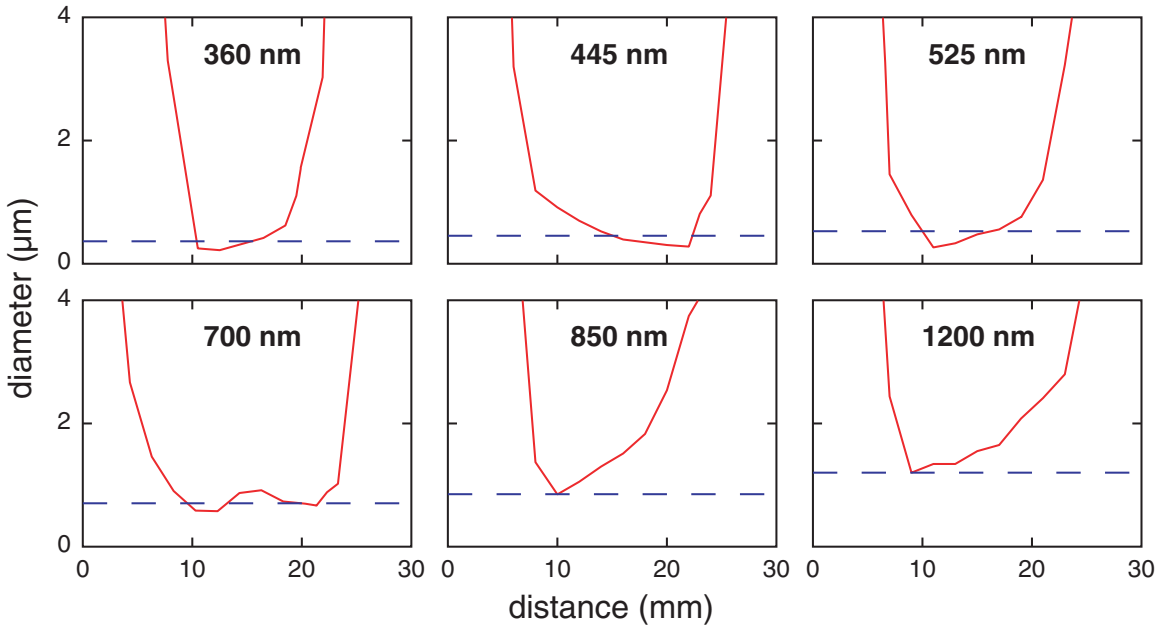

Figure 3.3: Diameter profiles of a set of six representative fibers. The averaged diameter of the sub-micrometer part of the fiber is shown at the top of each figure and indicated by the dashed line.

technique, we neglect the contribution from the tapered region when examining the spectral broadening.

For each fiber shown in Fig. 3.3, we measured the output spectrum generated by a femtosecond laser pulse input. The six spectra in Figure 3.4 are representative of about 30 different spectra taken for fibers with minimum diameters ranging from 90 nm to 1600 nm. Figure 3.4a shows the spectrum for a fiber with an average diameter of 360 nm. The small broadening shown in Fig. 3.4a is insensitive to changes in laser pulse energy ranging from of 150 pJ to 500 pJ. Figs. 3.4b-d show increasingly broader spectra with a growing asymmetry. In Fig. 3.4e we observe a minor reduction in broadening and the disappearance of features in the infrared. The spectrum observed for the 1200-nm diameter fiber (Fig. 3.4f) is clearly distinct from all other spectra in Figure 3.4. There is no transmitted light in the range 500–700 nm, and the spectrum has sharp peaks around 440 nm and in the near

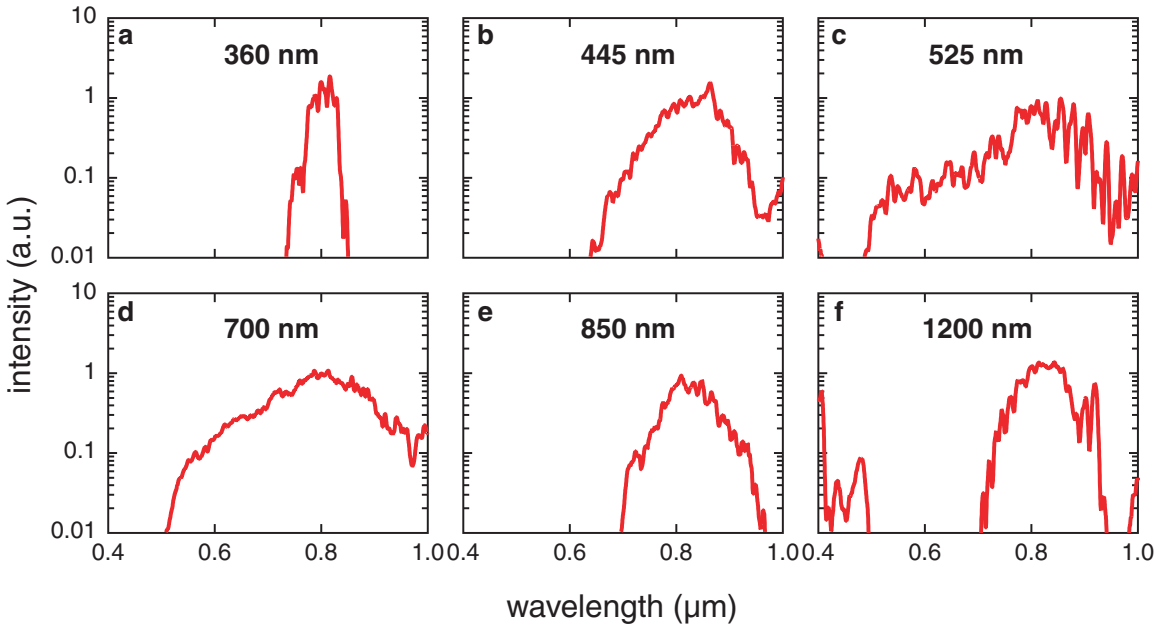

Figure 3.4: Spectral broadening for the six fibers of Figure 3.3. The transmitted pulse energies are 0.3, 4, 6, 4, 7 and 2.5 nJ, respectively.

infrared.

Figure 3.5 shows the evolution of the spectrum shown in Fig. 3.4f as a function of energy. At low energy, Fig. 3.5a, the pulse spectrum broadens in the infrared and displays a number of sharp features. As the energy is increased, sharp features also show up on the blue side. We observe that the features at 415 and 437 nm on the blue side are not the second harmonic frequencies of the two infrared peaks at 900 and 925 nm.

For fibers with an average diameter below 300 nm, we observe considerable variance from fiber to fiber of the amplitude and shape of the spectrum. We attribute the variance to contamination of the surfaces, leading to large wavelength dependent losses. From our definition of average diameter, a sub 300–nm average diameter fiber has a minimum diameter below 200 nm. The mode field at 800-nm wavelength has less than 10% of its power confined inside a fiber with 200-nm diameter (see Figure 2.2c). The large evanescent field is extremely

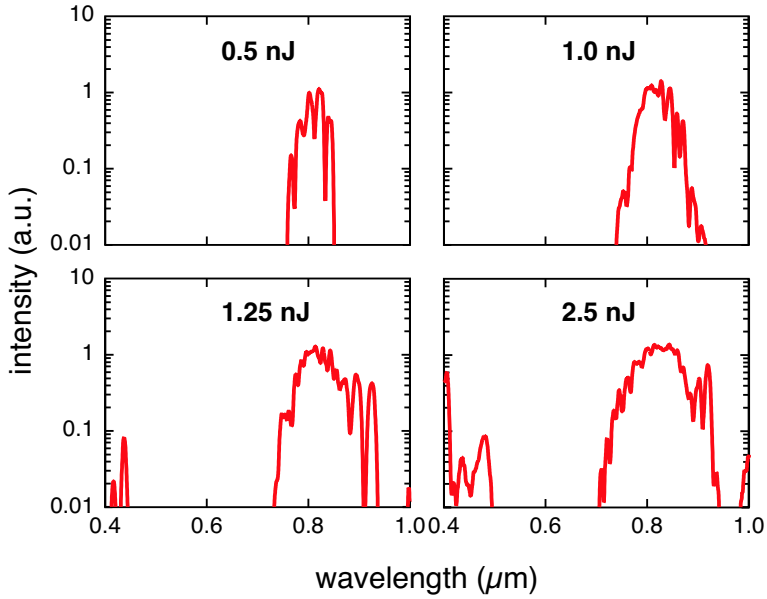

Figure 3.5: Evolution of the spectrum generated by a 1200-nm minimum diameter fiber with increasing transmitted pulse energy.

sensitive to contamination of the surfaces [30]. Any light signal propagating inside a fiber with sub-200 nm diameter experiences significant propagation losses at a wavelength of 800 nm if the surface is contaminated. If we isolate only the spectra with large signal levels (i.e. small losses), the output spectra is nearly identical to the input laser spectrum, indicating that no broadening occurs.

Figure 3.6 shows a qualitative visual inspection of scattered light when femtosecond laser pulses are propagating along silica nanowires. Since 800-nm wavelength light is outside the visual range for our eyes, the colors in the photographs come from one or more nonlinear effects. The smooth progression of colors in Figure 3.6a and b suggest that the nonlinear effects responsible for generating supercontinuum occur in the nanowire region. Figure 3.6c shows a progression of colors as well as bright scattering centers suggestive of surface contamination or abrupt nanowire diameter changes. The scattered light in Figure 3.6d shows a relatively uniform blue color in the nanowire region suggesting the color generation

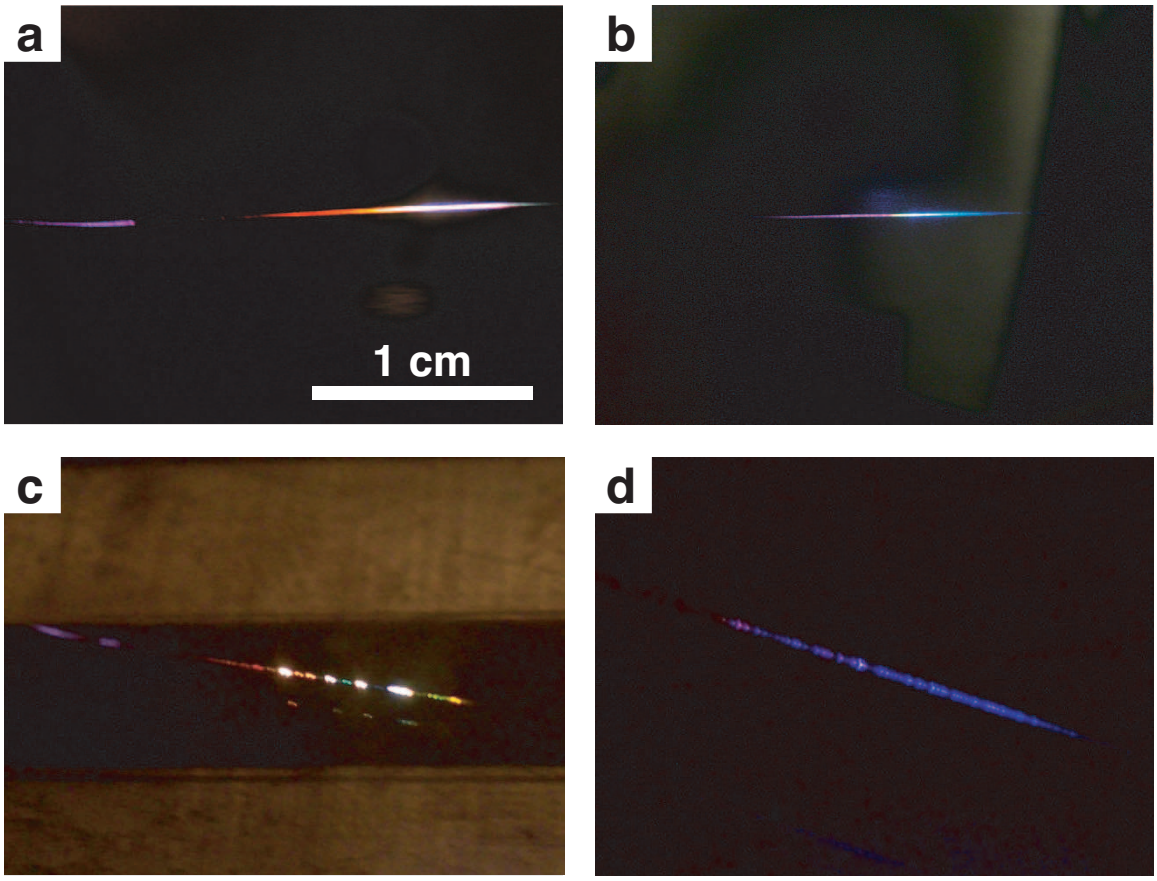

Figure 3.6: Photograph of scattered supercontinuum light generated by femtosecond laser pulses propagating in silica nanowires. The pulses are coupled in from the left side of the pictures and propagate to the right. (a) and (b) Smooth, uniform progression of colors in the scattered light. (c) Uneven scattering indicates surface contamination or abrupt nanowire diameter changes. (d) Scattered light shows no progression in color indicating that the colors may be generated outside of the nanowire region.

occurs in a very short interaction length or outside of the nanowire region.

3.5 Discussion

Previous theoretical calculations show the that the nonlinear parameter γ is highly diameter dependent for a bare silica fiber with nanoscale dimensions [62]. The optimal dimensions for nonlinear interactions in silica nanowires reach a maximum for diameters of

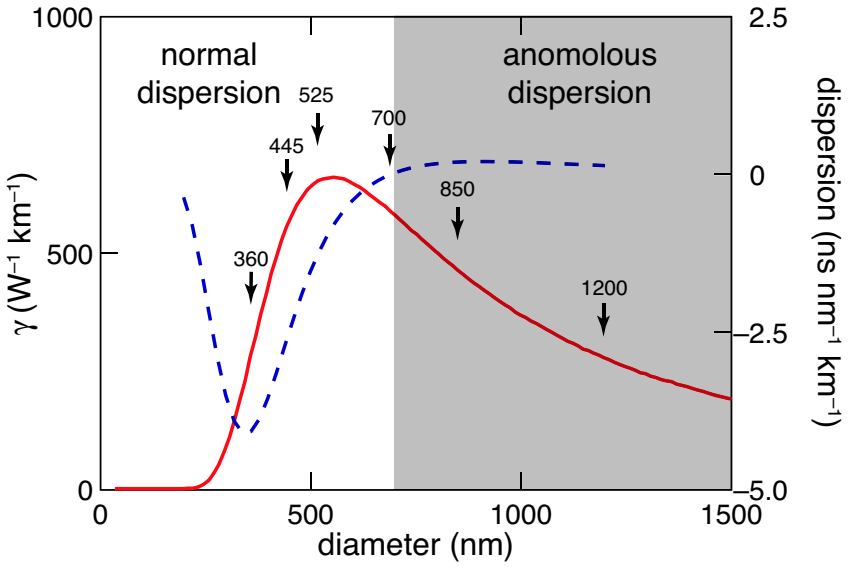

Figure 3.7: Calculated values for the nonlinearity (solid curve) and dispersion coefficient (dashed curve) for an 800-nm wavelength pulse as a function of the fiber diameter. The values for dispersion (D) are calculated for 800 nm from Ref. [30], while the value for the effective nonlinearity of a silica nanowire is calculated using Ref. [62]. The arrows mark the diameters of the fibers from in Figures 3.3 and 3.4.

about 550 nm at a wavelength of 800 nm [62]. Figure 3.7 plots the calculated values for the nonlinearity γ (solid curve) and for the dispersion coefficient D (dashed curve) of an 800-nm wavelength laser pulse. For reference, the black arrows mark the diameters of the fibers presented in Figures 3.3 and 3.4.

Comparing the width of the spectra in Fig. 3.4 with the nonlinearity shown in Figure 3.7, we see that the spectral width grows in agreement with the increase in fiber nonlinearity. When the fiber diameter is below 300 nm, γ is negligible and we observe almost no broadening and the spectrum does not change much when the input pulse energy is doubled. As the fiber diameter increases (300-800 nm), the nonlinearity quickly grows and nonlinear effects manifest themselves. The measured supercontinuum spectrum is broadest for fibers with average diameter between 500–750 nm, which matches the peak in the calculated γ.

As we exceed 800-nm diameter wires, the generated spectrum narrows, in agreement with the reduced value for γ.

We can examine the influence of dispersion by comparing the spectra for the two silica nanowires with average diameters of 445 nm and 700 nm. The nonlinearity γ is approximately the same for both, but the dispersion for 800-nm light is an order of magnitude larger for the 445-nm fiber than it is for the 700-nm diameter fiber (Figure 3.7). The large dispersion explains the narrower spectrum for the 445-nm nanowire than the one for the 700-nm nanowire. Nanowires with diameters outside the range 250 – 500 nm, the laser pulse still suffer from dispersion, but the dispersion length becomes orders of magnitude larger than the interaction length in the nanowire. For nanoscale device fabrication, the ability to select waveguide dimensions that control the nonlinear pulse propagation is a useful method for creating regions of greater and lesser nonlinearity from the same material system.

The relative contributions of dispersion and nonlinearity to the spectral broadening can be determined by comparing the respective length scales with the length of the nanowire. The dispersion length from Eq. (3.6) and the nonlinear length from Eq. (3.8) are shown in Table 3.1 for the pulse width $T_0 = 200$ fs, the wavelength $\lambda = 0.8$ μm, a pulse energy $E_0 = 1$ nJ. In comparison, the average effective length L of the fibers is ∼20 mm.

From Table 3.1 [60], we see that for nanowires with diameters less than 200 nm, $L_D, L_{NL} > L$, and so nonlinear effects do not play a role in the pulse propagation, in agreement with the spectra measured for these diameters. From 200 – 500 nm, $L_{NL} < L \sim L_D$ and nonlinear effects dominate but the dispersion is very large and so the pulse stretches, reducing the intensity before any significant broadening occurs. The dispersion is smaller, thus the dispersion length becomes larger as the diameter increases beyond 500 nm with $L \sim L_{nl} < L_D$ for 500 – 800 nm diameters, indicating that only nonlinear effects

diameter (nm)	D (ps nm^{-1} km^{-1})	γ (W^{-1} km^{-1})	L_D (mm)	L_{NL} (mm)	N
200	-370	2.5	260	400	
400	-3500	413	10	2.4	
600	-425	645	70	1.6	
800	160	500	190	2	9.6
1200	130	278	230	3.6	7.9

Table 3.1: Physical parameters relevant to the propagation of intense 800-nm laser pulses in different diameter fibers. The values for dispersion (D) are calculated for 800 nm according to reference [30], while the value for the effective nonlinearity of a bare silica fiber is calculated according to reference [62]. The dispersion length L_D, the nonlinear length L_{NL} and the soliton number N are calculated according to [28]. The bottom two rows are in the anomalous dispersion region for an 800-nm laser pulse.

contribute significantly in this range.

Silica nanowires with diameters in the range of 700 – 1000 nm have anomalous dispersion for laser pulses centered around 800 nm. When the pulse propagates under anomalous dispersion, the interplay between self-phase modulation and anomalous dispersion make soliton formation possible [28]. This shows how the dispersive properties of a waveguide can limit spectral broadening through a different mechanism. For soliton formation to occur the dimensionless number $N = (L_D/L_{NL})^{1/2}$ must be greater than or equal to 1. As the values in Table 3.1 show, N is significantly larger than one for the bottom two rows, thus we expect higher order solitons to be excited.

In the anomalous dispersion regime, our spectra show less broadening and the appearance of sharp soliton-like features. Higher order solitons are unstable and will break up into fundamental solitons in the presence of perturbations such as third order dispersion [28, 64, 65, 66]. The generation of strong blue-shifted peaks as observed in the spectrum for a 1200-nm nanowire is attributed to higher-order solition self-splitting [67, 68, 69, 66, 70].

The spectra observed for nanowire diameters in the anomalous dispersion regime (diameters ¿ 700 nm) generated with femtosecond laser pulses differ from previous work with fibers of similar diameters with nanosecond pulses [34]. The supercontinuum generated with 532-nm nanosecond pulses propagating in the anomalous dispersion regime has an almost flat 300-nm-wide spectrum [34]. From Figure 3.4e and f, we see that for nanowires with diameters with diameters greater than 700 nm, the spectra generated with femtosecond pulses are not flat and about 200-nm wide. We observe soliton formation at low energies followed by higher-order soliton self-splitting as the energy is increased. Although it is known that at high energies the soliton induced spectra can form a continuum of wavelengths [67, 68, 69, 66, 70], we are not able to achieve such high intensities without damaging the fibers.

Previous work with nanowires in the normal dispersion regime using femtosecond laser pulses claims that dispersion limits the broadening into infrared wavelengths [63]. The reported spectrum generated by a femtosecond laser pulse propagating in 554-μm-diameter tapered PCF had a sharp cutoff in the long wavelength side [63]. We do not observe any sharp cutoff for fibers with a diameter greater than 200 nm, but it is difficult to compare our experiment to previous work with femtosecond laser pulses [63] because it is unclear how to define the effective core size and interaction length of tapered fibers. Nevertheless, we believe that our results show that normal dispersion does not limit the infrared broadening of the supercontinuum spectrum.

We see from Table 3.1 that for nanowires with diameters smaller than 200 nm, the effective length is an order of magnitude smaller than L_D and $L_N L$, and so nonlinear effects do not play a role in the pulse propagation. Although we did not measure any nanowires with average diameters below 200 nm, we observed hardly any broadening in nanowires with minimum diameters below 200 nm. For nanowires with those dimensions, more than 90%

of the light is guided outside the silica core and so the effects of dispersion and nonlinearity are approach that of air. Consequently, a short pulse propagating in these fibers undergoes no spectral dispersion or broadening while still being guided by the fiber, suggesting that fibers with diameters smaller than 200 nm may be ideal for the guiding of intense, short pulses with minimal distortion.

3.6 Conclusions

We explored the nonlinear wave propagation along silica nanowires and calculated the effective nonlinearity taking into account the large evanescent field contribution to the waveguide mode. We experimentally confirmed the diameter dependence of the nonlinearity by using supercontinuum generation as a probe for characterizing the nonlinear optical properties of silica nanowires. The observed supercontinuum generation results from an interplay between the diameter-dependent nonlinearity and the dispersion of the fiber. The maximum broadening occurs for nanowires with diameters around 500 nm. Nanowires with diameters less than 200 nm appear to have negligible dispersion and nonlinearity making these waveguides useful for propagation of intense, short pulses with minimal distortion. The reduction of the interaction length to $\sim$20 mm and the low energy thresholds, supercontinuum generation in tapered fibers is a viable solution for coherent white-light source in nanophotonics.

3.7 Outlook

The investigation into the nonlinearity of the fiber through supercontinuum generation indicates that 500-nm diameter wires have an enhanced nonlinear parameter. Using intense laser propagation, we can take advantage of this enhancement in order to create

nonlinear optical devices. In Chapter 2, we showed the fabrication of a variety of linear optical devices including a 2×2 coupler and a micro-ring resonator. The short interaction length required for substantial nonlinear effects to occur implies that we can create devices whose operation relies on the diameter dependent behavior of the nonlinearity. The nonlinear propagation of light in nanoscale waveguides creates opportunities for nanoscale optical switching and optical logic and we will investigate one such device based on the Sagnac interferometer geometry in Chapter 4.

It is also useful to explore the possibility of using other material systems. The experiments performed in this chapter used nanowires drawn from optical fiber-quality silica, which is purified to produce the lowest losses and nonlinearity in order to maintain signal integrity over long distances. Nanowires fabricated from most other materials have a higher refractive index and will exhibit a higher nonlinearity, and may have tolerable losses over the small interaction lengths required for nonlinear device operation. We will investigate the use of ZnO nanowires as a candidate for these devices in Chapters 5 and 6.

Chapter 4

Nonlinear Sagnac interferometer using silica nanowires

In the previous chapter, we demonstrated that silica nanowires can be used as a model system for studying nonlinear optics at the nanoscale due to the enhanced nonlinear parameter, γ, and the nanowire diameter dependence of the waveguide dispersion. The top-down taper-drawing fabrication method allows for large interaction lengths (tens of millimeters) and the coupling of light from macroscopic sources to the nanoscale. The results from Chapter 3 show an optimal nanowire diameter for enhancing nonlinear effects in silica nanowires. We now consider experimental approaches that combine our understanding of the nonlinearity with our expertise in assembling photonic devices using silica nanowires.

In this chapter, we show the first demonstration of a nonlinear Sagnac interferometer using silica nanowires. This device is a basic component in the architecture for more complex optical devices that perform channel demultiplexing [72], pulse shaping [73], optical logic operations [74], and passive mode-locking for fiber lasers [75, 76]. The motivation for using silica nanowires to construct a Sagnac interferometer is to reduce the dimensions

enough for integration in microphotonic circuits.

We demonstrate all-optical modulation of ultrashort laser pulses (800 nm, 1 ps) with pulse energies on order of one nanoJoule. Laser pulses are injected into a Sagnac interferometer that is fabricated from a single silica nanowire with minimum diameter of 550 nm. The transmitted power through the Sagnac interferometer displays a nonlinear dependence on the input power. The relatively low pulse energy required to produce nonlinear effects in subwavelength silica nanowires is promising for optical switching and logic in integrated nonlinear microphotonics.

4.1 Background

Optical interferometry is a powerful tool in physics and astronomy with such wide-ranging applications as dispelling the existence of *aether* [77], detecting gravitational waves [78], sensing biological and chemical agents [79], and mimicking the iridescence of butterfly wings [80, 81]. There are many different types of interferometers; for example, perhaps the most familiar is the Michelson-Morley interferometer, shown in Figure 4.1, which has two independent paths that recombine to create an interference pattern at the detector. Small changes in the length of one of the paths yield a phase difference that causes a change in the interference pattern. Detection of the interference pattern reveals small phase changes and enables precise measurements.

The Sagnac interferometer configuration, shown in Figure 4.1, differs from the Michelson-Morley configuration in that counterpropagating beams that share the same path [82]. Even though this arrangement requires the two paths to have an identical length, a phase difference can occur when the system experiences rotation. The finite speed of light means that a rotation will shorten the path for one direction of propagation and lengthen

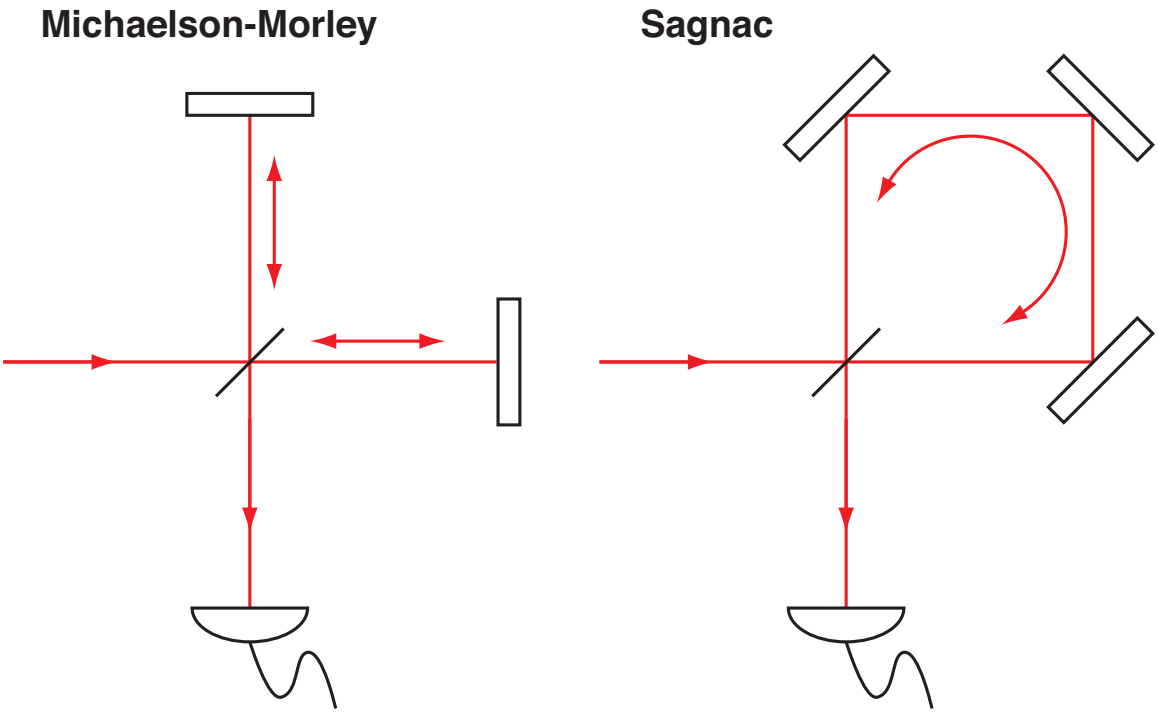

Figure 4.1: Diagram of a Michelson-Morley and a Sagnac interferometer. The Michelson-Morley configuration has two independent propagation paths, whereas the Sagnac configuration has a single shared path of counterpropagating beams.

the path for the other direction, which Georges Sagnac was able to experimentally observe and explain in 1913 [83, 84].

The ability of the Sagnac interferometer to detect rotations is useful for such application as a gyroscope. Early Sagnac interferometer-based gyroscopes measured the angular velocity of the Earth [85], and were envisioned to be useful for ship navigation [86]. Modern gyroscopes in inertial guidance systems provide 3D angular information to aircraft and satellites using ring lasers [87, 88, 89] as well as fiber-optic gyroscopes [90, 91].

The geometry of the Sagnac interferometer is easily reproduced using optical fibers by replacing the beam splitter with a 2x2 fiber coupler, as shown in Figure 4.2. The optical fiber can be coiled up to produce large path lengths in a relatively small packaging volume,

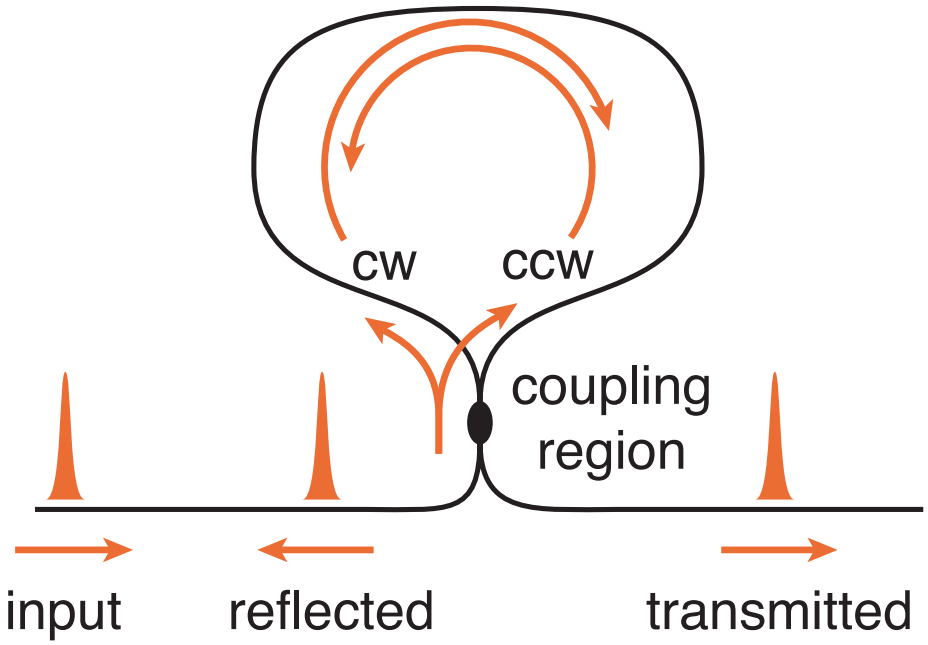

Figure 4.2: Diagram of a fiber Sagnac interferometer showing the clockwise and counter-clockwise paths and the directions of the input, reflected and transmitted light. The coupling region in our experiment results from evanescent coupling between touching silica nanowires.

which allows for a more sensitive measurement for the gyroscopic application mentioned above.

Using optical fiber provides another method for inducing a phase difference between the clockwise and counter-clockwise propagating beams: the optical Kerr effect. The intensity dependent index of refraction contributes to an accumulated nonlinear phase around the loop that can be different for the two paths, which will be described below.

In Chapter 3, we showed that the tight confinement of the mode in silica nanowires enhances the nonlinear parameter, γ, from Eq. (3.12), generating supercontinuum when femtosecond-laser pulses are launched into these nanowires [60]. In Chapter 2, we demon-

strated that evanescent coupling between two silica nanowires can be used to fabricate 3-dB couplers [46]. The enhanced nonlinearity and evanescent coupling properties suggest that a nonlinear Sagnac interferometer can be fabricated from silica nanowires. In such a configuration, the coupling region shown in Figure 4.2 results from touching two silica nanowires.

We proceed to describe the equations governing the nonlinear Sagnac interferometer [28]. In Section 2.1, we described the electric field inside a fiber by Eq. 2.2, which has a fast oscillation term $e^{-i\beta(\omega)z}$ that we will now write as $e^{-i\phi}$ where the phase is defined

$$\phi = \beta(\omega)z \equiv n(\omega)\frac{\omega}{c}z. \tag{4.1}$$

We expand the index of refraction to include intensity-dependent coefficient n_2

$$n = n_0 + n_2 I = n_0 + n_2\frac{P_0}{A_{eff}}. \tag{4.2}$$

where P_0 is the peak input power and A_{eff} is the effective area. The nonlinear index coefficient is related to the third-order susceptibility $n_2 = \frac{3}{8n}\mathrm{Re}[\chi^{(3)}_{xxxx}]$ [11], which is also related to the nonlinear parameter γ in Eq. (3.3). Rewriting the phase in Eq. (4.1) with those substitutions

$$\phi = \frac{n_0\omega}{c}z + \gamma P_0 z \equiv \beta_0 z + \gamma P_0 z. \tag{4.3}$$

where the first term is the linear phase, ϕ_L, we found in Section 2.1, and the second term is the nonlinear phase, ϕ_{NL}.

To understand how the nonlinear phase will impact the operation of a nonlinear Sagnac interferometer, we need to include the coupling region. We will treat this region as a linear 2x2 coupler similar to the device we showed in Chaper 2. Eqs. (2.10) and (2.11)

give the resulting electric fields in the output ports. We can define a coupling parameter that absorbs all the details of the coupling region

$$\rho = \cos^2(\kappa l_c) \tag{4.4}$$

where l_c is the length of the coupler. This substitution, and the trigonometric identity $\cos^2(x) + \sin^2(x) = 1$, allows us to rewrite Eqs. (2.10) and (2.11) for the case of our Sagnac interferometer

$$A_{cw} = \sqrt{\rho} A_0 \tag{4.5}$$

$$A_{ccw} = i\sqrt{1-\rho} A_0, \tag{4.6}$$

where A_0 is the slowly varying longitudinal function that describes the input electric field, and A_{cw} and A_{ccw} describe the clockwise and counter-clockwise fields shown in Figure 4.2. The fraction of the field that "hops" from one fiber to the other acquires a $\pi/2$ phase shift, indicated by i, that is completely analogous to the phase shift induced by reflecting off or passing through a half-silvered mirror in the Sagnac geometry shown in Figure 4.1.

The clockwise and counter-clockwise fields both accumulate the nonlinear phase given by Eq. (4.3) as they propagate around the loop. These phases can be different because the peak power of the counter-propagating pulses depends on the coupling parameter ρ. The pulses then recombine at the coupler interferometrically resulting in the transmitted and reflected pulses shown in Figure 4.2. To calculate the transmitted field, we add together the components from the clockwise and counter-clockwise fields as they go through the coupler again

$$\begin{aligned} A_{trans} =& \rho A_0 e^{i\phi_{cw}} && \text{(from the cw path)} \\ & - (1-\rho) A_0 e^{i\phi_{ccw}} && \text{(from the ccw path)} \end{aligned} \tag{4.7}$$

where ϕ_{cw} and ϕ_{ccw} are the respective accumulated phases along the length of the loop L. Substituting in the phase from Eq. (4.3), and squaring the electric field gives

$$\frac{|A_{trans}|^2}{|A_0|^2} = 1 - 2\rho(1-\rho)(1+\cos[(1-2\rho)\gamma P_0 L]). \tag{4.8}$$

Equation (4.8), also referred to as the transmittivity, reveals how the linear phase cancels perfectly, and gives a condition under which a Sagnac interferometer can act as a fiber-loop mirror [28]. In particular, using a 3-dB coupler in the coupling region of Figure 4.2, corresponding to a value $\rho = 0.5$, will yield $|A_{trans}|^2/|A_0|^2 = 0$. We can physically interpret this result as the forward and counter-propagating fields canceling out exactly at the output port, resulting in a perfect reflection of the incoming wave back along the input port. Using a fiber-based Sagnac interferometer in this mode of operation has applications in the fabrication of fiber lasers.

When the coupler does not equally split the incoming signal, *i.e.* $\rho \neq 0.5$, the reflection and transmission become power-dependent and vary sinusoidally with $(1-2\rho)\gamma P_0 L$. Thus, when the cosine term in Eq. 4.8 undergoes a full oscillation, or more precisely [28]

$$(1-2\rho)\gamma P_0 L = (2m-1)\pi \tag{4.9}$$

where m is and integer, we can achieve optical switching. Figure 4.3 shows the calculated transmitted power as a function of input power for continuous-wave laser light at two values of coupling parameter ρ near 0.5 using the standard optical fiber value of $\gamma = 10$ $\mathrm{W^{-1}km^{-1}}$ and a fiber length $L = 100$ m. The split signals accumulate different amounts of nonlinear phase (Eq. (4.3)) while propagating around the loop. This physical behavior has been demonstrated for switching and logic operations [74, 92, 93]. For example, the interferometer can be designed such that when two signals are fed into the input port, a transmitted signal at the output port is seen only when both signals are synchronous. The

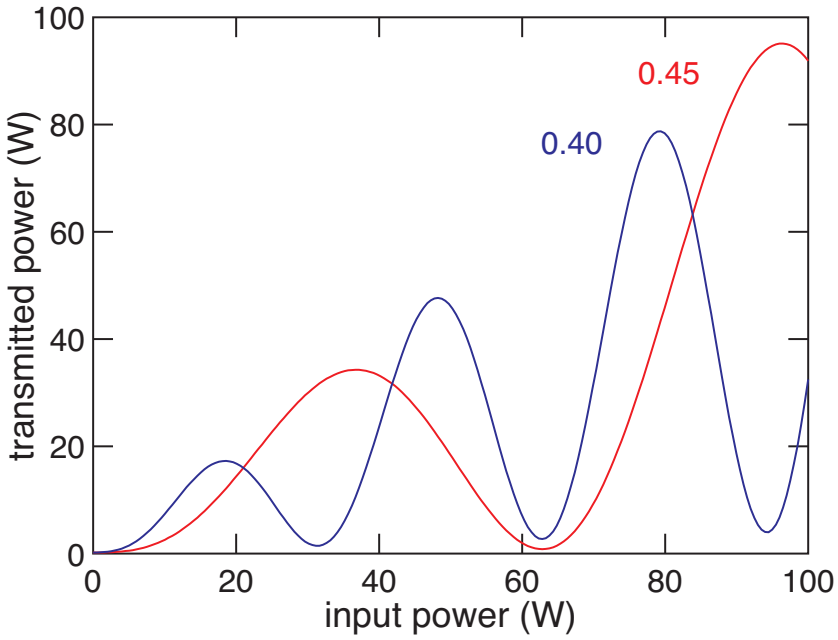

Figure 4.3: Transmitted power as a function of input power for a nonlinear Sagnac interferometer. The transmission exhibits sinusoidal oscillations with increasing input power for coupling parameters ρ of 0.40 and 0.45. After Ref. [28].

nonlinear effect of the Sagnac interferometer allows the combined intensity of two signals to be high enough to cause switching, but one signal alone is reflected [94].

4.2 Experimental Setup

To construct a nonlinear Sagnac interferometer, we fabricate silica nanowires by the conventional taper-drawing method described in Section 2.2, which are connected via taper on both ends to single-mode standard optical fiber for convenient input and measurement. Our results in Section 3.4, studying the supercontinuum generated by femtosecond laser pulses in silica nanowires of various diameters, show that the largest effective nonlinearity is achieved for nanowires with diameters in the range of 500 to 800 nm. Using a

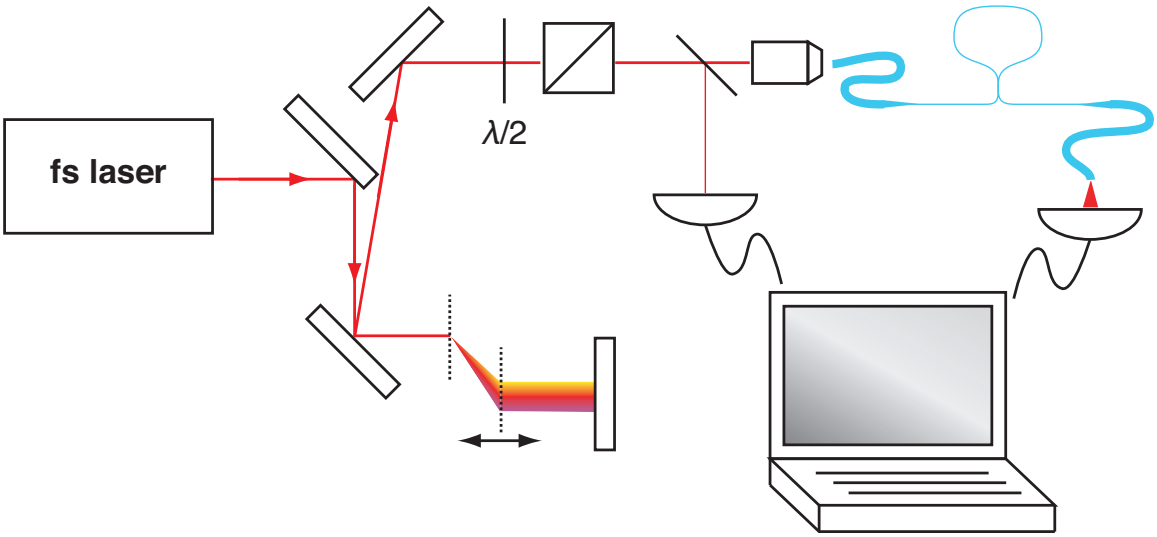

Figure 4.4: Schematic diagram of the experimental setup used to measure the transmitted power as a function of input power. The femtosecond laser pulses pass through a transmission grating pair and a variable attenuator before coupling into the optical fiber with a microscope objective.

variety of techniques involving micro-manipulators, air currents, and foldable mounts, we assemble the silica nanowires into the geometry shown in Figure 4.2, either free-standing or on a low-loss aerogel substrate. The evanescent coupling in the overlap region of the incoming and outgoing fiber, similar to Figure 2.8b, can be tuned similarly to our variable couplers [46] shown in Figure 2.15.

To characterize the linear and nonlinear response of the silica nanowire Sagnac interferometer, we couple pulses from a femtosecond laser oscillator (800 nm; 60 fs; 11MHz; 80 nJ) [95] through a transmission grating pair and a variable attenuator into standard optical fiber using a 10x microscope objective, as shown in Figure 4.4. Pulses couple to the nanowire via tapered fiber, then pass through the Sagnac loop, couple via a second taper to standard fiber and are collected by a photodiode or spectrometer. The Sagnac loop is situated over an inverted microscope for positioning and imaging the *in situ* nanowires. Following the transmission measurements, we transfer nanowires to a silicon substrate for

imaging using the SEM.

The transmission grating pair is used to pre-compensate for the length of standard optical fiber on the input side of the Sagnac loop [96]. The gratings have specifications of 20x20 mm, 600 lines/mm, blaze angle of 13.8 degrees, and a transmission efficiency of about 90% [97]. We align the first grating by finding the angle where the 0 degree transmission is minimum; this is when most of the power is in the first order reflection. The second grating is on a translation stage for an adjustable grating spacing. After optimizing the transmission efficiency, the beam hits a corner mirror pair, which sends the beam back along exactly the same path below the incoming beam, where it reflects off of a short, square pickoff mirror. We measure an efficiency through the grating pair of 0.64, which is very close to the maximum efficiency for passing through the gratings four times ($0.9^4 = 0.656$).

In order to control the input power into the Sagnac interferometer, we send the pre-compensated pulse through a variable attenuator, which consists of a half-wave plate, a polarizing beam-splitter cube, and an etalon. The half-wave plate is mounted on a computer-controlled rotation stage with an angular resolution of $< 0.01°$. We use the etalon to "pick-off" a few percent of the light, which is detected by a photodiode and used for calibration of the input power.

4.3 Results

Figure 4.5 shows the experimentally measured transmission through a silica nanowire Sagnac interferometer. We observe a change from the linear behavior of transmission in Figure 4.5a, into a distinct nonlinear transmission in Figure 4.5b. We acquired data over multiple sweeps through the same range of average input power. While all sweeps maintain the same the qualitative shape, some shifts in the measured transmission occur due to

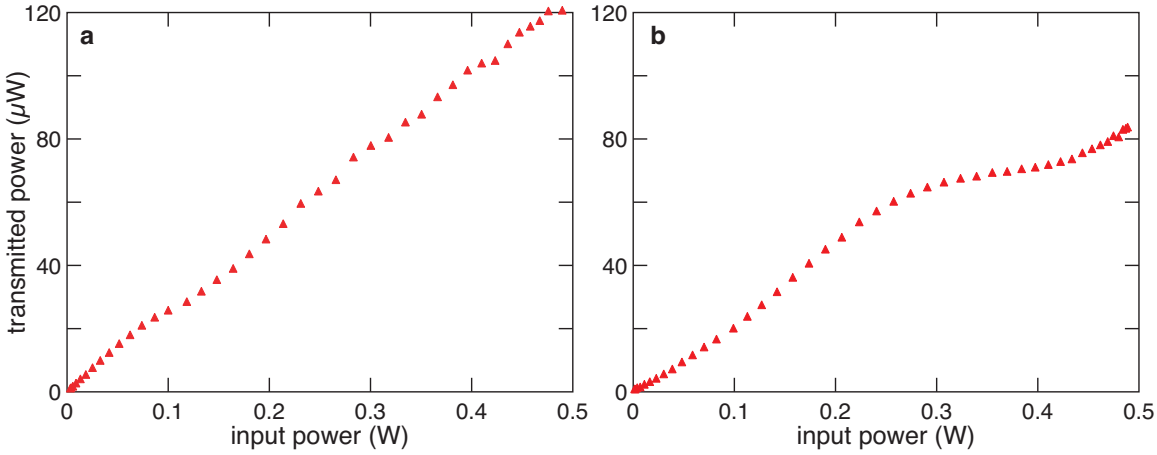

Figure 4.5: Experimentally measured transmission as a function of the input power of the Sagnac loop shown in Figure 4.7c. (a) Transmission for a "quasi-cw" pulse. (b) Transmission for pulse with the experimentally determined optimal pre-compensation for 20 cm of single mode optical fiber.

motion of the nanowire loop region over the time the measurements are taken. Based on autocorrelation traces of pulses traveling through 20 cm of single mode fiber, the grating pair separation for the data in Figure 4.5a corresponds to a pulse width of > 1 ps. The grating separation for the data in Figure 4.5b gave an autocorrelator trace of 720 fs, which corresponds to a 510 fs pulse width.

Figure 4.6 shows the spectra at two powers for the Sagnac interferometer with optimal pre-compensation used to collect the data in Figure 4.5b. The low power transmission yields a spectrum very similar to the input laser spectrum, whereas the high power transmission generates a broadened spectrum of about 15 nm in bandwidth. The observed broadening of the spectra is consistent with the operation of a nonlinear switch by self-phase modulation, which requires new frequencies to be generated to create the phase difference.

Figure 4.7 gives the details of the silica nanowire that we measured to acquire the data in Figure 4.5. By collecting a series of nanowire diameter measurements using the SEM, an example of which is shown in Figure 4.7d, we obtain the fiber diameter profile

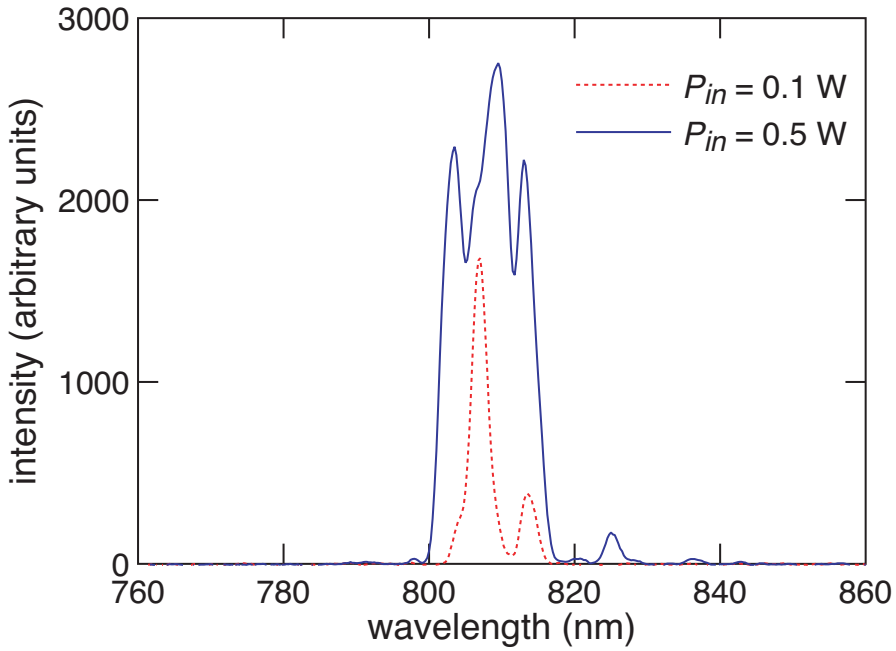

Figure 4.6: The transmitted spectra for the silica nanowire Sagnac interferometer in Figure 4.5. The spectrum broadens from the input laser line at low powers (dotted line) to about 15 nm at high powers (solid line).

shown in Figure 4.7a and b. Figure 4.7c is a microscope image of the assembled Sagnac interferometer, which provides an estimate for the length of the loop of approximately 500 μm.

The photograph in Figure 4.8 shows a different Sagnac interferometer assembled from a silica nanowire and supported on a mesoporous silica substrate. Using an amplified femtosecond pulse laser system, we can increase the input power up to the range for supercontinuum generation that we found in Chapter 3. We observe broadband scattered light in the Sagnac loop and along the output fiber.

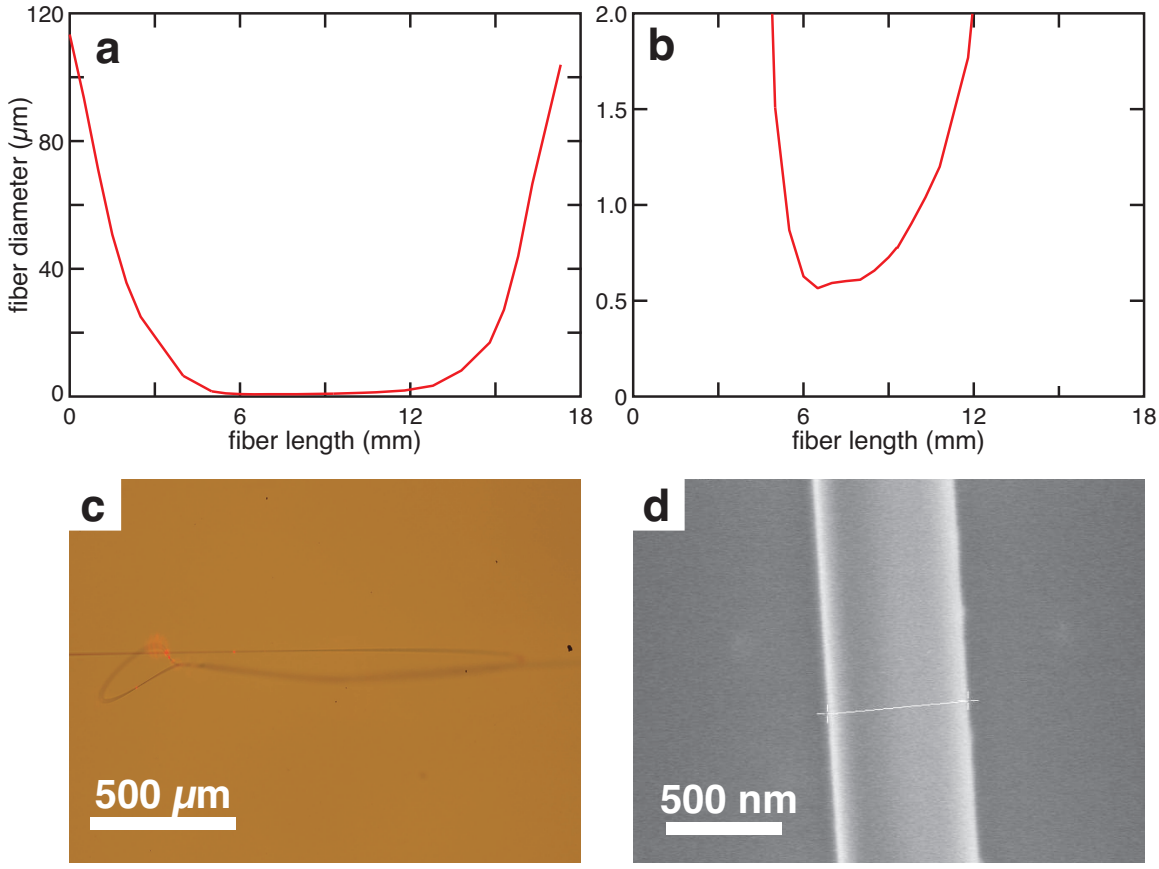

Figure 4.7: Details of the silica nanowire used to acquire the data in Figure 4.5. (a) Nanowire diameter profile as measured by SEM, with (b) finer scale on the sub-2 μm diameter region. (c) Microscope image of the free-standing Sagnac loop assembled with this nanowire, here shown with continuous-wave laser input. (d) Sample SEM measurement of the diameter of the silica nanowire.

4.4 Discussion

Our motivation for building a Sagnac interferometer using silica nanowires is to learn about the fundamental waveguiding of light at the nanoscale and to miniaturize the "footprint" required for optical switching, allowing for integration into microphotonic devices. The first experimental demonstration of all-optical switching using a nonlinear Sagnac interferometer involved a 25-meter loop of germanium-doped silica telecom fiber with a coupling parameter $\rho = 0.38$ [98]. The experiment, based on the design proposed in Ref. [74],

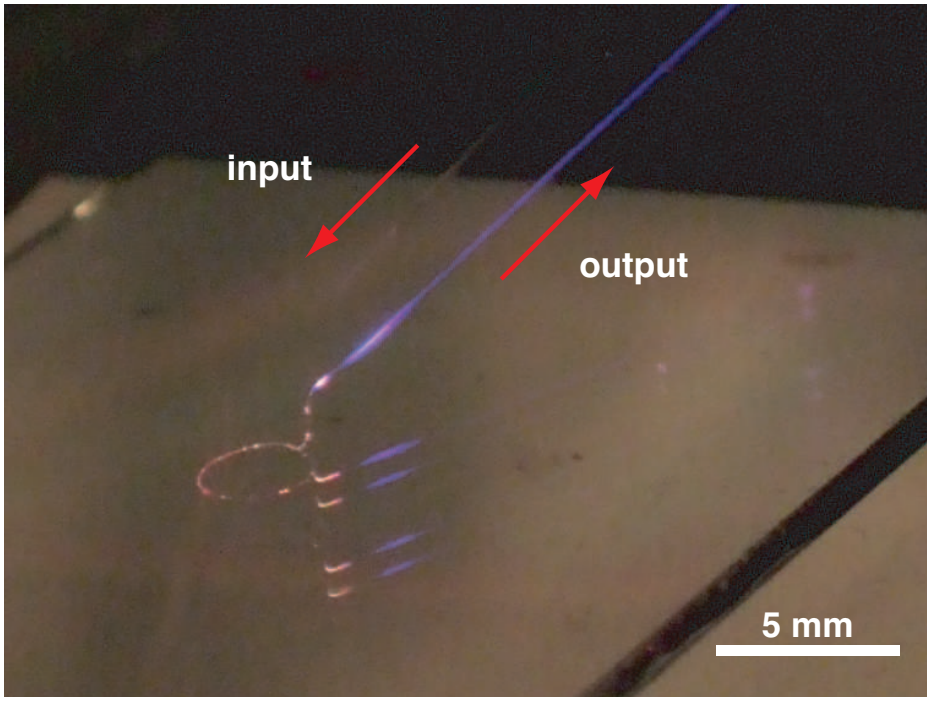

Figure 4.8: Generation of supercontinuum light in a silica nanowire Sagnac loop on a mesoporous silica substrate. The photograph also shows reflections of the input and output fibers, as well as the loop itself, from the glass slide below the mesoporous silica layer.

measured an increase in the transmittivity (Eq. (4.8)) to just over 60% for 850 ns pulses with peak power of about 30 W, and similar results for pulses of 180 ps in duration. The transmitted pulse shows narrowing since the switching occurs for the central, higher power part of the pulse [98]; this can be useful for applications in pulse shaping and cleanup [28]. Subsequent work showed that pulses can be switched entirely by using soliton pulses, which acquire a uniform nonlinear phase across the pulse [99]. Soliton switching has applications in demultiplexing [100] and other complex optical processing. Recent nonlinear Sagnac interferometers using semiconductor optical amplifiers (SOA) [101] can achieve switching with significantly lower peak powers and a shorter interaction length due to the gain in the SOA region.

In order to compare our silica nanowire Sagnac interferometer to previous results,

we must examine in detail the data in Figure 4.5, which exhibits a nonlinear transmission. Even though we do not observe the deep modulation that the calculated transmission in Figure 4.3 shows, we see a clear departure from linear transmission. To understand the curvature seen in Figure 4.5b, we fit our data to Eq. (4.8), as shown in Figure 4.9. We calculate the peak power from the average input power using

$$P_0 = T_0^{-1}\nu^{-1}P_{ave}, \tag{4.10}$$

where T_0 is the pulse width and ν is the repetition rate of the laser (11 MHz). We perform the fit with two free parameters, ρ and the combined term $\gamma L T_0^{-1}\nu^{-1}$, and an overall scaling factor.

The fit displays excellent agreement with the data and provides a value for the coupling parameter of $\rho = 0.08$. The motion of the free-standing Sagnac loop due to air currents is responsible for the uncertainty of about 10% across different power sweeps. Assuming values of $L = 0.5$ mm and $\gamma = 0.5$ $\mathrm{W^{-1}km^{-1}}$, the other free parameter of the fit gives a nonsensical value for the pulse width. The failure to acquire a meaningful value for the pulse width indicates that we have not accounted for a loss mechanism between the Sagnac loop and the measured output power. If we assume a pulse width of $T_0 = 1$ ps, which is reasonable based on autocorrelation traces, the fit parameter implies a loss of about 5×10^{-4}, which may occur in the coupling region, output taper region, or in the collection. Future experiments will need to address this non-neglible loss in order to make the terms in the data fit more precise. Even with that limitation, the fit gives an upper limit for the pulse energy required for a π phase shift of 2 nJ, which compares well with values from previous work using silica optical fiber (about 5 nJ [98]), and using SOA (about 1 nJ [102]). Ultimately, the fit shows that our silica nanowire Sagnac inteferometer is capable of modulating light by light with relatively low energies over a small length scale.

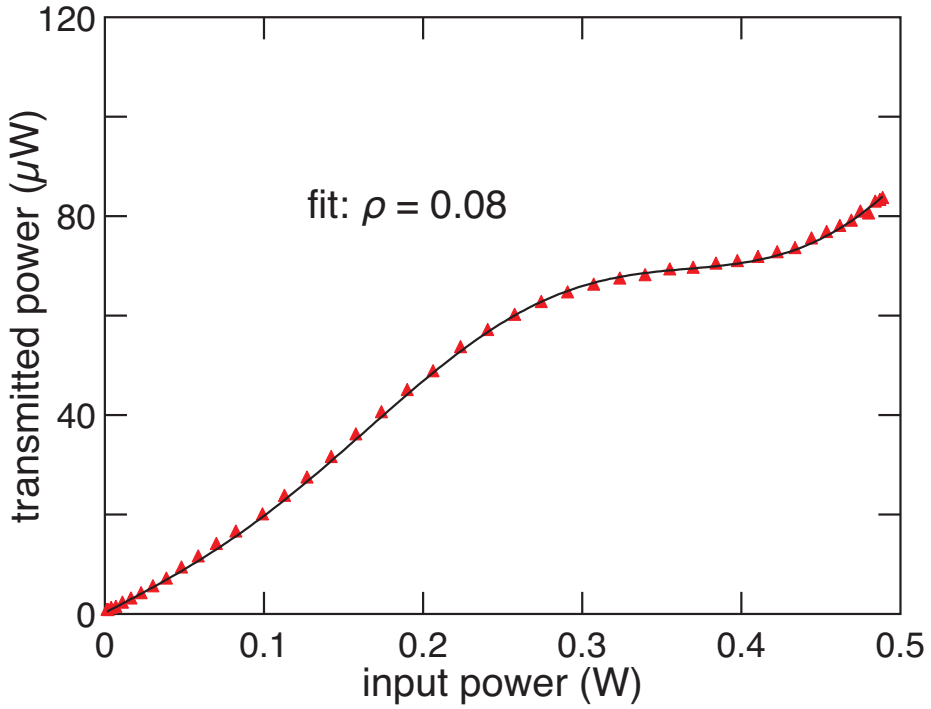

Figure 4.9: The fit of the measured transmission from Figure 4.5 to Eq. (4.8), which yields a coupling parameter $\rho = 0.08$.

We do not see the deep modulations in Figure 4.3 because of the relatively low value of the coupling parameter. As the coupling parameter approaches 0.5, the extinction of the transmission becomes stronger and the oscillation period increases (because the term $(1 - 2\rho)$ multiplies by the nonlinear phase in Eq. (4.8)). As a consequence, to measure the deep modulations in transmission due to a nonlinear Sagnac interferometer with a coupling parameter near 0.5, we need to reach larger values of the term $\gamma P_0 L$.

We can increase γ from Eq. (**??**) by increasing the nonlinear coefficient n_2, or by decreasing the effective A_{eff}. We can satisfy both by selecting a different material system with a higher refractive index n_0. In general, materials with higher refractive indices also have higher nonlinear coefficients [103]. In addition, the minimum mode field diameter scales with the wavelength of light inside a material $\lambda = \lambda_0/n_0$, where λ_0 is the vacuum

wavelength [30]. Thus, the higher the refractive index, the tighter the potential mode confinement, resulting in a smaller A_{eff}. Chapters 5 and 6 will explore the possibility of using the ZnO material system to take advantage of the higher index and nonlinearity that contribute to larger values of γ.

Increasing the other two parts of the nonlinear phase, P_0 and L, is more straightforward. The length of the Sagnac loop L can be made longer by multiple coiling, however, experimentally, the fabrication process creates an upper limit of about 1 cm. The peak power P_0, on the other hand, given in Eq. (4.10), can be increased much more readily. We assume that our pulse width T_0 is on the order of 1 ps. Presumably, we should be able to re-compress the pulse close to 100 fs, but in the region where the dispersion is close to zero (around 700 nm in diameter as shown in Figure 3.7), we may also need to compensate for third-order dispersion. In addition to decreasing the pulse width, we can increase the pulse energy by as much as a factor of 10^4 by repeating these experiments using an amplified femtosecond laser system. Lastly, we can improve the loss in the tapered region of the silica fiber so that more of the power coupled into the standard optical fiber is coupled into the nanowire Sagnac loop.

The photograph in Figure 4.8 shows that we can reproduce the supercontinuum generation that we observed in Chapter 3 by using an amplified femtosecond laser source. Experimentally testing over 50 fibers revealed no switching behavior in Sagnac loops that were generating supercontinuum light. It is likely that when the spectrum broadens beyond a certain range, the dispersion, which we can see from Figure 2.3, chirps and distorts the pulse, effectively "washing out" the interference effects. Measuring the broadening in the output spectrum of a silica nanowire loop at increased input powers can be used to characterize the nanowire and may have other applications.

4.5 Conclusions

In this chapter, we showed the first demonstration of a nonlinear Sagnac interferometer fabricated with silica nanowires. We measured the transmitted power as a function of input power and observed a distinct nonlinear response that indicates light-by-light modulation. We fit the nonlinear transmission to theoretical predictions to obtain physically relevant parameters. The fit displays excellent agreement with the data and gives a value for the coupling parameter of $\rho = 0.08$. The relatively low value of the coupling parameter accounts for the lack of deep modulations in transmission. The fit also gives a value for the phase of the oscillation that implies an unknown loss mechanism between the power in the Sagnac loop and the measured output power. Using estimates that were measured by other means for the nonlinear parameter, interaction length, and pulse duration, we calculate and upper limit of 2 nJ for the pulse energy required to achieve a π phase shift. We also increased the input power in the Sagnac loop using an amplified femtosecond laser system and observed supercontinuum generation but no switching behavior.

Our motivation for building a Sagnac interferometer using silica nanowires is to understand the fundamental properties of nonlinear optics at the nanoscale as well as to explore the practical applications that come from the miniaturization of photonic devices that allow for their integration. Our Sagnac loop achieves substantial nonlinear effects in less than a millimeter with relatively low pulse energies (fewer than a couple nanojoules). Future experiments will need to address the non-neglible loss in order to better understand the contribution of such parameters as the nonlinear parameter and the pulse duration.

For application as a nonlinear switch, the desirable deep modulation in transmitted power requires larger coupling and the ability to reach higher values of the nonlinear phase ($\gamma P_0 L$). We can increase γ by choosing materials with higher refractive indices and higher

nolinearity. In particular, we will examine the use of ZnO nanowires in the next two chapters as an example of a semiconductor material system for potential integration of nonlinear photonic devices.

4.6 Limitations and Outlook

As we have shown in Chapters 2 and 3, silica nanowires are a model system for studying nonlinear optics at the nanoscale because of their low loss and tight mode confinement. We take advantage of our top-down taper-drawn fabrication of nanowires to rapidly prototype microphotonic devices, but some difficulties and limitations exist in considering the future implementation of these devices. In particular, the narrow window of nanowire diameters, lower limits on the interaction lengths and input powers, and complicated procedures for micro-manipulation make repeatability and comparison difficult. We also often find that the Van der Waals attraction of the silica nanowires causes free-standing Sagnac loops to create complex tangles that result in the complete scattering of input light. This difficulty appeals to the use of mesoporous substrates, which we also employed. However, while assembling the Sagnac loop, we frequently needed to drag the nanowire repeatedly across the mesoporous surface, which would often cause the accumulation of nano-particles that we observed with the SEM. These particles effectively degrade the surface quality of the nanowires and can contribute to scattering.

Another limitation comes from the choice of silica as a nonlinear material in the Sagnac loop. The "preform" for a silica nanowire is a standard telecom optical fiber, which is highly purified to prevent absorption and loss and to reduce the nonlinearity that would destroy the integrity of digital information being transmitted over long distances. As we discussed, complete nonlinear switching in a Sagnac interferometer occurs for near 3-dB

coupling and requires a larger peak power in the loop for silica. Since optical fiber quality silica has one of the lowest material nonlinearities, nanowires of almost all other materials will have higher nonlinearity; this can increase the accumulated nonlinear phase without requiring an increase in the peak power. The ZnO nanowires we study in the next two chapters have a material nonlinearity of about 50 times that of silica [103].

Previous experiments accounted for depolarization of the light while propagating around the Sagnac loop [98, 99]. Even though the propagation lengths are substantially smaller in our experiment (as a result of using silica nanowires to tightly confine the transverse mode), the evanescent field is large enough that surface contaminants, microbends, and tensions may lead to unknown depolarization effects. In general, fiber couplers contribute to depolarization, and evanescent field coupling between two nanowires is likely polarization dependent as well. This implies that future implementations of our device will need to include polarization modeling in the design and operation.

The limitations described above do not present any fundamental barriers to the miniaturization of a nonlinear Sagnac interferometer for integration in microphotonic devices. The experimental difficulties can be overcome by improving the micro-manipulation procedure and taking advantage of other materials and standardized fabrication techniques. If we look ahead at the potential use of these devices, we can envision not only all-optical switching but applications in optical logic as well.

Using the knowledge obtained by manufacturing and characterizing nonlinear Sagnac interferometers, we have a positive outlook for miniaturized, microscale structures made from silica (and potentially other materials), that can act as all-optical logic gates by employing ultrashort laser pulses as input signals. Previous all-optical logic gates based on this principle have been demonstrated [74, 93], but in general require hundreds of meters of custom-made optical fiber and high powers to achieve the desired functionality. Recent

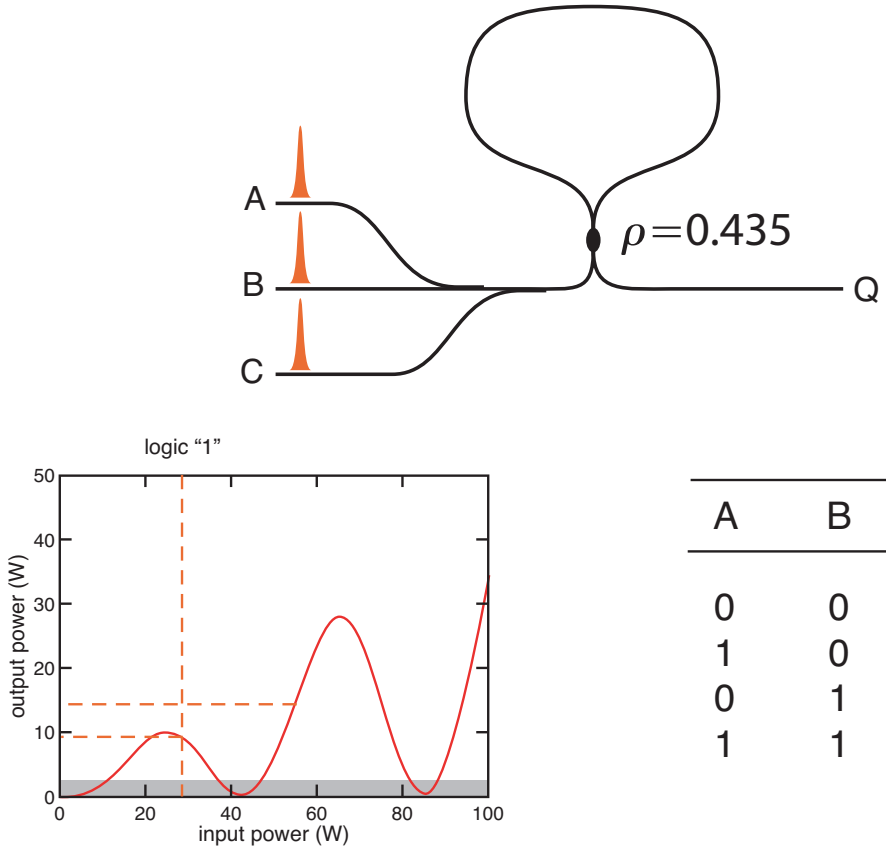

A	B	Q
0	0	1
1	0	1
0	1	1
1	1	0

Figure 4.10: Schematic diagram of an optical NAND gate using a nonlinear Sagnac interferometer. Using input ports A and B and control port C, a Sagnac loop with a specifically chosen coupling gives a transmission that can be used for optical logic. An input pulse energy can be chosen as a logical "1" such that combinations of inputs give logical outputs at port Q (logical "0" in gray on the plot) yielding a truth table representing a NAND gate.

experiments using planar waveguides and an SOA as the nonlinear element have reduced the device size to a few mm^2 [92].

Basic logic operations such as AND, XOR, and inversion have already been shown in the Sagnac interferometer configuration using standard-size optical fiber [92]. Figure 4.10 details the configuration of a Sagnac interferometer that displays transmission behavior corresponding to NAND gate operation, where the powers shown are arbitrary. The NAND

gate, in particular, is a universal gate from which all other operations can be performed. We demonstrated the assembly of a similar structure using silica nanowires, but the assembly in Figure 4.10 could be a combination of materials, including active materials that may be pumped to provide gain. Ultrashort pulses from a Ti:sapphire laser or microchip-pulsed laser can be used as input signals at ports A and B and control port C leading to a nonlinear Sagnac interferometer. The phase shift induced by the combination of pulses at the input provides the mechanism for the switching and logic. More precisely, the power of the input signal is chosen to yield a logical "1", and coupling parameter is chosen so that multiple input pulses yield either logical "0" or logical "1" at port Q, as given in the truth table.

In conclusion, we foresee a flexible optical logic gate for processing ultrafast optical signals that can reduce the required footprint to less than 100×100 μm^2. Furthermore, the use of subwavelength-diameter silica wires enables rapid assembly and quick geometry modification, as well as provides the important connection from macroscopic light sources to nanoscopic waveguides and devices. Employing nonlinear optics at the nanoscale creates an excellent platform upon which highly-integrated optical circuits can be built.

Chapter 5

Waveguiding in ZnO nanowires

As shown in Section 2.1 discussing silica nanowires, a large index contrast provides for tight confinement of the mode, which is useful for enhancing the nonlinear parameter, γ from Eq. (3.3), and allowing for the fabrication of nanoscale nonlinear photonic devices. Semiconductor material systems such as silicon, indium phosphide, and zinc oxide (ZnO), in general, have higher refractive indices than silica [103], allowing for tighter mode confinement. Semiconductor materials employed in photonic devices can act as passive waveguides, and can also exhibit active optical properties that depend on the free-carrier concentration. This chapter will focus exclusively on the passive waveguiding properties of ZnO nanowires, whereas chapter 6 will discuss the transmission characteristics and heating that result from femtosecond-pulse excitation of ZnO nanowires.

We use tapered silica fibers and nanowires to inject laser light and broadband sources into ZnO nanowires with diameters around 250 nm to study their waveguiding properties. We find that high-order waveguide modes are frequently excited and carry significant intensity at the wire surface. Numerical simulations reproduce the experimental observations and indicate a coupling efficiency for visible light between silica and ZnO

nanowires of around 50% for a variety of coupling angles. Experimentally we find an emission angle from the ZnO nanowires of about 90°, in agreement with the simulations.

In this chapter, we show that the combination of silica nanowires, which are fabricated in a top-down approach, and ZnO nanowires, obtained from a bottom-up growth process, allows a detailed experimental investigation of the passive waveguiding properties of the semiconductor nanowires. By carrying out numerical finite-difference time-domain simulations we find that it is possible to achieve a high coupling efficiency from the tapered silica fibers into ZnO. We study the evanescent field of ZnO nanowires as a function of their diameter and analyze the condition for single-mode and multi-mode waveguiding. In both the experiments and simulations we find that for typical ZnO nanowire diameters of about 250 nm and laser light in the visible spectral region, the coupling from silica to ZnO nanowires frequently leads to the excitation of high-order waveguide modes. We also use our combination of silica and ZnO nanowires to study the emission of low-order waveguide modes from the end facets of the ZnO nanowires and compare the results with our simulations.

5.1 The ZnO material system

The investigation of the structural, electrical and optical properties of semiconductor nanowires has been an active field of research for the past couple of years because these nanowires afford a large variety of novel nanoscale electronic and optoelectronic devices like piezoelectric nanogenerators [104], field effect transistors [105], light emitting diodes [106, 107], lasers [108, 109] and waveguides [108, 109, 18, 110, 111]. These applications are feasible because the high crystalline quality, low defect density, smooth sidewalls, and well-defined end facets of the nanowires make them suitable as waveguides and res-

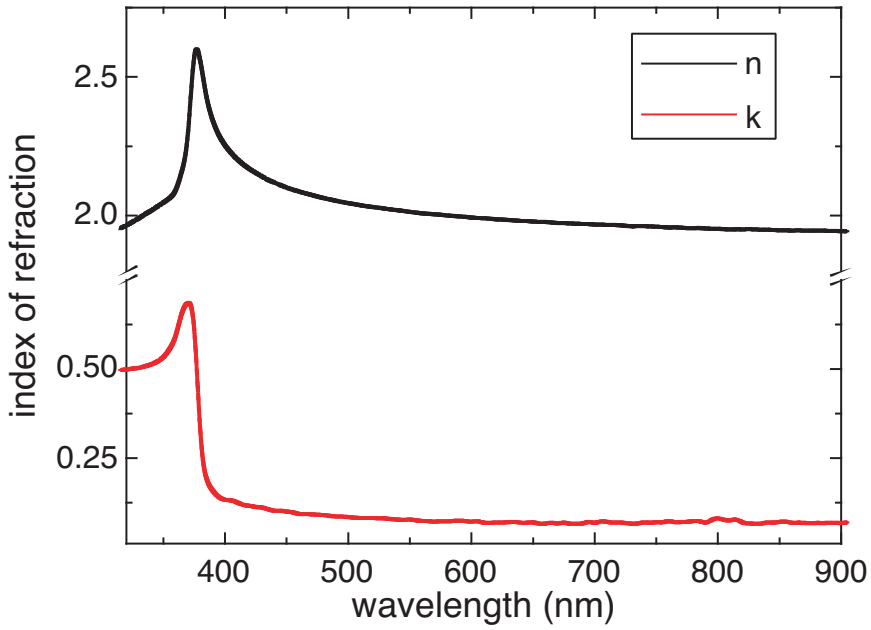

Figure 5.1: The real and imaginary refractive index of bulk ZnO.

onators for optical modes in the visible or near IR spectrum.

In particular, nanowires made of the large bandgap, wurtzite II-VI semiconductor zinc oxide (ZnO) have been extensively investigated because this material system is a promising candidate for the fabrication of nanoscale light emitters in the near-UV spectral region [112, 113, 114]. Furthermore, ZnO is an easy to handle, non-toxic material possessing a large exciton binding energy (60 meV), [111] which allows efficient excitonic light-emission processes even at room temperature. ZnO nanowires can be grown in large quantities in a well-defined diameter range up to lengths of several tens of micrometers in high-temperature vapor-liquid-solid growth processes, sometimes with gold as catalyst.

The real and imaginary parts of the refractive index of bulk ZnO is shown in Figure 5.1. The notable features of the ZnO refractive index are the absorption peak centered around 370 nm, corresponding to the room-temperature ZnO band-gap of 3.37

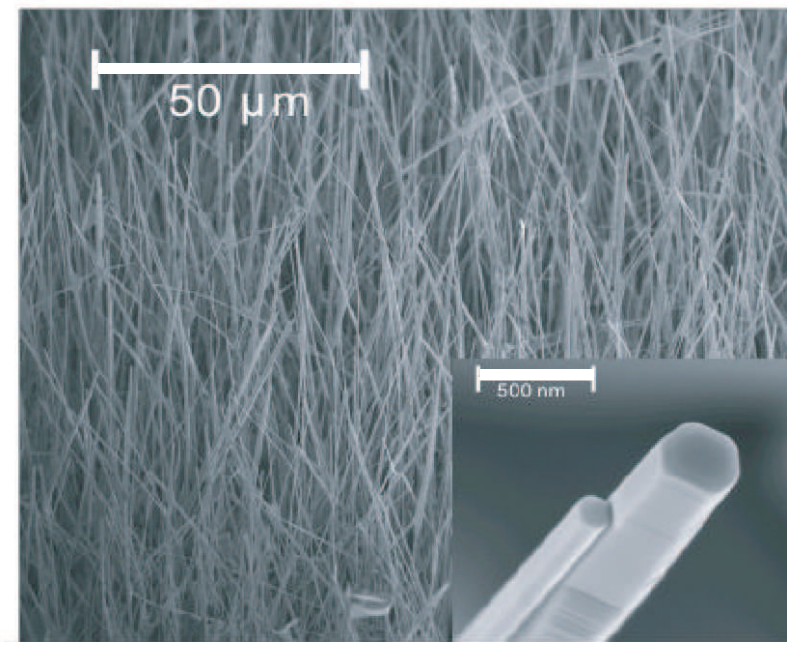

Figure 5.2: The as-grown ZnO nanowires with lengths up to 100 μm long and diameters 40 and 500 nm. The inset shows the hexagonal cross-section of the ZnO nanowires. After Ref. [114]

eV [112, 115], and the relatively flat value of $n = 2.0$ across most of the visible spectrum. Since the index contrast between ZnO and air is higher than the contrast between silica and air, the mode confinement will be stronger in ZnO wires than in silica wires of similar diameter. The waveguide simulations in Section 5.3 use the value of $n = 2.0$ for the material index of ZnO. The roughly flat value of the index through the visible regime allows for the scalability of the important parameters of the simulations, such as d_{ZnO}, d_{silica}, and λ.

We synthesized single crystalline zinc oxide (ZnO) nanowires in a horizontal tube furnace by a vapor transport technique [26]. High-purity ZnO powder was placed in an alumina boat and heated to an evaporation temperature of 1620 K. Silicon substrates covered with a 4-nm thin Au film were placed at the cooler end of the tube furnace with a temperature of around 1370 K. The vapor was transported at a pressure of 100 mbar by

Ar gas flow of 50 sccm to the substrates initiating the catalytic driven vapor-liquid-solid (VLS) growth process [116] of the ZnO nanowires. The as-deposited nanowires are typically up to 100 μm long and between 40 and 500 nm in diameter, as determined by scanning electron microscopy (SEM), shown in Figure 5.2. Energy-dispersive spectrometry reveals only stoichiometric zinc and oxygen signals; transmission electron microscopy and x-ray diffraction confirm that the nanowires are of wurtzite structure and the c-axis is in the growth direction.

5.2 Experimental Setup

We mechanically disperse 20-μm to 80-μm long ZnO nanowires onto thin glass substrates coated with a 800-nm thick mesoporous silica film [54, 55]. The mesoporous films have monodisperse, 8-nm wide pores and are deposited using a dip-coating process. The resulting films have a refractive index of about $n = 1.185$ throughout the visible spectral region, [54] preventing parasitic coupling into the substrates. Combined with their extremely high homogeneity and flatness, these layers also help minimize losses and noise due to scattering at the output sides of the silica and ZnO nanowires, which is crucial when investigating coupling and waveguiding processes. Because the refractive index of mesoporous silica is much lower than that of both the silica and ZnO nanowires, we can treat the nanowires as freestanding, air-clad waveguides in our numerical simulations.

To couple light into the semiconductor nanowires we use silica nanowires fabricated by techniques described in Section 2.2. Silica nanowires and tapered fibers are fabricated by taper drawing from standard silica optical fibers [25] with lengths of up to several tens of millimeters and a high diameter uniformity. External laser light and white light sources can be easily coupled into the silica nanowires through the macroscopic optical fiber to which

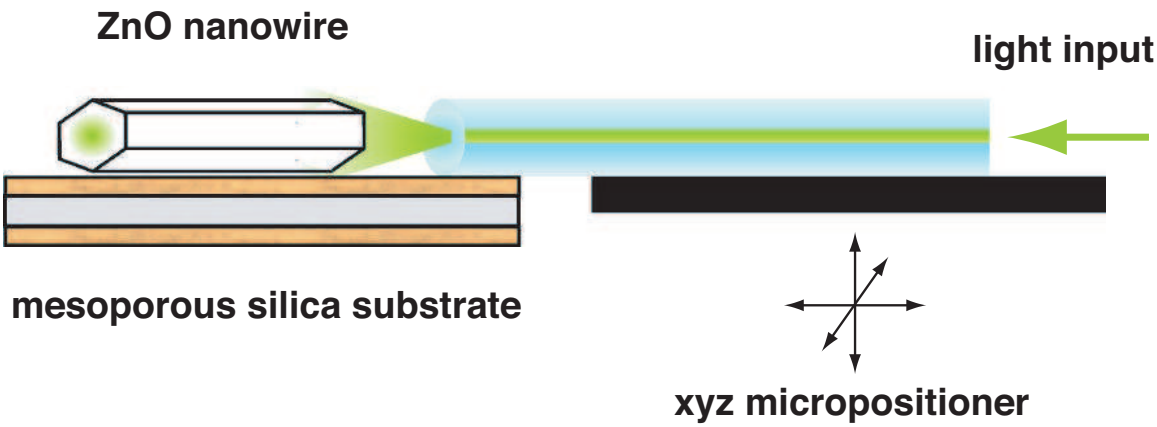

Figure 5.3: Diagram of the experimental setup for coupling light from tapered silica fibers into ZnO nanowires.

the nanowires are still attached. The tapered and submicrometer diameter silica wires used for these experiments were produced using a conventional fiber tapering technique [60]. The fiber-pulling setup consists of a regulated hydrogen torch and two computer-controlled linear stages as shown in Figure 2.5. The parameters for the fiber-pulling system, such as speed, acceleration, fiber tension and position of the flame, were optimized to yield low-loss taper regions.

To study the coupling and waveguiding properties of the ZnO nanowires, we launched continuous wave laser light ($\lambda = 532$ nm, $P = 1$ mW) and broadband white light ($P = 1$ W) into a silica optical fiber mounted on a micropositioning stage as shown in the diagram in Figure 5.3. We used either the as-fabricated silica nanowires or cut them off close to the tapered region, using the end of the tapered region to couple light into the ZnO nanowires. We observed the coupling using an inverted microscope with a 100x oil-immersion objective (numerical aperture 1.4) and used the micropositioning stage to bring the end of the silica fiber near an individual ZnO nanowire.

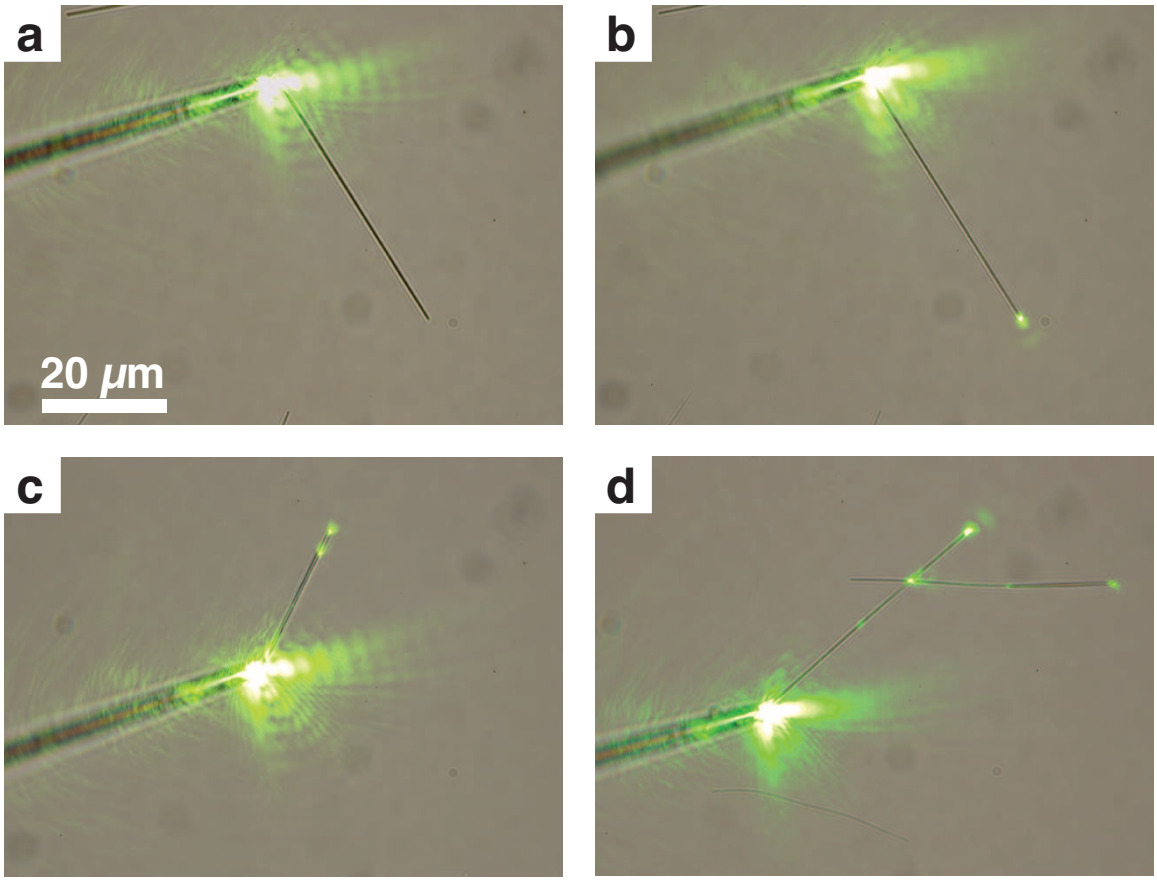

Figure 5.4: Waveguiding in single ZnO nanowires. (a) Tapered silica fiber close to the nanowire but no coupling. (b) Coupling of light into a low-order waveguide mode of the ZnO nanowire. (c) Nanowire with imperfections leading to additional losses and two output points. (d) Coupling between two ZnO nanowires lying on top of each other.

5.3 Results

Figure 5.4 shows the coupling of green laser light from the tapered silica fiber into a ZnO nanowire. We observe no coupling between the two waveguides at all (Fig. 5.4a) until the distance between them is smaller than about 1 μm and light is seen exiting the end facet (Fig. 5.4b). Figure 5.4c shows the emission of light from a growth imperfection along the length of the nanowire. In Fig. 5.4d we show that light also couples efficiently between two ZnO nanowires lying on top of each other.

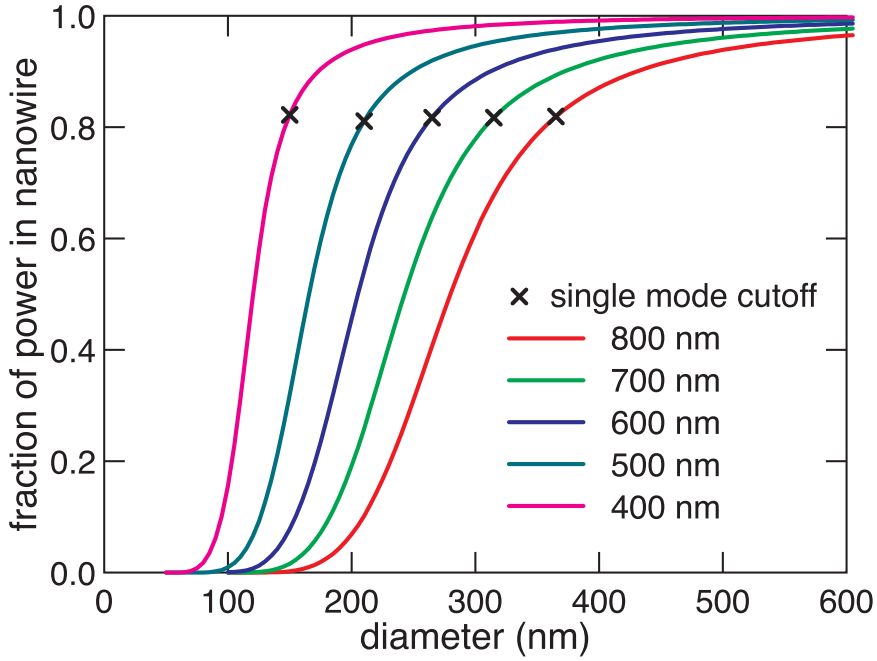

Figure 5.5: Diameter and wavelength dependence of the fraction of power guided in the lowest order HE11 mode inside a cylindrical ZnO nanowire. The remaining part of the power is guided in the evanescent field. The crosses show the transition between the single-mode and multi-mode waveguiding regimes (single-mode guiding occurs for diameters smaller than that at the cross).

In order to understand the relevant properties and mechanisms that govern the waveguiding and coupling observed in Figure 5.4, we performed numerical simulations of the mode distribution in the visible part of the spectrum, where ZnO is completely transparent. We started with an analytically solvable model [30] treating the ZnO nanowire as a perfect cylinder, neglecting its hexagonal structure. The simulations include the dispersion of ZnO by approximating the refractive index with a Sellmeier type equation [115].

In Figure 5.5 we show the wire-diameter and wavelength dependence of the calculated power of the lowest-order HE11 mode that is carried inside the cylindrical ZnO nanowire. In comparison with the same calculations for silica nanowires, shown in Figure 2.2c, the power in the core for ZnO nanowires is higher for a given diameter nanowire. The

crosses mark the transition from single-mode to multi-mode waveguiding obtained from the condition [30] for single-mode waveguiding: $2\pi d/\lambda_0(n_1^2 - n_{air}^2)^{1/2} < 2.405$, where d is the wire diameter, λ_0 the vacuum wavelength, and n_1 and n_{air} are the refractive indices of ZnO and air, respectively. The transition occurs when the power guided in the ZnO nanowires is less than about 80%.

The calculation in Figure 5.6 shows explicitly the transition from multi-mode waveguiding to single-mode waveguiding for a given diameter of a ZnO nanowire and wavelength of light. The critical diameter for single-mode waveguiding is in the range between $d = 350$ nm ($\lambda = 800$ nm) and $d = 150$ nm ($\lambda = 400$ nm). Figure 5.5 shows that the fraction of power guided inside the nanowire sharply decreases below the critical diameter, especially at short wavelengths. The results in Figure 5.5 and Figure 5.6 agree with previous results obtained for silica and silicon nanowires [30]. The diameters of the ZnO nanowires used here is about 250 nm, thus we expect higher-order waveguiding for wavelengths below $\sim$600 nm.

Figure 5.7a and b show that a slight change in the alignment of the silica tapered fiber with respect to the ZnO nanowire dramatically changes the coupling and waveguiding conditions. In Figure 5.7a the coupling, guiding and emission of the waveguide mode is the same as in Figure 5.4b, but a small adjustment of the tapered fiber leads to the excitation of high-order waveguide modes (Fig. 5.7b). These high-order modes carry a significant additional fraction of power at the nanowire surface and even outside the nanowire as evanescent fields. This can be seen by comparing the emitted intensities at the nanowire ends in Figures 5.7a and 5.7b.

High-order modes can also be generated at imperfections along the ZnO nanowire. Figure 5.7c shows a transition from single-mode to multimode waveguiding along a nanowire. An SEM picture of that nanowire shows that the diameter of the nanowire increases at the

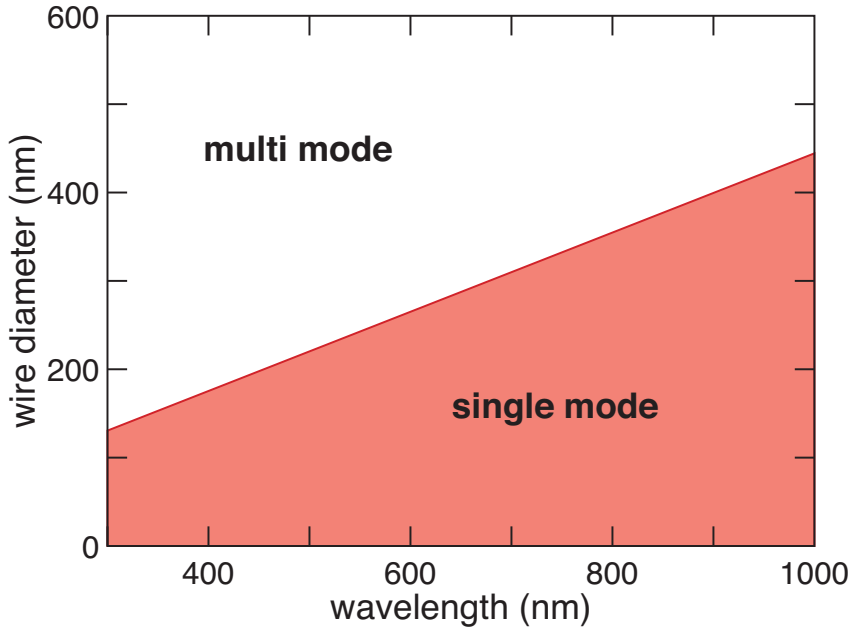

Figure 5.6: Calculation of the single mode and multi mode regimes for a range of ZnO nanowire diameters and wavelengths.

transition point (Fig. 5.7d). We observed many nanowires that exhibited a similar single- to multimode transition.

We also directly couple broadband light into the waveguide modes of ZnO nanowires. Figure 5.8 shows a white light source launched along a ZnO nanowire via a silica fiber taper. The wavelength-dependent loss shown in Figure 5.8a reveals another indication of the nanowire diameter change seen in Figure 5.7d. Broadband waveguiding is observed in both the bright field and dark field images in Figure 5.8b.

An enlarged view of the end of the nanowire in Fig. 5.7a shows the emission profile (Figure 5.9a). The dashed white lines show that the cone emission angle is about 90°. Figure 5.9b shows a finite-difference time domain (FDTD) simulation [117] of the emission of a single-mode pulse from a ZnO nanowire using a constant index of refraction ($n = 2$), which, as Figure 5.1 shows, is a reasonable approximation for visible wavelengths.

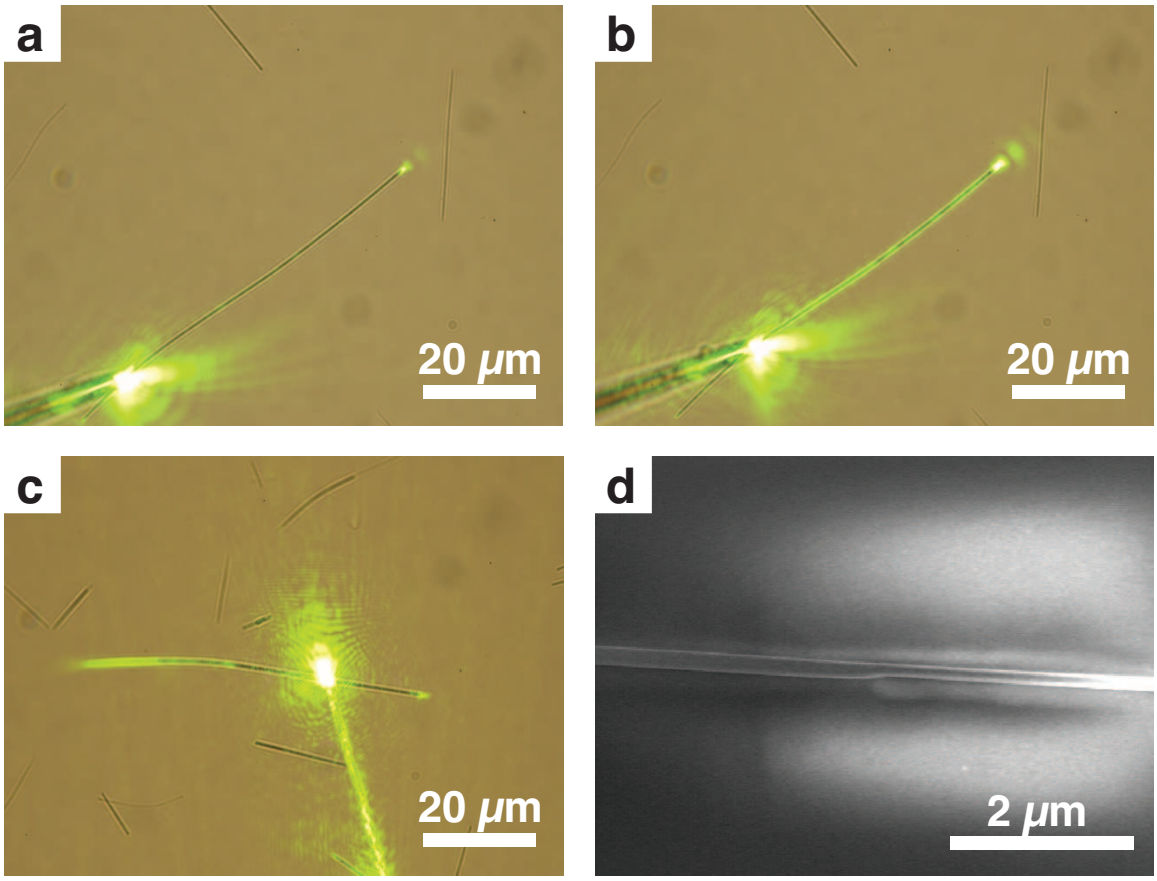

Figure 5.7: Experimental observation multi-mode waveguiding. Top row: a slight change in the alignment of the silica nanowire changes the mode excited in the ZnO nanowire from (a) a low-order to (b) a high-order mode with a significant intensity guided at the surface. Scattering at the high-quality substrates leads to low losses of this mode which make this mode visible under the microscope. (c) High-order mode can also be excited when the diameter of the nanowire changes. (d) SEM picture showing the diameter change that causes the excitation of the higher-order modes in (c).

We plot the square of the electric field in the z-direction (perpendicular to the plane of the figure) after the pulse has been emitted from the right end of the nanowire. A small fraction of the light has been reflected and travels back to the left inside the nanowire. The lateral dimensions are given in units of the ZnO nanowire diameter d_{ZnO} and the wavelength has been chosen to be $2.66 d_{ZnO}$, which corresponds to the situation in Figure 5.9a ($\lambda = 532$ nm and $d = 200$ nm). The simulation confirms our experimental observation of directed

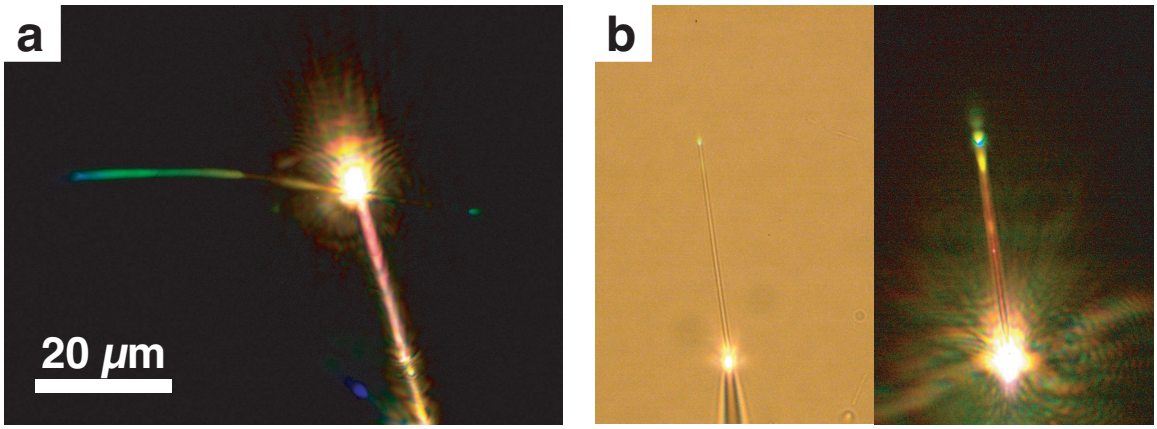

Figure 5.8: A white light source coupled from silica tapered fiber into ZnO nanowires. (a) The ZnO nanowire in Figure 5.7c reveals wavelength-dependent losses when white light is launched into the waveguide. (b) Bright and dark field images of broadband waveguiding in a ZnO nanowire. Both images were taken at the same magnification.

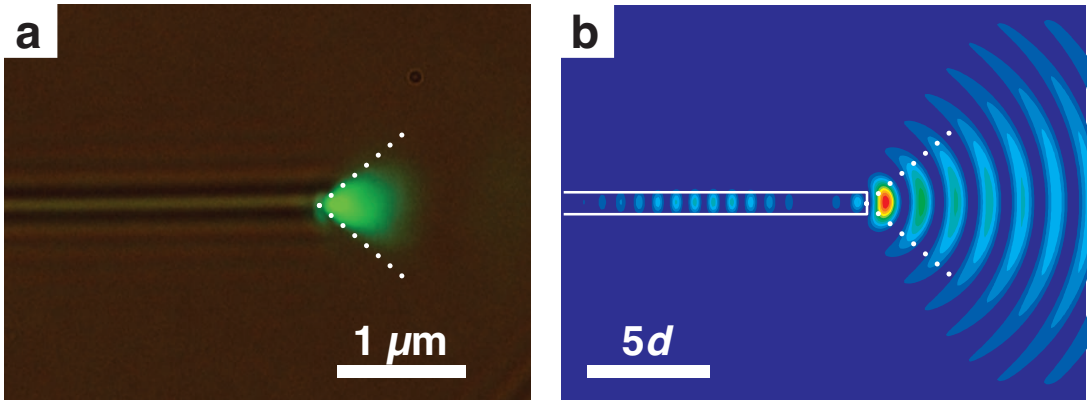

Figure 5.9: (a) Magnified view of the conical emission of a low-order guided mode from a ZnO nanowire. The emission angle is approximately 90° (dotted lines). (b) FDTD calculation of the square of the electric field of a light pulse propagating along a nanowire of diameter d with a wavelength of $2.66d$.

emission from the nanowire waveguide mode into a cone with an angle of about 90° as indicated by the dotted white lines in Figure 5.9a.

As our results in Figures 5.5 and 5.7 demonstrate, ZnO nanowires with diameters around 200 nm can serve as multimode waveguides for visible light. In order to determine

the maximum achievable coupling efficiency and to understand the origin and properties of the high-order waveguide modes, we numerically simulated the waveguiding and coupling between silica and ZnO nanowires using the FDTD technique [117]. The results of the FDTD simulations are scalable if the wavelength and the lateral dimensions of the nanowires are multiplied by the same number, over the region where the linear refractive indices of the involved materials are constant. For the simulations presented here, we assume constant refractive indices of $n_{ZnO} = 2$, $n_{silica} = 1.46$, and $n_{air} = 1$, which is a good approximation for the wavelength range between 400 nm and 1000 nm. We simulated the propagation of a pulse from a silica to a ZnO nanowire for various angles between the symmetry axes of the junction, as shown in the inset in Figure 5.10. A light pulse uniformly illuminates the left end of the silica fiber, exciting a low-order mode that travels to the right. At the interface between the silica and the ZnO nanowire, part of the pulse is reflected, a second part is scattered, and a third part is coupled into the waveguide modes of the ZnO nanowire.

To estimate the coupling efficiency, we calculated the transmission into the ZnO nanowire by dividing the integrated power in the ZnO nanowire by the integrated power coupled into the silica nanowire. Figure 5.10 shows how this transmission depends on the angle between the nanowires given a diameter ratio of $d_{silica} = 4d_{ZnO}$ and letting the central wavelength of the light pulse (measured in vacuum) be three times the diameter of the ZnO nanowire, so that $\lambda = 600$ nm, $d_{ZnO} = 200$ nm, and $d_{silica} = 800$ nm, in accordance with our experimental conditions. The simulations show that the coupling efficiency exceeds 0.50 for angles up to 50°. For angles larger than 50° the transmission decreases substantially, but remains above 0.10 even when the nanowires are perpendicular to each other. Varying the wavelength between $2d_{ZnO}$ and $4d_{ZnO}$ (not shown here) changes the transmission by less than 0.1. Likewise, we find that the transmission depends weakly (< 0.1) on the diameter ratio for the range $2 < d_{ZnO}/d_{silica} < 4$. Introducing a small gap between the two nanowires

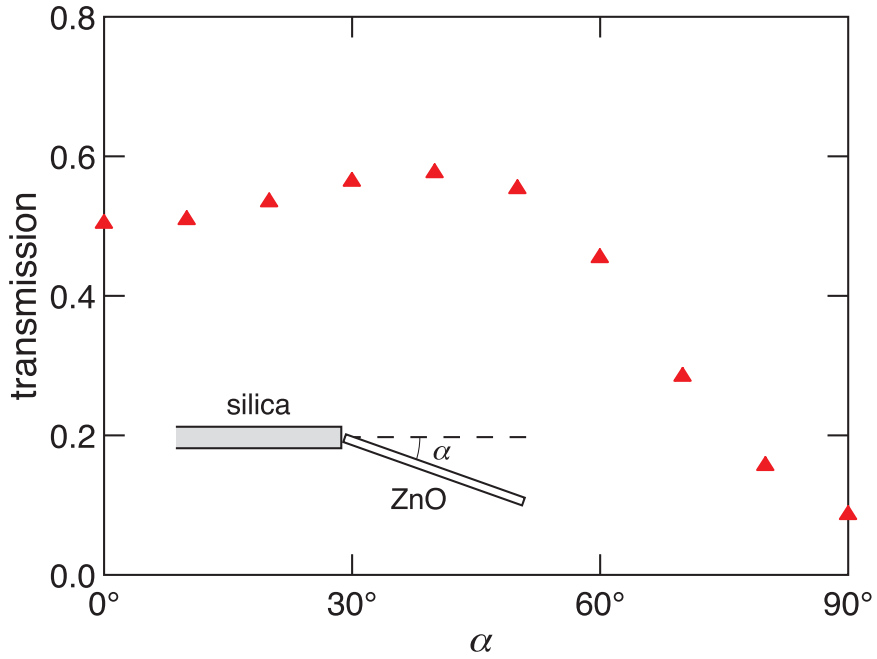

Figure 5.10: Coupling efficiency between a silica fiber with 1 μm diameter and a ZnO nanowire with 250 nm obtained from numerical FDTD simulations. Transmission as a function of the angle between the silica fiber and the ZnO nanowire. The inset shows the geometry used in the simulation.

(gap length $\leq \lambda/5$) decreases the transmission by only a few percent.

Figure 5.11 shows the wavelength dependence of the transmission for two nanowire angles of 10° and 60°. The wavelength scale covers the range from $2d_{ZnO}$ to $4d_{ZnO}$ which corresponds to 400 nm $< \lambda <$ 800 nm for our experimental condition ($d_{ZnO} = 200$ nm). For both angles, the transmission spectra show the same general wavelength dependence. The main difference between the two angles is that the transmission at 60° is about $0.10 - 0.25$ smaller. This difference is in line with the results presented in Figure 5.10. The transmission spectra show that the coupling efficiency decreases as we decrease the wavelength from a value of $4d_{ZnO}$; the simulations show that this decrease is due to increased scattering at the interface between the nanowires. Below a wavelength of $2.5d_{ZnO}$ the transmission increases sharply for both angles. At an angle of 10° the transmission exceeds 0.7, significantly higher

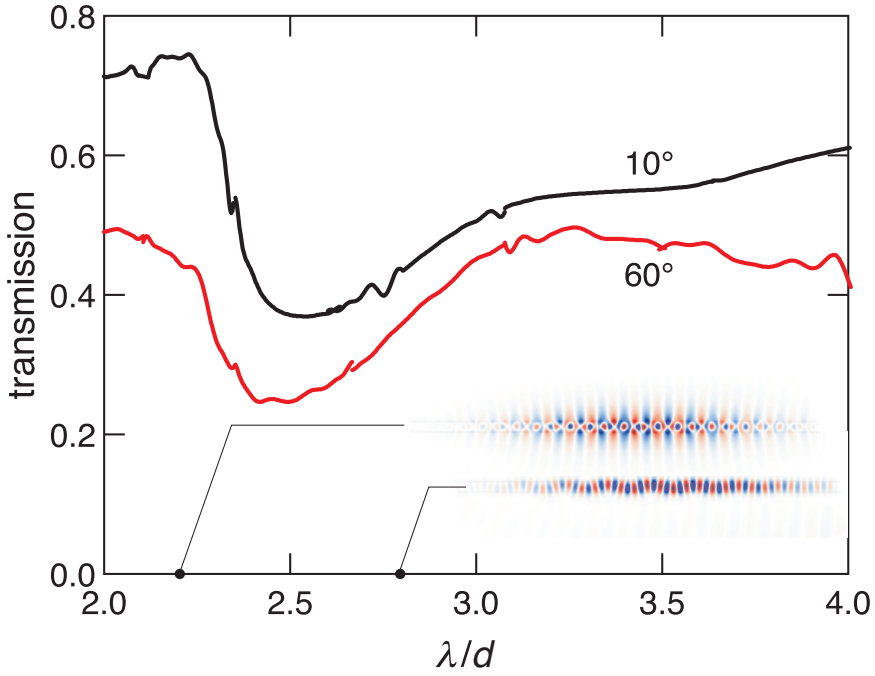

Figure 5.11: Coupling efficiency between a silica fiber with 1 μm diameter and a ZnO nanowire with 250 nm obtained from numerical FDTD simulations. Transmission as a function of the wavelength for two different coupling angles. The inset shows the simulated two-dimensional electric field profiles in the ZnO nanowire at $\lambda/d = 2.2$ and 2.8.

than at longer wavelengths.

The inset in Figure 5.11 shows the mode profiles of the transmitted pulse at wavelengths of $2.2d_{ZnO}$ and $2.8d_{ZnO}$. The blue and the red correspond to maximum negative and positive amplitudes of the electric field, respectively. The profile for the long-wavelength pulse shows a low-order mode with a noticeable zigzag-like propagation through the ZnO nanowire. The profile for the short-wavelength pulse shows additional high-order mode components with strong field amplitudes at the nanowire surface and significant evanescent-field amplitudes.

5.4 Discussion

Although the photoluminescence properties of semiconductor nanowires have been studied experimentally [112, 113, 118, 119], their waveguiding properties remain largely unexplored. One reason is the lack of a robust, efficient, and well-understood optical technique to study individual nanowires. Figure 5.4 shows that silica tapered fibers and silica nanowires are convenient, robust, and efficient tools to controllably inject light into the waveguide modes of individual semiconductor nanowires. As Figures 5.4a and 5.4b show that a considerable amount of light can be coupled into ZnO nanowires even when the angle between the two waveguides is large. Our technique thus permits the convenient and systematic study of the waveguiding properties of semiconductor nanowires. The technique can also be used to scan nanowires for potential imperfections and sources of additional loss (as shown in Figure 5.4c) before they are further processed into devices. The simple two-nanowire system in Figure 5.4d shows that silica tapered fibers can be used to characterize the performance and loss of more complex optical nanowire circuits.

The low-index and low-loss mesoporous silica substrates prevent parasitic scattering from overshadowing the waveguiding characteristics. Because no light is emitted or scattered from any other part but the nanowires end facet (Fig. 5.4b), we can conclude that no significant losses occur during the waveguiding of low-order modes in the ZnO nanowire. The large index contrast between the waveguide materials and the mesoporous silica allows us to directly compare experimental results with simulations of air-clad waveguides.

The index of refraction n of semiconductor nanowires typically ranges between 2 and 4 and so the wavelength λ_{air}/n in these materials is substantially reduced. Consequently the critical diameter for single mode waveguiding is distinctly smaller than for silica nanowires. Conversely, for a nanowire of fixed diameter, the limit for single-mode

waveguiding is farther into the blue spectral region than for silica nanowires. Figure 5.5 shows that at the single-mode cutoff for ZnO ($n = 2$), 80% of the mode energy is confined in a small spatial region with a diameter between 150 and 350 nm, which is precisely the range of diameters for VLS-grown ZnO nanowires. The strong confinement is very desirable for efficient and low-loss waveguiding and wiring of light at the nanoscale.

The large index contrast between the ZnO and silica nanowires causes the excitation of high-order modes with substantial evanescent fields in ZnO nanowires, even for nanowires with diameters just slightly exceeding the single mode limit. As the high-order mode propagates, these evanescent fields scatter at the surface of the nanowire, leading to the green appearance in Figure 5.7b.

The experimental results in Figure 5.7a,b and the simulations in Figure 5.10b both show that the excitation of high-order modes is controlled by the alignment between the nanowires. Depending on the application, either low- or high-order modes may be preferable. For example, the strong confiment provided by low-order modes enables low-loss nanoscale waveguiding. Likewise, low-order modes would maximize the overlap between the optical field and the semiconductor material in semiconductor amplifiers. On the other hand, high-order modes could be used to achieve efficient evanescent sensing and enhance coupling efficiency, as demonstrated in Figures 5.7a and b.

Our experiments show that the acceptance angle for launching waves into ZnO nanowires is large. Because the propagation of light is reversible, the acceptance and emission angles should be the same. Indeed, the emission cone angle of the nanowires is approximately 90°, as shown in Figure 5.9. While this angle is large, the emission is still clearly directed and the nanowire ends cannot be considered point sources, as previously reported for actively emitting short ZnO nanowires [120].

The FDTD simulations presented in Figure 5.9 confirm the high coupling efficiency

between the waveguide modes in the silica fibers and ZnO nanowires. Although the experimentally achievable efficiency might still be significantly below the theoretical value of 0.50, the simulations show that the efficiency is varies little for changes in alignment for angles less than 50°. This maximum angle of 50° is in excellent agreement with the experimental observation of a 90° cone angle for emission in Figure 5.9. Within experimental accuracy this cone angle is approximately twice the angle at which the coupling efficiency starts to decrease, as theoretically expected. The simulations show that the main physical parameter that determines the coupling efficiency is the large index contrast between both waveguide materials.

Figure 5.11 shows that for wavelengths above $2.5d_{ZnO}$ the transmission increases with increasing wavelength. The profiles of the electric field obtained in the simulations reveal that as the wavelength increases, scattering at the interface between the two wires decreases, increasing the amount of light that is coupled to the ZnO nanowire. For all angles studied the transmission reaches a minimum at wavelengths around $2.5d_{ZnO}$. Below this wavelength the transmission is significantly higher. As the single mode cutoff regime in Figure 5.6 and the mode profiles in the inset of Figure 5.11 show, this increase coincides with the excitation of high-order modes during the coupling from the silica to the ZnO nanowire.

5.5 Conclusions

In summary, we used silica nanowires and tapered fibers to efficiently and controllably inject laser light into individual ZnO nanowires and study their waveguiding properties. The ZnO nanowires are placed on glass substrates covered with a layer of low-index mesoporous silica to prevent coupling of light from the silica tapered fibers into the glass substrate

and achieve very low parasitic scattering at the nanowire output facets. Finite-difference time domain simulations reveal the dependence of the coupling efficiency from the silica into the ZnO nanowires on the angle between them and on the wavelength of the guided modes. The maximum efficiency can theoretically reach 50%. We showed that high-order waveguide modes with high intensities at the nanowire surface are frequently excited when light is coupled between nanowire waveguides of different refractive indices. We studied the single- and multimode waveguiding conditions for ZnO nanowires in numerical simulations and calculated the evanescent field strength of the lowest order mode of a cylindrical ZnO nanowire. We analyzed the emission of waveguide modes for ZnO nanowires ($d \sim 200$ nm) both experimentally and in simulation and found a typical emission angle of 90°. The wavelength dependence of the transmission efficiency and the behavior of high-order modes presented here facilitate the interpretation of semiconductor nanowire experiments and the optimization of semiconductor nanowire devices.

Chapter 6

Femtosecond pulse excitation of ZnO nanowires

In Chapter 5, we used a technique of coupling broadband and laser light directly into the waveguiding modes of ZnO nanowires by means of tapered silica fibers and nanowires. The combination of the top-down fabrication of silica nanowires with the bottom-up fabrication of ZnO nanowires allowed us to study the passive waveguiding properties and to characterize the quality of the ZnO nanowires. As we have shown in chapters 3 and 4, we can use silica nanowires to assemble nonlinear microphotonic devices. ZnO nanowires, with their higher index and nonlinearity [121, 115, 122, 123, 124], and the high degree of control over the growth parameters [26], are also promising candidates for micro- and nanophotonic device fabrication.

In this chapter, we examine the response of single ZnO nanowires to excitation from femtosecond-laser pulses. We measured the transmission characteristics of single ZnO nanowires under femtosecond-pulse excitation. We find that the excitation generates the second harmonic and photoluminescence in the ZnO nanowire, which couples into low-order

waveguide modes of the nanowire but with distinctly different efficiencies. We measure the transmission spectrum of a single ZnO nanowire for near-UV light generated by interband recombination processes. The transmission spectrum allows us to determine the absorption edge of the excited nanowire and to study the temperature profile of the nanowire under femtosecond-pulse excitation, which agrees with finite-element simulations of local heating in a ZnO nanowire. Ultimately, understanding how various thermal and mechanical properties that affect the nanowire transmission properties will become important concerns when engineering future nonlinear photonic devices.

6.1 ZnO as a nonlinear material system

Zinc oxide (ZnO) is a non-toxic, wide-bandgap semiconductor used in electronic and near-UV optoelectronic devices such as sensors, light emitters and detectors [112, 125]. ZnO has received much attention because it is easy to fabricate large quantities of high-quality ZnO nanowires with diameters of a few hundred nanometers and lengths of several tens of micrometers [106, 108, 26]. Such nanowires are transparent throughout the visible spectral region, due to the large room-temperature band gap $E_{gap} = 3.37$ eV of ZnO [112, 115]. Furthermore, because of the large refractive index of ZnO across the visible spectrum ($n > 2$) [115], ZnO nanowires are excellent low-loss sub-wavelength waveguides. The large index provides tight optical confinement for low-order modes and also results in a large acceptance angle for coupling light into the nanowire waveguide. Although the hexagonal cross-section of the nanowires influences the intensity profile of higher-order modes, the lowest order mode exhibits almost circular symmetry inside the nanowire [109]. The semiconducting properties of the material permit the fabrication of nanowire devices in which gain and refractive index can be electrically modulated [106, 108, 107, 19, 18]. How-

ever, efficient and reliable p-type doping of ZnO remains an unsolved problem hindering the design of electrically operated nanowire devices [125].

Because ZnO is a highly polar semiconductor it is frequently used for frequency doubling of intense ultrashort laser pulses [126]. Several studies report on the non-linear coefficients [126, 124, 122, 123, 127] of *c*-plane and *a*-plane ZnO thin films, and on second-harmonic generation [128] and polariton effects [120] in ZnO nanowires.

In this work, we show that excitation of individual ZnO nanowires with ultrashort laser pulses excites waveguide modes in the nanowires. We study the coupling and transmission efficiency of the photoluminescence and second-harmonic generation in the nanowire. We perform transmission measurements on a single nanowire and determine the absorption edge of the highly excited semiconductor material. The absorption edge allows us to deduce an upper limit for the local temperature of the nanowire close to the excitation spot. We perform finite-element simulations to model the heat distribution of a ZnO nanowire under excitation with intense femtosecond-laser pulses. These simulations show how light-induced thermal effects change the nanowire transmission properties which provides a window for studying fundamental material properties of the ZnO nanowires.

6.2 Experimental Setup

We grow ZnO nanowires by a vapor transport technique using high-purity ZnO powder as source material [26] as described in Section 5.2. We mechanically disperse the nanowires onto glass slides that are covered with 800-nm thick films of mesoporous silica [54, 55], yielding nanowires of $20-60$ μm length, $200-400$ nm diameter, and a separation between the nanowires that is large enough to study single nanowires. The mesoporous silica films have a low refractive index, $n = 1.185$, throughout the whole visible spectrum [54, 55].

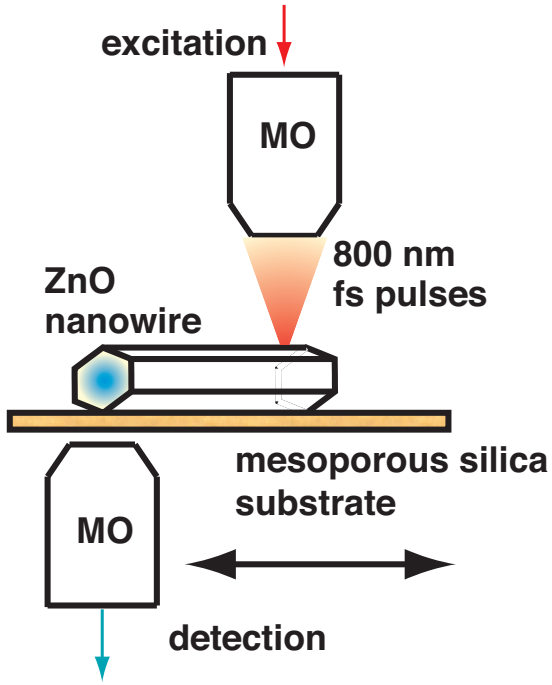

Figure 6.1: Schematic diagram of our experimental setup. A ZnO nanowire is lying on a glass slide covered with a 800-nm layer of low-index mesoporous silica. The nanowire is excited from the top perpendicular to one of its a-planes. The emission from the nanowire is observed with an inverted microscope.

The low index creates a large index contrast $\Delta n = 0.8$ between nanowire and substrate, which, when combined with the high homogeneity and flatness of the mesoporous layer, helps prevent parasitic scattering and coupling into the substrate.

We performed the experiments described in this chapter using an inverted microscope, shown schematically in Figure 6.1. The nanowires are excited from the top with the fundamental 800-nm pulses from a femtosecond laser oscillator (60 fs; 11 MHz; 80 nJ) [95]. The incident radiation is normal to the waveguide direction of the nanowires. A reflection type objective (40x; 0.5 NA) focuses the laser pulses onto the nanowires to a spot size with a diameter < 10 μm. We estimate the typical excitation fluence at the excitation spot to be 0.45 kJ/m^2, well below the damage threshold for ZnO nanowires which we determined to

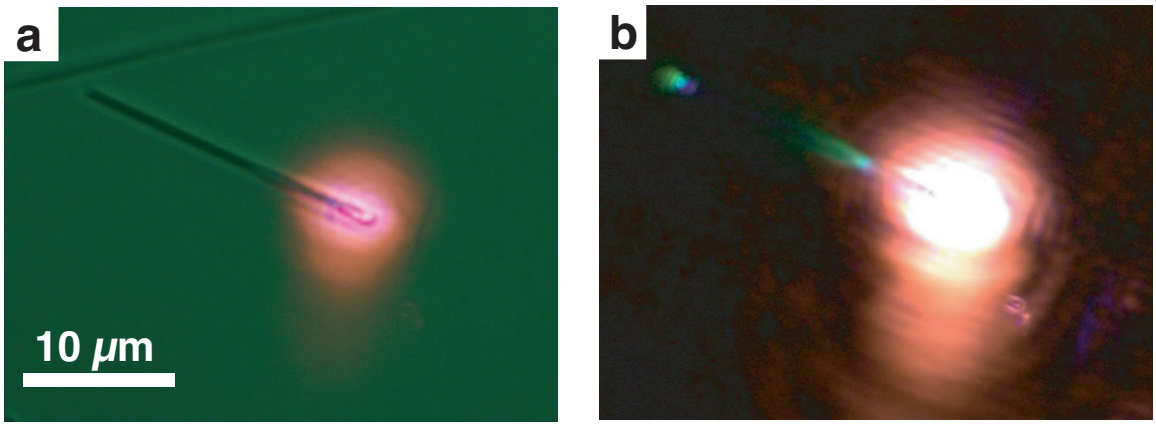

Figure 6.2: Microscope image of a single ZnO nanowire under infrared fs-pulse excitation. (a) At low fluence, the position of the nanowire and the location of the excitation spot are shown. (b) Near the excitation spot residual infrared light, blue and green photoluminescence, and second harmonic light can be observed. The far end of the nanowire shows emission of photoluminescence that is guided along the length of the nanowire without visible waveguiding losses.

be about $5 - 10$ times higher. Using a fiber-coupled spectrometer, we spatially resolve the emission spectrum of the nanowire at the image plane of an output port of the microscope. A BG40 color-glass filter attenuates the 800-nm signal from the excitation pulses while providing high and nearly constant transmission over the entire ZnO emission spectrum (transmission between 0.85 and 0.90 between 350 and 550 nm).

6.3 Results

Figure 6.2 shows a microscope image of a ZnO nanowire excited at one end with 800-nm fs pulses. At low fluence, as shown in Figure 6.2a, we align the location of the excitation spot to the position of the ZnO nanowire. In spite of the BG40 filter, residual red light is still clearly visible around the excitation spot. Increasing the excitation fluence to 0.45 kJ/m^2 as shown in Figure 6.2b, we observe blue and green emission close to the excitation spot.

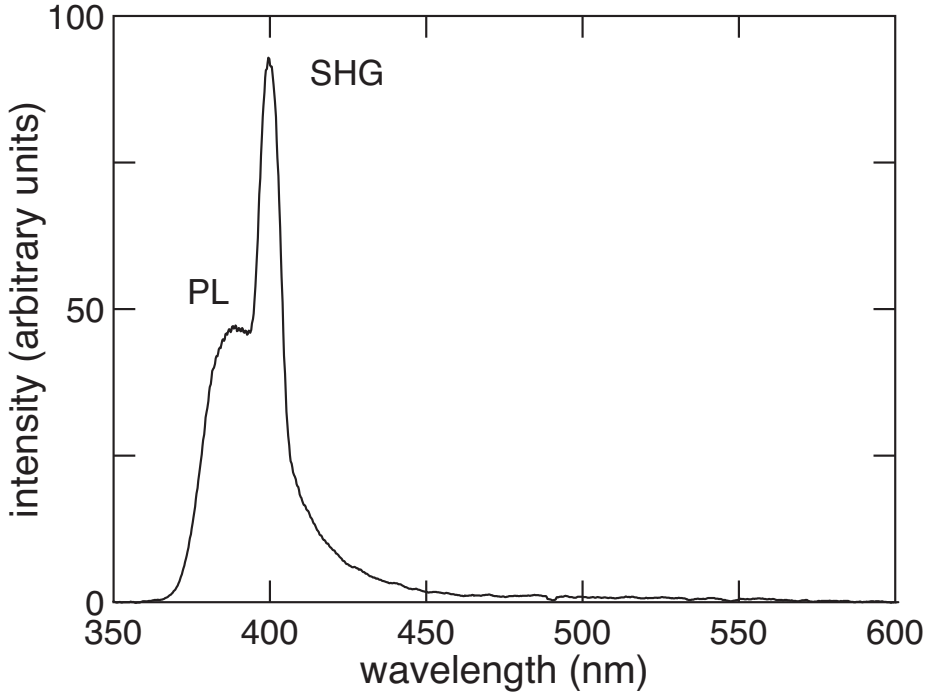

Figure 6.3: Spectrum of the light collected directly at the excitation spot of a single nanowire irradiated by 800-nm fs pulses. The second harmonic (SHG) of the laser line is clearly visible at 400 nm on top of a photoluminescence (PL) pedestal ranging from $370-450$ nm. Between 475 nm and 575 nm we find weak green emission from deep centers.

Figure 6.3 shows a spectrum of the emission. In addition to a pronounced second-harmonic peak at 400 nm, the spectrum shows photoluminescence from excitonic recombination located at 385 nm and from deep centers in the ZnO nanowires centered around 500 nm [125]. Figure 6.2 also shows that part of the photoluminescence and second-harmonic of the excitation pulses is guided to the far end of the nanowire where we can clearly see the blue and green components of the emission from the waveguide mode. Apart from the regions directly around the excitation spot and at the far end of the nanowire, no further emission from the nanowire waveguide is visible.

Figure 6.4 compares the spectra measured directly at the excitation spot (input)

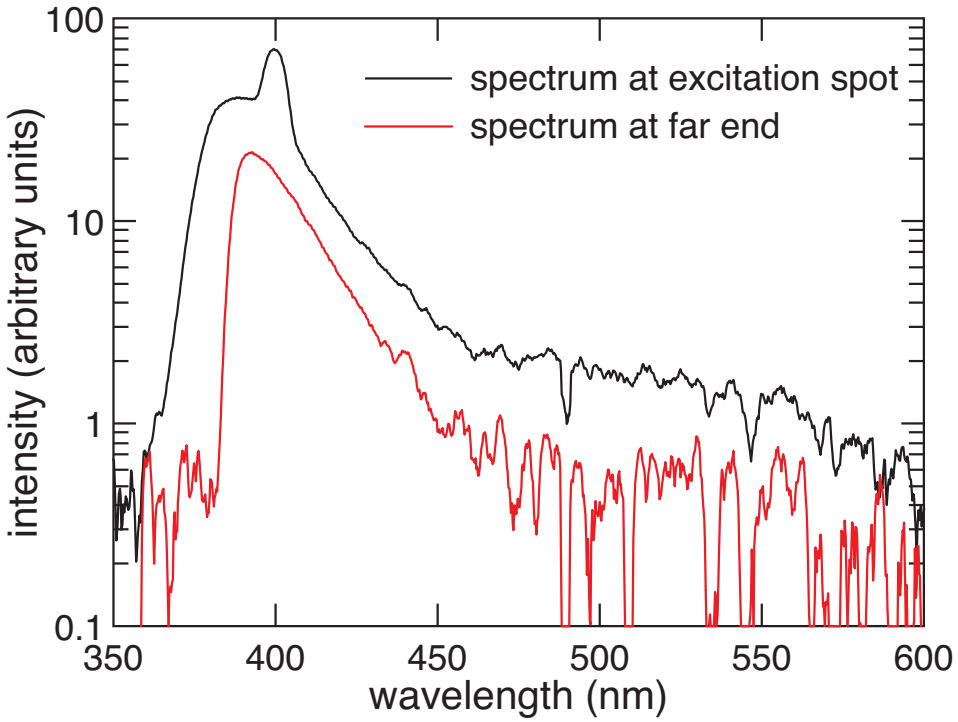

Figure 6.4: Emission spectrum of a single nanowire at the excitation spot (input) and spectrum of the light emitted at the other end of the nanowire 25 μm away from the excitation spot (output).

and at the far end of the nanowire, 25 μm away from the excitation spot (output). As expected, the output intensity is distinctly weaker than the input intensity. The peak due to second-harmonic generation is absent in the output spectrum. Below 390 nm, the output intensity drops sharply to the noise level, even though the input intensity is still significant. At long wavelengths, the output spectrum follows the same general trend as the input spectrum.

To understand the relation between the two spectra in Figure 6.4, we plot their ratio I_{out}/I_{in} in Figure 6.5. For comparison we also show the input spectrum on a linear scale. The ratio I_{out}/I_{in} in Figure 6.5 can be interpreted as a transmission spectrum that also accounts for the different coupling efficiencies of the photoluminescence and second-

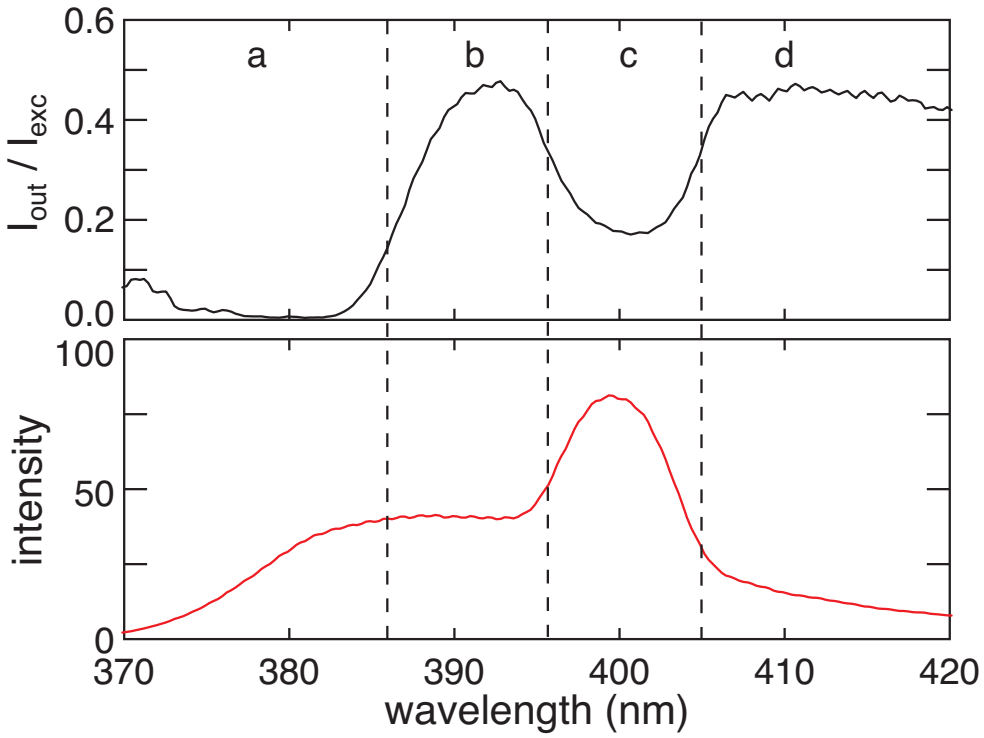

Figure 6.5: Ratio of the output to input intensity for a single nanowire. The input spectrum is also shown for comparison. The spectra are divided into four regions discussed in the text.

harmonic generation into the waveguide modes of the nanowire waveguide. We can identify four different regions in this transmission spectrum. In region I the I_{out}/I_{in} is close to zero even though we observe considerable intensity in the corresponding part of the input spectrum. In region II the photoluminescence in the input spectrum is maximum and I_{out}/I_{in} has a local maximum. Region III, which is at the position of the second-harmonic in the input spectrum, shows a decrease in I_{out}/I_{in}. In Region IV I_{out}/I_{in} increases again to the same approximately constant value as in region II and the input spectrum shows contributions from the photoluminescence.

In Figures 6.6 and 6.7, we show the results of 3D finite-element simulations of the temperature distribution in a hexagonal ZnO nanowire. The nanowire, with a length of

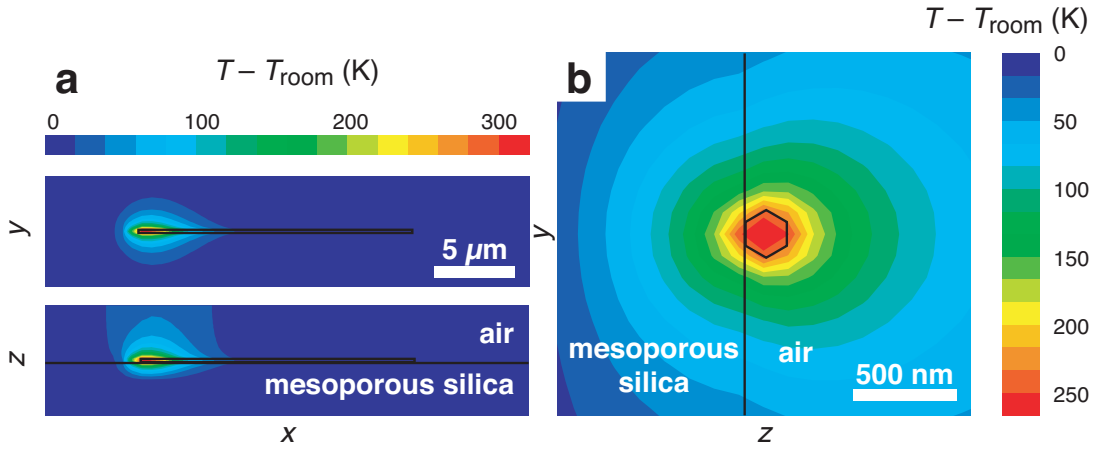

Figure 6.6: Finite-element simulations of the temperature profiles of a ZnO nanowire heated at one end and lying on a glass substrate that is covered with a layer of mesoporous silica. (a) Color-coded 2D temperature profiles in the x-y and x-z planes for $z = 0$ and $y = 0$ μm, respectively. (b) Temperature profile in the z-y plane for x = 7.5 μm.

15 μm and a diameter of 200 nm (measured from edge to edge of the hexagon), is lying on a glass substrate covered with a 1-μm thick layer of mesoporous silica. The ratios of the thermal conductivities $c_{ZnO}/c_{mesoporous\ silica}/c_{glass}/c_{air}$ are taken to be 10/0.1/1/0.02 [129]. The value for c_{ZnO} takes into account a ten-fold reduction in thermal conductivity of nanostructures compared to bulk samples [129].

In the simulation the nanowire is heated up to a temperature of 600 K by adding a constant heat source at one end of the nanowire (the heat source is modeled by adding a 2-μm long internally-heated piece of nanowire to the actual nanowire). We obtained the results shown in Figures 6.6 and 6.7 by numerically solving the heat-conductivity equation for the system. The computational cell extends from -450 μm to $+450$ μm in the x- and y-directions, and from -15 μm to $+15$ μm in z-direction. The boundaries are kept at a constant $T = 300$ K. The nanowire is centered at the origin of the computational cell.

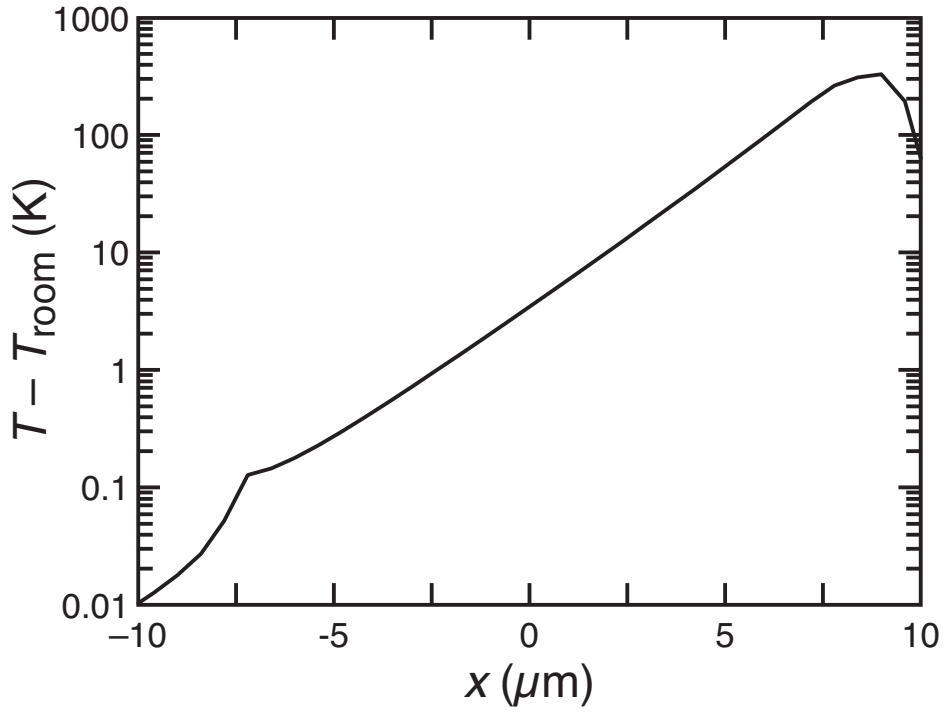

Figure 6.7: Finite-element simulations of the temperature profiles of a ZnO nanowire heated at one end and lying on a glass substrate that is covered with a layer of mesoporous silica. Temperature increase $T - T_{room}$ as a function of x for $y = 0$ μm, $z = 0$ μm plotted on a logarithmic scale.

The heated piece of nanowire piece is located in the region between $x = 7.5$ and 9.5 μm. Figure 6.6a shows color-coded two-dimensional temperature profiles of the nanowire in the x-y plane at $z = 0$ and the x-z plane at $y = 0$, respectively. In Figure 6.6b, we show the temperature profile in the y-z plane at $x = 7.5$ (adjacent to the heated region $x = 7.5$ to 9.5).

The one-dimensional temperature increase $T - T_{room}$ along the x-direction of the nanowire is plotted in Figure 6.7 for $y = 0$, $z = 0$. The simulations demonstrate an almost exponential decay of the temperature difference $T - T_{room}$ along the nanowire. The simulation in Figure 6.7 gives a characteristic length scale of about 3.5 μm for a ten-fold decrease in $T - T_{room}$.

6.4 Discussion

Figures 6.2 and 6.3 show that it is possible to efficiently excite near band-edge photoluminescence and second-harmonic radiation in ZnO nanowires using 800-nm femtosecond laser pulses incident normal to the nanowires. Radiation incident normal to the *c*-plane of ZnO leads to a vanishing contribution from $\chi^{(2)}$ [126] but radiation normal to the *a*-plane of microcrystalline ZnO layers was shown to be especially favorable for second-harmonic generation [127]. Our results confirm similar behavior for ZnO nanowires; excitation normal to the side surfaces leads to efficient second-harmonic generation. In contrast to previously published results [128, 120], however, we observe only weak deep-level emission because of the high crystalline quality of our high-temperature grown nanowires.

Figures 6.4 and 6.5 show that the different contributions of the excited nanowire emission couple into the waveguide modes of the nanowire with distinctly different efficiencies. The minimum in the transmission spectrum in region III of Figure 6.5 at the spectral position of the second-harmonic emission can be explained by the directed nature of the second-harmonic generation process. Because the nanowire is excited perpendicular to its waveguiding direction, the second harmonic of the excitation pulses is also preferentially emitted perpendicular to the waveguide. The large acceptance angle of the ZnO nanowires (about 40°, measured with respect to the symmetry axis of the waveguide [130]) and NA of the reflective objective used for excitation (0.50), however, still permits part of the second harmonic to couple into waveguide modes, albeit with a distinctly lower efficiency than the isotropically emitted photoluminescence. This lower coupling efficiency explains the decrease in I_{out}/I_{in} at the second-harmonic wavelength in region III of Figure 6.5.

The small value of in I_{out}/I_{in} in region I of Figure 6.5 can be attributed to reabsorption of the photoluminescence as it is guided along the nanowire. Under high-excitation

conditions photoluminescence emission lines in semiconductors are significantly broadened and shifted by heating, band-gap renormalization, screening and state filling [131]. The short-wavelength photoluminescence is sufficiently energetic to induce transitions across the band gap and is therefore absorbed in the unexcited part of the nanowire. This interband absorption reduces the transmission to almost zero in region I in Figure 6.5.

We expect excitation of the nanowire with an 11-MHz train of intense ultrashort laser pulses to heat the nanowire substantially. In a highly excited semiconductor, an increase in temperature and screening both reduce the band gap [131, 132]. Indeed, the absorption edge in Figure 6.5 at $\lambda = (385 \pm 5)$ nm, corresponding to a band gap energy $E_{gap} = (3.22 \pm 0.04)$ eV, is shifted down from the room temperature value of the ZnO band gap, $E_{gap} = 3.370$ eV, by an amount $\Delta E = (150 \pm 40)$ meV [125, 133]. The observed shift in the band edge in Figure 6.5 thus allows us to determine an upper limit for the temperature of the nanowire. To first order, we can ignore the screening effects for the excited nanowires [134]. Under this approximation, we can use the results from Ref. [133], reproduced in Figure 6.8, to convert the band-gap shift observed in our experiments to a corresponding temperature $T = (580 \pm 50)$ K of the ZnO nanowire. The rise in temperature of about 300 K is still significantly below the melting temperature of the material.

The finite-element simulation of the temperature distribution in Figures 6.6a and 6.7 shows that only a 3-μm region around the excitation spot is heated significantly. The relatively high thermal conductivity of the nanowire material compared to that of the surrounding air and substrate produces the almost perfect exponential temperature decay along the length of the nanowire. A few micrometers of nanowire material with a redshifted bandgap, however, are long enough for the waveguide modes to experience substantial absorption because typical absorption lengths in ZnO are around 300 nm. The numerical simulations therefore confirm that the local heating of nanowires under excitation with

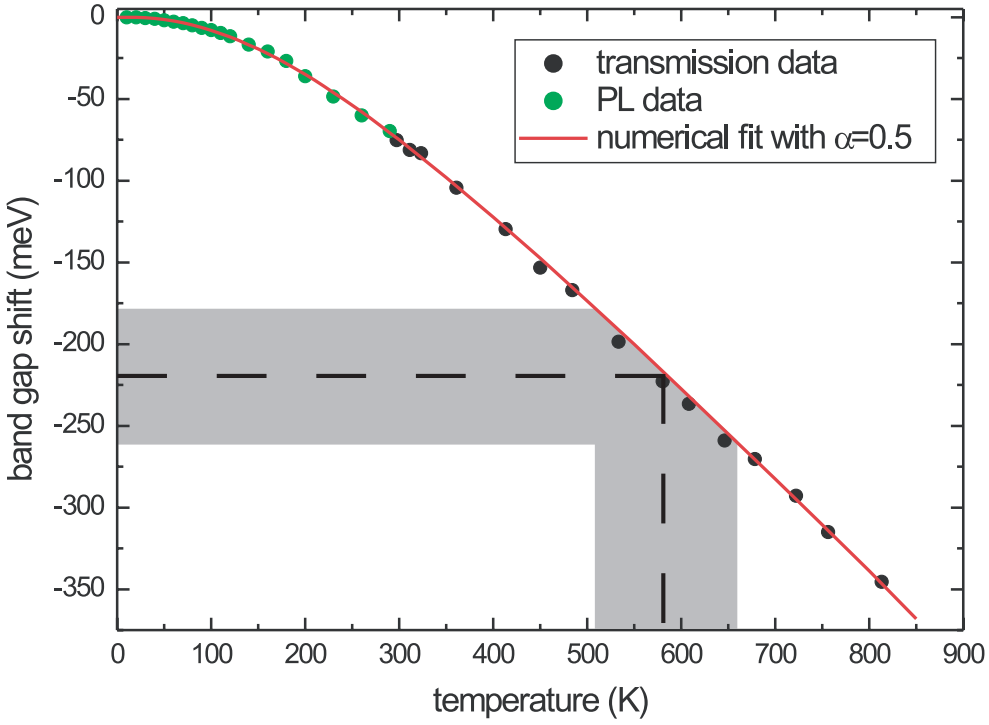

Figure 6.8: ZnO band-gap shift as a function of temperature. The dashed line shows the measured band-gap shift and the corresponding nanowire temperature with the shaded region showing the uncertainty. After Ref. [133].

intense femtosecond laser pulses can have a significant effect that needs to be taken into consideration when interpreting experimental results.

6.5 Conclusions

In summary, we generated blue and green photoluminescence and second harmonic radiation by femtosecond multiphoton excitation of individual ZnO nanowires. We find that each of these contributions to the excited-nanowire emission couple into waveguide modes of the nanowire. By comparing the emission spectra at the input and output of the nanowire we can measure the transmission of a single nanowire. The resulting transmission spectra show that the photoluminescence and the second harmonic couple into the waveguide modes with

distinctly different efficiencies because the photoluminescence emission is isotropic, while the second harmonic generation is mainly directed normal to the axis of the nanowire.

The transmission spectra also show that the band gap of the excited nanowire is shifted to lower energy due to the elevated temperature of the nanowire at the excitation spot and due to screening effects in the highly excited nanowire. Our results reveal an upper limit for the temperature at the excitation spot of $T = (580 \pm 50)$ K under excitation with an 11-MHz pulse train of 60-fs pulses with an excitation fluence of 0.45 kJ/m^2. We performed numerical simulations of the temperature distribution in a single ZnO nanowire that yield a nearly exponentially decreasing temperature profile along the nanowire. The temperature increase drops by one order of magnitude after a characteristic length of about 3.5 μm in the ZnO nanowire confirming the importance of local laser heating for the optical properties of these nanowires. Our results demonstrate that nonlinear fs-pulse excitation of semiconductor nanowires is a convenient method to study the transmission properties of individual nanowire waveguides. The same method will also be useful for analyzing the transmission characteristics of nanowire heterostructures and for studying the interaction of waveguide modes and their evanescent contributions with surrounding media.

6.6 Outlook

The results from Chapter 5 show the potential for ZnO nanowires as passive waveguiding structures. In this chapter we found the ZnO material system promising for nonlinear nanoscale photonic devices. Integration of the bottom-up chemically grown ZnO nanowires, with their high degree of uniformity and control of dopants, creates new possibilities by confining the mode tighter and reducing the peak power needed to produce substantial nonlinear effects.

Future experiments may take further advantage of changing material parameters, or simultaneous electrical operation, to introduce new functionality for optical devices. Experiments combining semiconducting and silica nanowires open up opportunities to better control the nonlinearity and dispersion in specific regions of interest. In particular, using the Sagnac interferometer geometry from Chapter 4, ZnO nanowires of specified lengths can be placed along along the Sagnac loop to provide a higher nonlinearity without increasing the size of the structure. Combinations of this type will prove useful for reducing the pulse energies required to achieve useful nonlinear device operation.

Chapter 7

Summary and outlook

This dissertation explored the linear and nonlinear optical properties of silica nanowires for assembling microphotonic devices and examined the possibility of combining silica and semiconductor nanowires, specifically ZnO, to build nanoscale photonic devices with new functionality enabled by the nonlinear interaction of light with matter.

The properties of the sub-micrometer silica optical fibers, as a result of the fabrication technique, lend themselves to a variety of applications. We demonstrated that the smooth sidewalls and high degree of uniformity allow low-loss waveguiding for optical and near-infrared wavelengths of light. Our numerical simulations showed that the high index contrast between silica and air contribute to the tight confinement of the mode and substantial evanescent field surrounding the nanowire. The physical properties, such as flexibility and strength, enable manipulation and assembly of the nanowires into more complicated structures like bends, couplers, and resonators.

The large evanescent field creates a strong interaction between silica nanowires and the environment. The well-understood surface chemistry of glass means the nanowires can be functionalized to interact with specific chemical or biological species in the surrounding

gaseous or liquid cladding. Assembling the nanowires into a resonator or interferometer geometry can substantially enhance the sensitivity of a functionalized nanowire down to the single molecule level.

Silica nanowires can also be used to manipulate single atoms. Cold atoms in a magneto-optical trap can be loaded into a quazi-atomic state around a silica nanowire [135, 136, 137]. Off-resonant light propagating along the nanowire creates an evanescent field whose intensity causes a level shifting which attracts the atoms to the nanowire. The attraction can be balanced by the circular motion of the atom around the wire, giving rise to "orbital" levels like those calculated for the Bohr atom.

By aligning the end face of a silica nanowire or sharp taper perpendicular to a surface, we can deliver high power pulses to a surface of interest. With sufficient power and dispersion management, the pulses can create a plasma on the surface, which upon re-combination, will emit spectral lines that can be used to identify the composition of the material at the surface. The emitted light from this process, also referred to as laser-induced breakdown spectroscopy, can be collected by separate optics or by the pulse delivery nanowire itself. The tight confinement of light in a silica nanowire suggests that sub-micrometer spectral identification may be possible.

We also discussed the nonlinear effects inside nanowires. We demonstrated supercontinuum generation, and used the spectral broadening as a probe of the nonlinearity of the nanowire. One application for the generated light is a coherent white light source in nanoscale optical devices. We also envision submersing the nanowires in solutions with nonlinearity, and potentially gain, tailored to a specific spectral region. Nonlinear optical processes in silica nanowires can be used for wavelength conversion to produce optical delay lines based on the difference in group velocity, or other slow-light techniques [138, 139].

We demonstrated the first silica nanowire Sagnac interferometer to show the po-

tential use of nonlinear microphotonic devices for integrated optical circuits. We observed a power-dependent transmission that may be used for optical switching, and discussed the potential implementation of the nonlinear Sagnac interferometer as NAND optical logic gate. Future experiments will take advantage of heterostructures that will increase the nonlinearity and thereby reduce the required interaction length and operating power.

We examined one potential heterostructure by studying the waveguiding properties of ZnO nanowires. We used silica nanowires to directly inject light into the waveguiding modes of the ZnO nanowires. We also studied the transmission characteristics of ZnO nanowires being excited by a fs-pulsed laser. We demonstrated that the excitation of ZnO nanowires with light can change the optical properties of the nanowire waveguide. Combinations of different types of nanowires can provide opportunities to exploit the material and waveguiding properties that will ultimately enable new functionality in nanoscale optical circuits.

Research with silica nanowires has also created a broader impact in middle school and high school education. The Massachusetts school system has recently added nanotechnology into the state curriculum as a method for integrating math, chemistry, biology, physics, and engineering. While nanotechnology is indeed heavily multidisciplinary, the concepts are difficult to visualize, and "hands-on" experience usually requires expensive equipment. The fact that silica nanowires can be fabricated by hand, at a low cost, presents an opportunity to bring modern nanoscale research to the classroom.

References

[1] D. H. Fischer, *Paul Revere's ride*. New York: Oxford University Press, 1994.

[2] "Bell's Photophone," *Nature*, vol. 23, pp. 15–19, Nov. 1880.

[3] D. Colladon, "On the reflection of a ray of light inside a parabolic liquid stream," *Comptes Rendus*, vol. 15, pp. 800–802, Oct 1842.

[4] J. Tyndall, "On floating matter and beams of light," *Nature*, vol. 1, pp. 499–501, Mar. 1870.

[5] J. C. Maxwell, "A dynamical theory of the electromagnetic field," *Philosophical Transactions of the Royal Society of London*, vol. 155, pp. 459–512, 1865.

[6] R. Maurer and P. Schultz, "Fused silica optical waveguide." United States Patent 3659915, May 1972.

[7] J. Hecht, *City of light : the story of fiber optics*. Oxford: Oxford University Press, rev. and expanded ed ed., 2004.

[8] A. L. Schawlow and C. H. Townes, "Infrared and optical masers," *Physical Review*, vol. 112, pp. 1940–1949, Dec 1958.

[9] T. H. Maiman, "Stimulated optical radiation in ruby," *Nature*, vol. 187, no. 4736, pp. 493–494, 1960.

[10] N. Bloembergen, *Nonlinear optics*. Singapore ; River Edge, NJ: World Scientific, 4th ed., 1996. Nicolaas Bloembergen. ill. ; 26 cm.

[11] G. P. Agrawal, *Nonlinear fiber optics*. Optics and photonics, San Diego: Academic Press, 3rd ed., 2001.

[12] T. G. Philbin, C. Kuklewicz, S. Robertson, S. Hill, F. Konig, and U. Leonhardt, "Fiber-optical analog of the event horizon," *Science*, vol. 319, pp. 1367–1370,

Mar 2008.

[13] N. Engheta, "Circuits with Light at Nanoscales: Optical Nanocircuits Inspired by Metamaterials," *Science*, vol. 317, no. 5845, pp. 1698–1702, 2007.

[14] W. L. Barnes, A. Dereux, and T. W. Ebbesen, "Surface plasmon subwavelength optics," *Nature*, vol. 424, no. 6950, pp. 824–830, 2003.

[15] S. A. Maier, P. G. Kik, and H. A. Atwater, "Observation of coupled plasmon-polariton modes in au nanoparticle chain waveguides of different lengths: Estimation of waveguide loss," *Applied Physics Letters*, vol. 81, no. 9, pp. 1714–1716, 2002.

[16] A. M. Morales and C. M. Lieber, "A laser ablation method for the synthesis of crystalline semiconductor nanowires," *Science*, vol. 279, no. 5348, pp. 208–211, 1998.

[17] X. F. Duan and C. M. Lieber, "General synthesis of compound semiconductor nanowires," *Advanced Materials*, vol. 12, no. 4, pp. 298–302, 2000.

[18] M. Law, D. J. Sirbuly, J. C. Johnson, J. Goldberger, R. J. Saykally, and P. D. Yang, "Nanoribbon waveguides for subwavelength photonics integration," *Science*, vol. 305, no. 5688, pp. 1269–1273, 2004.

[19] C. J. Barrelet, A. B. Greytak, and C. M. Lieber, "Nanowire photonic circuit elements," *Nano Letters*, vol. 4, no. 10, pp. 1981–1985, 2004.

[20] D. J. Sirbuly, M. Law, H. Q. Yan, and P. D. Yang, "Semiconductor nanowires for subwavelength photonics integration," *Journal of Physical Chemistry B*, vol. 109, no. 32, pp. 15190–15213, 2005.

[21] Y. N. Xia, J. A. Rogers, K. E. Paul, and G. M. Whitesides, "Unconventional methods for fabricating and patterning nanostructures," *Chemical Reviews*, vol. 99, no. 7, pp. 1823–1848, 1999.

[22] R. Ahmad, F. Pizzuto, G. Camarda, R. Espinola, H. Rao, and J. Osgood, R.M., "Ultracompact corner-mirrors and T-branches in silicon-on-insulator," *Photonics Technology Letters, IEEE*, vol. 14, no. 1, pp. 65–67, 2002.

[23] F. Romanato, D. Cojoc, E. Di Fabrizio, M. Galli, and D. Bajoni, "X-ray and electron-beam lithography of three-dimensional array structures for photonics," *Journal of Vacuum Science and Technology B*, vol. 21, no. 6, pp. 2912–2917, 2003.

[24] L. Eldada, "Optical communication components," *Review of Scientific Instruments*, vol. 75, no. 3, pp. 575–593, 2004.

[25] L. M. Tong, R. R. Gattass, J. B. Ashcom, S. L. He, J. Y. Lou, M. Y. Shen, I. Maxwell, and E. Mazur, "Subwavelength-diameter silica wires for low-loss optical wave guiding," *Nature*, vol. 426, no. 6968, pp. 816–819, 2003.

[26] C. Borchers, S. Muller, D. Stichtenoth, D. Schwen, and C. Ronning, "Catalyst-nanostructure interaction in the growth of 1-d ZnO nanostructures," *Journal of Physical Chemistry B*, vol. 110, pp. 1656–1660, Feb 2006.

[27] E. Snitzer, "Cylindrical dielectric waveguide modes," *Journal Of The Optical Society Of America*, vol. 51, no. 5, p. 491, 1961.

[28] G. P. Agrawal, *Applications of nonlinear fiber optics*. Optics and photonics, San Diego: Academic Press, 2001.

[29] A. W. Snyder and J. D. Love, *Optical waveguide theory*. Science paperbacks ; 190, London ; New York: Chapman and Hall, 1983.

[30] L. M. Tong, J. Y. Lou, and E. Mazur, "Single-mode guiding properties of subwavelength-diameter silica and silicon wire waveguides," *Optics Express*, vol. 12, no. 6, pp. 1025–1035, 2004.

[31] L. M. Tong and E. Mazur, "Silica nanowires and subwavelength-diameter fibres," in *Specialty Optical Fibers Handbook*, 2006.

[32] C. Boys, ""on the production, properties, and some suggested uses of the finest threads"," *Philosophical Magazine*, vol. 23, pp. 489–499, 1887.

[33] R. Threlfall, *On laboratory arts*. London: Macmillan, 1898.

[34] S. G. Leon-Saval, T. A. Birks, W. J. Wadsworth, P. S. J. Russell, and M. W. Mason, "Supercontinuum generation in submicron fibre waveguides," *Optics Express*, vol. 12, no. 13, pp. 2864–2869, 2004.

[35] M. Sumetsky, Y. Dulashko, and A. Hale, "Fabrication and study of bent and coiled free silica nanowires: Self-coupling microloop optical interferometer," *Optics Express*, vol. 12, no. 15, pp. 3521–3531, 2004.

[36] P. Domachuk and B. J. Eggleton, "Photonics - shrinking optical fibres," *Nature Materials*, vol. 3, no. 2, pp. 85–86, 2004.

[37] G. Brambilla, E. Koizumi, X. Feng, and D. J. Richardson, "Compound-glass

optical nanowires," *Electronics Letters*, vol. 41, no. 7, pp. 400–402, 2005.

[38] L. Tong, J. Lou, Z. Ye, G. T. Svacha, and E. Mazur, "Self-modulated taper drawing of silica nanowires," *Nanotechnology*, vol. 16, no. 9, p. 1445, 2005.

[39] L. M. Tong, L. L. Hu, J. J. Zhang, J. R. Qiu, Q. Yang, J. Y. Lou, Y. H. Shen, J. L. He, and Z. Z. Ye, "Photonic nanowires directly drawn from bulk glasses," *Optics Express*, vol. 14, no. 1, pp. 82–87, 2006.

[40] F. Bilodeau, K. O. Hill, S. Faucher, and D. C. Johnson, "Low-loss highly overcoupled fused couplers - fabrication and sensitivity to external-pressure," *Journal of Lightwave Technology*, vol. 6, no. 10, pp. 1476–1482, 1988.

[41] T. A. Birks and Y. W. Li, "The shape of fiber tapers," *Journal of Lightwave Technology*, vol. 10, no. 4, pp. 432–438, 1992.

[42] M. Sumetsky, Y. Dulashko, and A. Hale, "Fabrication and study of bent and coiled free silica nanowires: Self-coupling microloop optical interferometer," *Optics Express*, vol. 12, no. 15, pp. 3521–3531, 2004.

[43] H. E. Labelle and A. I. Mlavsky, "Growth of sapphire filaments from melt," *Nature*, vol. 216, no. 5115, p. 574, 1967.

[44] N. P. Bansal and R. H. Doremus, *Handbook of glass properties.* Academic Press handbook series, Orlando: Academic Press, 1986. Narottam P. Bansal and R.H. Doremus. ill. ; 25 cm.

[45] A. J. C. Grellier, N. K. Zayer, and C. N. Pannell, "Heat transfer modelling in co2 laser processing of optical fibres," *Optics Communications*, vol. 152, no. 4-6, pp. 324–328, 1998.

[46] L. M. Tong, J. Y. Lou, R. R. Gattass, S. L. He, X. W. Chen, L. Liu, and E. Mazur, "Assembly of silica nanowires on silica aerogels for microphotonic devices," *Nano Letters*, vol. 5, no. 2, pp. 259–262, 2005.

[47] M. J. Matthewson and C. R. Kurkjian, "Static fatigue of optical fibers in bending," *Journal of the American Ceramic Society*, vol. 70, no. 9, pp. 662–668, 1987.

[48] V. AnnovazziLodi, S. Donati, S. Merlo, and G. Zapelloni, "Statistical analysis of fiber failures under bending-stress fatigue," *Journal of Lightwave Technology*, vol. 15, no. 2, pp. 288–293, 1997.

[49] J. Sakai and T. Kimura, "Bending loss of propagation modes in arbitrary-index

profile optical fibers," *Applied Optics*, vol. 17, no. 10, pp. 1499–1506, 1978.

[50] J. D. Joannopoulos, R. D. Meade, and J. N. Winn, *Photonic crystals : molding the flow of light*. Princeton, N.J.: Princeton University Press, 1995.

[51] G. Brambilla, V. Finazzi, and D. J. Richardson, "Ultra-low-loss optical fiber nanotapers," *Optics Express*, vol. 12, no. 10, pp. 2258–2263, 2004.

[52] Y. K. Akimov, "Fields of application of aerogels (review)," *Instruments and Experimental Techniques*, vol. 46, no. 3, pp. 287–299, 2003.

[53] A. C. Pierre and G. M. Pajonk, "Chemistry of aerogels and their applications," *Chemical Reviews*, vol. 102, no. 11, pp. 4243–4265, 2002.

[54] D. Konjhodzic, H. Bretinger, U. Wilczok, A. Dreier, A. Ladenburger, M. Schmidt, M. Eich, and F. Marlow, "Low-n mesoporous silica films: structure and properties," *Applied Physics A-Materials Science and Processing*, vol. 81, pp. 425–432, Jul 2005.

[55] M. Schmidt, G. Boettger, M. Eich, W. Morgenroth, U. Huebner, R. Boucher, H. G. Meyer, D. Konjhodzic, H. Bretinger, and F. Marlow, "Ultralow refractive index substrates-a base for photonic crystal slab waveguides," *Applied Physics Letters*, vol. 85, pp. 16–18, Jul 2004.

[56] G. Kakarantzas, T. E. Dimmick, T. A. Birks, R. Le Roux, and P. S. J. Russell, "Miniature all-fiber devices based on co2 laser micro structuring of tapered fibers," *Optics Letters*, vol. 26, no. 15, pp. 1137–1139, 2001.

[57] M. G. Daly, P. E. Jessop, and D. Yevick, "Crosstalk reduction in intersecting rib waveguides," *Journal of Lightwave Technology*, vol. 14, no. 7, pp. 1695–1698, 1996.

[58] S. G. Johnson, C. Manolatou, S. H. Fan, P. R. Villeneuve, J. D. Joannopoulos, and H. A. Haus, "Elimination of cross talk in waveguide intersections," *Optics Letters*, vol. 23, no. 23, pp. 1855–1857, 1998.

[59] M. Sumetsky, Y. Dulashko, J. M. Fini, and A. Hale, "Optical microfiber loop resonator," *Applied Physics Letters*, vol. 86, no. 16, 2005.

[60] R. R. Gattass, G. T. Svacha, L. Tong, and E. Mazur, "Supercontinuum generation in sub-wavelength diameter silica fibers," *Optics Express*, vol. 14, pp. 9408–9414, Oct 2006.

[61] A. L. Gaeta, "Catastrophic collapse of ultrashort pulses," *Physical Review*

Letters, vol. 84, no. 16, pp. 3582–3585, 2000.

[62] M. A. Foster, K. D. Moll, and A. L. Gaeta, "Optimal waveguide dimensions for nonlinear interactions," *Optics Express*, vol. 12, no. 13, pp. 2880–2887, 2004.

[63] M. A. Foster and A. L. Gaeta, "Ultra-low threshold supercontinuum generation in sub-wavelength waveguides," *Optics Express*, vol. 12, no. 14, pp. 3137–3143, 2004.

[64] A. V. Husakou and J. Herrmann, "Supercontinuum generation of higher-order solitons by fission in photonic crystal fibers," *Physical Review Letters*, vol. 87, no. 20, p. 203901, 2001.

[65] A. V. Husakou and J. Herrmann, "Supercontinuum generation, four-wave mixing, and fission of higher-order solitons in photonic-crystal fibers," *Journal Of The Optical Society Of America B-Optical Physics*, vol. 19, no. 9, pp. 2171–2182, 2002.

[66] K. Sakamaki, M. Nakao, M. Naganuma, and M. Izutsu, "Soliton induced supercontinuum generation in photonic crystal fiber," *Ieee Journal Of Selected Topics In Quantum Electronics*, vol. 10, no. 5, pp. 876–884, 2004.

[67] J. Herrmann, U. Griebner, N. Zhavoronkov, A. Husakou, D. Nickel, J. C. Knight, W. J. Wadsworth, P. S. J. Russell, and G. Korn, "Experimental evidence for supercontinuum generation by fission of higher-order solitons in photonic fibers," *Physical Review Letters*, vol. 88, no. 17, p. 173901, 2002.

[68] L. Tartara, I. Cristiani, and V. Degiorgio, "Blue light and infrared continuum generation by soliton fission in a microstructured fiber," *Applied Physics B-Lasers And Optics*, vol. 77, no. 2-3, pp. 307–311, 2003.

[69] I. Cristiani, R. Tediosi, L. Tartara, and V. Degiorgio, "Dispersive wave generation by solitons in microstructured optical fibers," *Optics Express*, vol. 12, no. 1, pp. 124–135, 2004.

[70] J. Teipel, K. Franke, D. Turke, F. Warken, D. Meiser, M. Leuschner, and H. Giessen, "Characteristics of supercontinuum generation in tapered fibers using femtosecond laser pulses," *Applied Physics B-Lasers And Optics*, vol. 77, no. 2-3, pp. 245–251, 2003.

[71] R. Zhang, X. P. Zhang, D. Meiser, and H. Giessen, "Mode and group velocity dispersion evolution in the tapered region of a single-mode tapered fiber," *Optics Express*, vol. 12, no. 24, pp. 5840–5849, 2004.

[72] G. P. Agrawal, *Fiber-optic communication systems.* New York: Wiley-Interscience, 3rd ed ed., 2002.

[73] K. Smith, N. J. Doran, and P. G. J. Wigley, "Pulse shaping, compression, and pedestal suppression employing a nonlinear-optical loop mirror," *Optics Letters*, vol. 15, pp. 1294–1296, Nov. 1990.

[74] K. Otsuka, "Nonlinear antiresonant ring interferometer," *Optics Letters*, vol. 8, pp. 471–473, Sept. 1983.

[75] A. G. Bulushev, E. M. Dianov, and O. G. Okhotnikov, "Intracavity pulse compression in a laser with nonlinear resonator," *IEEE Photonics Technology Letters*, vol. 2, pp. 699–701, Oct. 1990.

[76] A. G. Bulushev, E. M. Dianov, and O. G. Okhotnikov, "Passive mode locking of a laser with a nonlinear fiber reflector," *Optics Letters*, vol. 15, pp. 968–970, Sept. 1990.

[77] A. Michelson and E. Morley, "On the relative motion of the earth and the luminiferous ether," *American Journal of Science*, vol. 34, pp. 333–345, 1887.

[78] R. J. Sandeman and D. E. McClelland, "Laser interferometer gravitational-wave observatories - an overview," *Journal of Modern Optics*, vol. 37, pp. 1747–1759, Nov 1990.

[79] G. Gauglitz, "Direct optical sensors: principles and selected applications," *Analytical and Bioanalytical Chemistry*, vol. 381, pp. 141–155, Jan 2005.

[80] M. Srinivasarao, "Nano-optics in the biological world: Beetles, butterflies, birds, and moths," *Chemical Reviews*, vol. 99, pp. 1935–1961, Jul 1999.

[81] P. Vukusic, J. R. Sambles, C. R. Lawrence, and R. J. Wootton, "Quantified interference and diffraction in single morpho butterfly scales," *Proceedings of the Royal Society of London Series B-Biological Sciences of the Royal Society of London Series B-Biological Sciences*, vol. 266, pp. 1403–1411, Jul 1999.

[82] E. J. Post, "Sagnac effect," *Reviews of Modern Physics*, vol. 39, pp. 475–493, Apr 1967.

[83] G. Sagnac, "Luminous ether demonstrated by the effect of relative wind of ether in a uniform rotation of an interferometer," *Comptes Rendus Hebdomadaires des Seances de l'Academie des Sciences*, vol. 157, pp. 708–710, 1913.

[84] G. Sagnac, "The proof of the reality of luminous ether by the experiment of

the turning interferograph," *Comptes Rendus Hebdomadaires des Seances de l'Academie des Sciences*, vol. 157, pp. 1410–1413, 1913.

[85] A. A. Michelson and H. G. Gale, "The Effect of the Earth's Rotation on the Velocity of Light," *Astrophysical Journal*, vol. 61, p. 137, Apr. 1925.

[86] G. Sagnac, "Effect tourbillonaire optique la circulation de l'éther lumineux dans un interférographe tournant," *Journal de Physique Théorique et Appliquée*, vol. 5, no. 4, pp. 177–195, 1914.

[87] C. V. Heer, "History of the laser gyro," *Proceedings of the Society of Photo-optical Instrumentation Engineers*, vol. 487, pp. 2–12, 1984.

[88] W. W. Chow, J. Geabanacloche, L. M. Pedrotti, V. E. Sanders, W. Schleich, and M. O. Scully, "The ring laser gyro," *Reviews of Modern Physics*, vol. 57, no. 1, pp. 61–104, 1985.

[89] G. E. Stedman, "Ring interferometric tests of classical and quantum-gravity," *Contemporary Physics*, vol. 26, no. 4, pp. 311–332, 1985.

[90] V. Vali and R. W. Shorthill, "Fiber ring interferometer," *Applied Optics*, vol. 15, p. 1099, May 1976.

[91] S. K. Kim, H. K. Kim, and B. Y. Kim, "Er^{3+}-doped fiber ring laser for gyroscope applications," *Optics Letters*, vol. 19, pp. 1810–1812, Nov. 1994.

[92] V. M. Menon, W. Tong, F. Xia, C. Li, and S. R. Forrest, "Nonreciprocity of counterpropagating signals in a monolithically integrated Sagnac interferometer," *Optics Letters*, vol. 29, pp. 513–515, Mar. 2004.

[93] M. Jinno and T. Matsumoto, "Ultrafast all-optical logic operations in a nonlinear Sagnac interferometer with two control beams," *Optics Letters*, vol. 16, pp. 220–222, Feb. 1991.

[94] K. Okamoto, *Fundamentals of optical waveguides*. San Diego: Academic Press, 2000.

[95] Website. `http://www.femtolasers.com`.

[96] H. A. Haus, *Waves and fields in optoelectronics*. Englewood Cliffs, NJ: Prentice-Hall, 1984.

[97] Website. `http://www.wasatchphotonics.com/`.

[98] N. J. Doran, D. S. Forrester, and B. K. Nayar, "Experimental investigation of all-optical switching in fiber loop mirror device," *Electronics Letters*, vol. 25, pp. 267–269, Feb 1989.

[99] K. J. Blow, N. J. Doran, and B. K. Nayar, "Experimental demonstration of optical soliton switching in an all-fiber nonlinear sagnac interferometer," *Optics Letters*, vol. 14, pp. 754–756, Jul 1989.

[100] K. J. Blow, N. J. Doran, and B. P. Nelson, "Demonstration of the nonlinear fiber loop mirror as an ultrafast all-optical demultiplexer," *Electronics Letters*, vol. 26, pp. 962–964, Jul 1990.

[101] D. Cotter, R. J. Manning, K. J. Blow, A. D. Ellis, A. E. Kelly, D. Nesset, I. D. Phillips, A. J. Poustie, and D. C. Rogers, "Nonlinear optics for high-speed digital information processing," *Science*, vol. 286, pp. 1523–1528, Nov 1999.

[102] A. O'Neill and R. Webb, "All-optical loop mirror switch employing an asymmetric amplifier/attenuator combination," *Electronics Letters*, vol. 26, no. 24, pp. 2008–2009, 1990.

[103] M. J. Weber, *Handbook of optical materials*. Boca Raton: CRC Press, 2003.

[104] Z. L. Wang and J. H. Song, "Piezoelectric nanogenerators based on zinc oxide nanowire arrays," *Science*, vol. 312, pp. 242–246, Apr 2006.

[105] Y. Li, F. Qian, J. Xiang, and C. M. Lieber, "Nanowire electronic and optoelectronic devices," *Materials Today*, vol. 9, pp. 18–27, Oct 2006.

[106] Y. Huang, X. F. Duan, and C. M. Lieber, "Nanowires for integrated multicolor nanophotonics," *Small*, vol. 1, pp. 142–147, Jan 2005.

[107] J. M. Bao, M. A. Zimmler, F. Capasso, X. W. Wang, and Z. F. Ren, "Broadband ZnO single-nanowire light-emitting diode," *Nano Letters*, vol. 6, pp. 1719–1722, Aug 2006.

[108] P. J. Pauzauskie and P. Yang, "Nanowire photonics," *Materials Today*, vol. 9, pp. 36–45, Oct 2006.

[109] R. Hauschild and H. Kalt, "Guided modes in ZnO nanorods," *Applied Physics Letters*, vol. 89, p. 123107, Sep 2006.

[110] Z. Ye, X. H. Hu, M. Li, K. M. Ho, and P. D. Yang, "Propagation of guided modes in curved nanoribbon waveguides," *Applied Physics Letters*, vol. 89, p. 241108, Dec 2006.

[111] A. V. Maslov and C. Z. Ning, "Reflection of guided modes in a semiconductor nanowire laser," *Applied Physics Letters*, vol. 83, pp. 1237–1239, Aug 2003.

[112] D. C. Look, "Recent advances in ZnO materials and devices," *Materials Science and Engineering B-Solid State Materials for Advanced Technology*, vol. 80, pp. 383–387, Mar 2001.

[113] T. Voss, C. Bekeny, L. Wischmeier, H. Gafsi, S. Borner, W. Schade, A. C. Mofor, A. Bakin, and A. Waag, "Influence of exciton-phonon coupling on the energy position of the near-band-edge photoluminescence of ZnO nanowires," *Applied Physics Letters*, vol. 89, p. 182107, Oct 2006.

[114] L. Wischmeier, T. Voss, S. Borner, and W. Schade, "Comparison of the optical properties of as-grown ensembles and single ZnO nanowires," *Applied Physics A-Materials Science and Processing*, vol. 84, pp. 111–116, Jul 2006.

[115] H. Yoshikawa and S. Adachi, "Optical constants of ZnO," *Japanese Journal Of Applied Physics Part 1-Regular Papers Short Notes and Review Papers*, vol. 36, pp. 6237–6243, Oct 1997.

[116] R. S. Wagner and W. C. Ellis, "Vapor-liquid-solid mechanism of single crystal growth," *Applied Physics Letters*, vol. 4, no. 5, p. 89, 1964.

[117] A. Farjadpour, D. Roundy, A. Rodriguez, M. Ibanescu, P. Bermel, J. D. Joannopoulos, S. G. Johnson, and G. W. Burr, "Improving accuracy by subpixel smoothing in the finite-difference time domain," *Optics Letters*, vol. 31, pp. 2972–2974, Oct 2006.

[118] Q. X. Zhao, M. Willander, R. E. Morjan, Q. H. Hu, and E. E. B. Campbell, "Optical recombination of ZnO nanowires grown on sapphire and si substrates," *Applied Physics Letters*, vol. 83, pp. 165–167, Jul 2003.

[119] G. C. Yi, C. R. Wang, and W. I. Park, "ZnO nanorods: synthesis, characterization and applications," *Semiconductor Science and Technology*, vol. 20, pp. S22–S34, Apr 2005.

[120] L. K. Van Vugt, S. Ruhle, and D. Vanmaekelbergh, "Phase-correlated nondirectional laser emission from the end facets of a ZnO nanowire," *Nano Letters*, vol. 6, pp. 2707–2711, Dec 2006.

[121] Y. R. Shen, *The principles of nonlinear optics*. Wiley classics library, Hoboken, N.J.: Wiley-Interscience, wiley classics library ed., 2003.

[122] C. Y. Liu, B. P. Zhang, N. T. Binh, and Y. Segawa, "Second harmonic genera-

tion in ZnO thin films fabricated by metalorganic chemical vapor deposition," *Optics Communications*, vol. 237, pp. 65–70, Jul 2004.

[123] C. Y. Liu, B. P. Zhang, N. T. Binh, and Y. Segawa, "Third-harmonic generation from ZnO films deposited by mocvd," *Applied Physics B-Lasers And Optics*, vol. 79, pp. 83–86, Jul 2004.

[124] M. C. Larciprete, D. Haertle, A. Belardini, M. Bertolotti, F. Sarto, and P. Gunter, "Characterization of second and third order optical nonlinearities of ZnO sputtered films," *Applied Physics B-Lasers And Optics*, vol. 82, pp. 431–437, Mar 2006.

[125] C. Klingshirn, R. Hauschild, H. Priller, M. Decker, J. Zeller, and H. Kalt, "ZnO rediscovered - once again!?," *Superlattices and Microstructures*, vol. 38, pp. 209–222, Oct-Dec 2005.

[126] U. Neumann, R. Grunwald, U. Griebner, G. Steinmeyer, and W. Seeber, "Second-harmonic efficiency of ZnO nanolayers," *Applied Physics Letters*, vol. 84, pp. 170–172, Jan 2004.

[127] U. Neumann, R. Grunwald, U. Griebner, G. Steinmeyer, M. Schmidbauer, and W. Seeber, "Second-harmonic performance of a-axis-oriented ZnO nanolayers on sapphire substrates," *Applied Physics Letters*, vol. 87, p. 171108, Oct 2005.

[128] C. F. Zhang, Z. W. Dong, G. J. You, R. Y. Zhu, S. X. Qian, H. Deng, H. Cheng, and J. C. Wang, "Femtosecond pulse excited two-photon photoluminescence and second harmonic generation in ZnO nanowires," *Applied Physics Letters*, vol. 89, p. 042117, Jul 2006.

[129] N. Mingo and D. A. Broido, "Lattice thermal conductivity crossovers in semiconductor nanowires," *Physical Review Letters*, vol. 93, p. 246106, Dec 2004.

[130] T. Voss, G. T. Svacha, E. Mazur, S. Muller, C. Ronning, D. Konjhodzic, and F. Marlow, "High-order waveguide modes in ZnO nanowires," *Nano Letters*, vol. 7, pp. 3675–3680, Dec 2007.

[131] C. F. Klingshirn, *Semiconductor optics*. Berlin: Springer, 2005.

[132] P. Y. Yu and M. Cardona, *Fundamentals of semiconductors : physics and materials properties*. Berlin: Springer, 3rd, rev. and enlarged ed ed., 2001.

[133] R. Hauschild, H. Priller, M. Decker, J. Brückner, H. Kalt, and C. Klingshirn, "Temperature dependent band gap and homogeneous line broadening of the exciton emission in ZnO," *Physica Status Solidi C Current Topics*, vol. 3,

pp. 976–979, Mar. 2006.

[134] M. Saraniti and U. Ravaioli, *Nonequilibrium carrier dynamics in semiconductors : proceedings of the 14th international conference, July 25-29, 2005, Chicago, USA*, vol. 110 of *Springer proceedings in physics*. Berlin: Springer, 2006.

[135] F. Le Kien, V. I. Balykin, and K. Hakuta, "Atom trap and waveguide using a two-color evanescent light field around a subwavelength-diameter optical fiber," *Physical Review A*, vol. 70, no. 6, 2004.

[136] V. I. Balykin, K. Hakuta, F. Le Kien, J. Q. Liang, and M. Morinaga, "Atom trapping and guiding with a subwavelength-diameter optical fiber," *Physical Review A*, vol. 70, no. 1, 2004.

[137] F. Le Kien, J. Q. Liang, K. Hakuta, and V. I. Balykin, "Field intensity distributions and polarization orientations in a vacuum-clad subwavelength-diameter optical fiber," *Optics Communications*, vol. 242, no. 4-6, pp. 445–455, 2004.

[138] R. W. Boyd and D. J. Gauthier, *Progress in Optics*, vol. 43. Amsterdam: Elsevier, 2002.

[139] Y. Okawachi, M. Foster, J. Sharping, A. Gaeta, Q. Xu, and M. Lipson, "All-optical slow-light on a photonic chip," *Opt. Express*, vol. 14, no. 6, pp. 2317–2322, 2006.